UNIVERSIDADE DE LISBOA
INSTITUTO SUPERIOR TÉCNICO

Quantum Transport in Hybrid Monolayer-Bilayer Graphene Structures

Hadi Zahir Olyaei

Supervisor: Doctor Eduardo Filipe Vieira de Castro
Co-Supervisor: Doctor Pedro José Gonçalves Ribeiro

Thesis approved in public session to obtain the PhD Degree in Physics

Jury final classification: Pass with Distinction

2020

UNIVERSIDADE DE LISBOA
INSTITUTO SUPERIOR TÉCNICO

Quantum Transport in Hybrid Monolayer-Bilayer Graphene Structures

Hadi Zahir Olyaei

Supervisor: Doctor Eduardo Filipe Vieira de Castro
Co-Supervisor: Doctor Pedro José Gonçalves Ribeiro

Thesis approved in public session to obtain the PhD Degree in Physics

Jury final classification: Pass with Distinction

Jury

Chairperson: **Doctor Vítor João Rocha Vieira, Instituto Superior Técnico, Universidade de Lisboa**
Members of the Committee:
Doctor Nuno Miguel Machado Reis Peres, Escola de Ciências, Univrsidade do Minho
Doctor Pedro Domingos Santos do Sacramento, Instituto Superior Técnico, Universidade de Lisboa
Doctor Eduardo Filipe Vieira de Castro, Faculdade de Ciências, Universidade do Porto
Doctor Bruno António Campos Amorim, Escola de Ciências, Univrsidade do Minho

Funding Institutions
FCT - Fundação para a Ciência e Tecnologia

2020

Resumo

Nesta tese, investigamos o transporte quântico em estruturas híbridas de grafeno - monocamada-bicamada-monocamada. Primeiro consideramos a dupla camada em empilhamento do tipo Bernal e, de seguida, generalizamos a nossa análise para um ângulo arbitrário de rotação entre as duas camadas. Em ambos os casos, a transmissão através da bicamada de grafeno foi calculada para dois tipos diferentes de conexões aos eletrodos feitos de uma camada única de grafeno.

No caso da bicamada com empilhamento tipo Bernal, um algoritmo baseado na matriz de transferência e num modelo de ligação forte foi desenvolvido para obter a transmissão balística para além do regime de resposta linear. Observou-se que as duas configurações se comportam de maneira semelhante, quando nenhuma tensão eletrostática é aplicada. Na presença de uma parede de domínio, delimitando a região sob tensão da bicamada, a condutância das duas configurações é similar. No entanto, para uma tensão finita, ambas desenvolvem um hiato na condutância característico de uma bicamada polarizada, mas apenas uma configuração mostra uma mudança abrupta na condutância. Conclui-se ainda que para uma microestrutura com paredes de domínio igualmente espaçadas, há uma alta sensibilidade ao tamanho do domínio. Este fenómeno deve-se à presença de estados topologicamente protegidos com energia no interior do hiato e localizados nas paredes de domínio, que hibridizam à medida que o tamanho de domínio se torna da ordem do seu comprimento de localização. Mostra-se ainda que a transmissão através de uma região de duas camadas pode ser manipulada por uma tensão eletrostática aplicada.

No caso de duas camadas de grafeno rodadas, obtivemos numericamente a condutância para estruturas com diferentes ângulos de rotação, comensuráveis ou incomensuráveis. Encontramos uma forte dependência no ângulo de rotação e diferenciamos três regimes qualitativamente diferentes: para ângulos grandes ($\theta \gtrsim 10^\circ$), existem fortes efeitos de comensurabilidade, aparecendo efeitos pronunciados na condutância para ângulos comensuráveis correspondendo a pequenas células unitárias. Também observamos que para grandes ângulos incomensuráveis as duas camadas de grafeno comportam-se efectivamente como se estivessem desacopladas; para ângulos intermédios ($3^\circ \lesssim \theta \lesssim 10^\circ$), encontramos uma correlação entre a condutância e density of states que sugere as propriedades de transporte podem ser usadas para determinar o ângulo de rotação; para pequenos ângulos ($1^\circ \lesssim \theta \lesssim 3^\circ$), verificámos a condutância se torna uma função suave do ângulo. Os resultados obtidos estão de acordo com resultados experimentais e sugerem que a condutância pode ser usada para determinar os regimes de bandas planas, com regiões de condutividade zero correlacionadas com hiatos na densidade de estados.

Palavras-chave: Transporte quântico, Grafeno, Bernal stacked bilayer, twisted bilayer, Estrutura monolayer-bilayer-monolayer.

Abstract

In this thesis, we investigate quantum transport in graphene-based hybrid monolayer-bilayer-monolayer structures. First we address the so-called Bernal stacked bilayer and later generalise our analysis for an arbitrary twisted angle. The transmission across a graphene bilayer region is calculated for two different types of connections to monolayer leads, corresponding either to a flake of graphene on top of a graphene strip or to two overlapped semi-infinite strips.

In the case of Bernal stacked bilayer graphene, a transfer matrix algorithm based on a tight-binding model is developed to obtain the ballistic transmission beyond linear response. We show that the two configurations, with different connections to the leads, behave similarly when no gate voltage is applied. For a finite gate voltage, both develop a conductance gap characteristic of a biased bilayer, but only one shows a pronounced conductance step at the gap edge. A gate voltage domain wall applied to the bilayer region renders the conductance of the two configurations similar. For a microstructure consisting of equally spaced domain walls, we find a high sensitivity to the domain size. This is attributed to the presence of topologically protected in-gap states localized at domain walls, which hybridize as the domain size becomes of the order of their confining scale. Our results show that transmission through a bilayer region can be manipulated by a gate voltage in ways not previously anticipated.

For the case of twisted bilayer graphene, we obtain the conductance numerically for structures with different twist angles which can be commensurate or incommensurate. We find a strong angle dependence with three qualitatively different regimes. For large angles ($\theta \gtrsim 10^\circ$) there are strong commensurability effects. Large commensurate angles, corresponding to a small unit cell, appear as sharp features in the conductance. We also observed that for large incommensurate angles, the two graphene layers effectively decouple. For intermediate angles ($3^\circ \lesssim \theta \lesssim 10^\circ$), we find a correlation of the conductance features with the twist angle, which suggests that conductance measurements can be used to determine the twisting angle. For small twisting angles ($1^\circ \lesssim \theta \lesssim 3^\circ$) we find that commensurability effects are washed out, and the conductance becomes a smooth function of the angle. Conductance can be used to probe the almost flat bands appearing in this regime. Our results agree with the recent experimental findings where zero conductance regions have been correlated with gaps in the density of states.

Keywords: Quantum transport, Graphene, Bernal stacked bilayer, Twisted bilayer, Monolayer-bilayer-monolayer structure

Acknowledgment

Firstly, I would like to express my sincere gratitude to my supervisor Dr. Eduardo V. Castro and co-supervisor Dr. Pedro Ribeiro for their continuous support of my Ph.D. study and related research, for their patience, motivation, and immense knowledge. Their guidance helped me in all the time of research and writing of this thesis. I could not have imagined having better mentors for my Ph.D study. I am also very thankful towards the Center of Physics and Engineering of Advanced Materials (CeFEMA) for providing workspace and support during the period of the PhD. I thank the support from the Fundacao para a Ciencia e a Tecnologia (FCT) through Doctoral Programme in the Physics and Mathematics of Information and the associated scholarship PD/BD/113649/2015 from September 2015 to August 2019.

Thank you,
Hadi Zahir Olyaei

List of Figures

Nomenclature

AGNR	Armchair graphene nanoribbon
BL	Bilayer
CLC	Chain-ladder-chain
DOS	Density of states
FBZ	First Brillouin zone
gcd	Greatest common divisor
GNR	Graphene nanoribbon
hBN	Hexagonal boron nitride
HOPG	Highly oriented pyrolytic graphite
KPM	Kernel polynomial method
MBM	monolayer-bilayer-monolayer
SLG	Single layer graphene
STM	Scanning tunneling microscopy
TB	Tight binding
tBLG	twisted bilayer graphene
vdW	van der Waal
vHS	van Hove Singularity
ZGNR	Zigzag graphene nanoribbon

Contents

1 Introduction

1.1 Context

Until 2004, it was presumed that two-dimensional (2D) materials were thermodynamically unstable and they could not be isolated. The argument was that displacement of atoms due to thermal fluctuations can be in the order of interatomic distances [1]. Hence, decreasing the thickness of thin films decreases their melting point and they become unstable at a thickness of few layers [2, 3]. In 2004, graphene was experimentally discovered and the 2D graphene crystals were found to show high crystal quality [4, 5]. Indeed, the existence of graphene can be reconciled with theory and it can be argued that strong interatomic bonds guarantees that thermal fluctuations cannot result in dislocations or other crystal defects even at higher temperature [1]. Graphene is a flat single layer of carbon atoms tightly packed into a 2D honeycomb lattice, and is a basic building block for graphitic materials of all other dimensionalities. One can wrap up graphene into large 0D fullerene, roll it into nanotubes or stack into few layers of graphene and eventually into 3D graphite [6, 7]. Graphene possesses many intriguing properties such as large electron mobility [8, 4] extremely high thermal conductivity [9] and extraordinary elasticity and stiffness [10]. These peculiar properties make graphene a great candidate to serve as new nanoscale building blocks to create unique nanoelectronic and nanoelectromechanical devices [11, 12].

Graphene yet has another interesting characteristic. Graphene sheets can be stacked on top of each other to form few-layer graphene where relatively weak, van der Waals forces keep the stack together [13, 14, 15, 16, 17, 18]. Graphene sheets consisting of few layers are naturally obtained in the process of fabrication [19]. Few-layer graphene combines outstanding electronic and mechanical properties [20, 21, 22]. As a very especial example of graphene hetero structures, Bernal stacked bilayer has particular potential for next-generation nanoelectronic applications owing to its peculiar electronic band structures [23]. Twisted bilayer as another stable form of bilayer graphene has also attracted significant attention from both theoretical as well as experimental researchers owing to its extraordinary optical [24, 25] and electronic properties [26, 27, 28]. Twisted bilayer graphene (tBLG) is fabricated by the stacking of two monolayers of graphene with a specific twisting angle (θ); The atomic orientation among the two layers affects interlayer coupling strength and the interlayer electron motion in the bilayer [29, 30, 31, 32]. As a result of tunable interlayer coupling and band structure, twisted bilayer exhibits extraordinary potential to be a key component of bilayer-based devices [33, 34, 35].

Similar attempts were made to obtain other 2D crystals such as hexagonal Boron Nitride (h-BN), metal dichalcogenides [36, 37] and hundreds of different 2D materials [38] in search of new phenomena and applications.

A practical approach to characterize graphene-based electronic devices is to build junctions and hybrid structures by connecting graphene flakes with different widths and orientations [39, 40, 41]. It is of paramount importance to study the transport properties of these hybrid structures as fundamental and crucial component of graphene-based circuits. Until now, many efforts have been made in exploring ballistic transport properties of graphene/bilayer junctions [42, 43, 44, 45, 46, 47, 48, 49]. These studies already revealed a high degree of tunability of the transport properties. However, the effects of further manipulations of the gate voltage, namely through the creation of a domain wall affecting the bilayer region [50] are yet to be investigated. Furthermore, the possibility of a microstructured gate voltage with several built-in domain walls opens up new avenues to engineer electronic transport at the nanoscale. The aim of this thesis is to study ballistic transport of micro-structured bilayer graphene flakes with different types of connection to monolayer. The thesis addresses the conductance characteristics of twisted bilayer in the ballistic regime, which, to the knowledge of the author, has not been fully addressed before.

1.2 Organization of the thesis

This section presents a brief review of the content of the thesis.

1.2.1 Summary of chapter 2

Chapter 2 contains the preliminaries needed to understand the following chapters. The chapter starts with a survey of literature on graphene and its unique band structure based on tight-binding model approximation. It also has a concise introduction to bilayer graphene and its different stacking, AA, AB, and twisted. The density of states as one of the principal quantities, which is considered in this thesis, is also briefly described. Chebyshev polynomials and their role in the kernel polynomial method for computing density of states is emphasized. Finally, we provide a discussion on the transport in mesoscopic systems and Landauer-Buttiker formalism for quantum transport.

1.2.2 Summary of chapter 3

We start Chapter 3 with a discussion of the importance of graphene-based hybrid structures and their presence in graphene production techniques as a natural product. As a pedagogy warm up exercise to study transport in complex heterostructures we explore the transport properties of one dimensional (1D) chain-ladder-chain. The simplicity of the 1D model helps us to establish our semi-analytical transfer matrix method to get the transmission and reflection coefficient. Next, we tackle the question of quantum transport in graphene-AB stacked bilayer-graphene. This is the main topic of the chapter. We study two main configurations of 2D hybrid structure using the methodology we developed for the 1D toy model. We conclude with a summary of the results. In the Appendix we present some of the calculation steps in detail.

1.2.3 Summary of chapter 4

In Chapter 4, we study quantum transport in twisted bilayer graphene. The structure of the system similar to that of Chapter 3 consists of monolayer-bilayer-monolayer, but where the AB stacked bilayer is replaced by a twisted bilayer. The methodology to get the transmission coefficients is purely numerical. We use the numerical results of transport and density of states to uncover the nature of charge transport in such a structure. We close the chapter with a discussion and a summary. Appendix provides a prescription to build the bilayer structure using a Python code.

1.2.4 Summary of chapter 5

Chapter 5 contains the concluding remarks and a summary of the work accomplished in this thesis. We also address some open questions which might be interesting for future studies.

1.3 Original content and external material

All the results presented in this thesis, except those of Chapter 2, were obtained by the author in collaboration with co-authors of the papers mentioned at the beginning of each section. All figures present in this text originate from the author's and his collaborators' work. The numerical algorithms coded by the author rely on external routines such as MUMPS [51] and Kwant open source package [52].The programming languages used were Python and Mathematica.

2 Theoretical framework and numerical methods

In this chapter, we provide the reader some background knowledge in graphene physics and the techniques we use in the following chapters to study electronic and transport properties. The chapter serves as a bridge to linking the result presented in the next chapters with previously existing framework.

2.1 Two-dimensional materials

There is an enormous amount of work on two dimensional (2D) materials, including theoretical research papers, programming packages, experimental findings, etc. This raises the question of why so much work and effort invested in this field of science and technology? What makes 2D materials so attractive? And why are their properties different from three dimensional (3D) materials? The answers to these questions are all based on the fundamental role of dimensionality as, in general, one may expect different properties in 2D materials as compared with their bulk form. Optical and electronic properties are usually different due to confinement of electrons but also due to the absence of interlayer interactions, that, despite being generally quite weak, play an essential role in determining band structure. As an example, we will see in the next sections that bilayer graphene has different electronic bandstructure than monolayer graphene, solely because of relatively weak interlayer interaction.

2.2 Single layer graphene

Graphene, a single layer of graphite, has been one of the first real two dimensional materials with one atom thickness to be isolated experimentally. During the last few decades, extensive effort was devoted to obtaining single-layer graphene sheets, with the purpose of having access to the properties of a tightly bond one-atom-thick layer of sp^2 carbon which had been predicted by theory. Not all the techniques could end up in isolation of graphene. Many of those techniques had been tested with only moderate success. Eventually, graphene was first isolated by Andre Geim's group at Manchester University in 2004 [38]. Surprisingly, the technique employed for obtaining real one atom thick layers with almost macroscopic lateral dimensions was straightforward. It consists of rubbing (HOPG) against another surface, similar to what happens when you use a pencil. With this technique, a variety of flakes leaves on the surface. Most of these flakes have more than ten layers, but notably, single sheets can also be found among the resulting structures . Although the synthesis of 2D materials includes several key routes: mechanical exfoliation, chemical exfoliation, and direct synthesis, to date, mechanical exfoliation turns to result in few-layer materials with higher quality that can exhibit almost ideal electronic behavior [19].

The exfoliation technique is simple, but the low production of monolayers with this method does not render it a reliable and economical technique. Hence, it is not technologically applicable. However, the technique is still useful for fundamental studies, as demonstrated by a large number of works carried out using this technique [53]. One significant result of obtaining single-layer graphene out of HOPG using the exfoliation method is that it proves that these high-quality flakes are stable under ambient conditions.

2.2.1 Single electron tight-binding model and reciprocal space

Most of the exceptional features of graphene are the result of its dimensionality and its very unique electronic bandstructure. The linear dispersion relation of electrons near the Fermi surface mimics relativistic particles [53]. Because of this linear dispersion relation, low energy electrons in graphene behave as massless Dirac Fermions [38].

In this section, we model the electronic structure of graphene using the so-called tight-binding approximation. We start by setting up some useful notation. The electronic structure of an isolated C atom is represented as $1s^2 2s^2 2p^2$; in a solid-state material, the $2s$ and $2p$ electrons hybridize while the $1s$ electrons remain more or less inert. One possible result of the hybridization of the $2s$ and $2p$ electrons is four sp^3 orbitals, which naturally turn to form a tetrahedral bonding structure that takes in all the valence electrons. This is precisely what happens in diamond, the best known solid form of carbon, which is a very good insulator (bandgap ~ 5 eV). Nonetheless, another possibility is to form three sp^2 orbitals, resulting in a p-orbital. In this scenario, the sp^2 orbitals arrange themselves in a plane at 120° angles, and the resulting lattice thus turns into a honeycomb lattice. In a honeycomb arrangement, there are two inequivalent sublattices, labeled as A and B, see Fig. 2.1, with the environment of the corresponding atoms being mirror images of one another. The Bravais lattice has primitive lattice vectors a_1 , a_2 as shown in Fig. 2.1, defined as

$$\mathbf{a_1} = \sqrt{3}a_{cc}\left(\frac{\sqrt{3}}{2}, \frac{1}{2}\right), \quad \mathbf{a_2} = \sqrt{3}a_{cc}\,(0,1)\ , \tag{2.1}$$

where a_{cc} is the nearest-neighbor C-C spacing ($\approx 1.42\,\mathring{A}$). For the sake of convenience, we set $\sqrt{3}a_{cc} = 1$ and measure the length unit with respect to this unit. We chose an atom in the A sublattice of graphene to be the reference atom of the unit cell. Thus, a given atom in the plane of graphene can be tracked according to its position, R_{nm}, as

$$\mathbf{R}_{mn} = \begin{cases} m\mathbf{a_1} + n\mathbf{a_2} & \text{if sublattice } A \\ m\mathbf{a_1} + n\mathbf{a_2} + \frac{1}{3}\left(\mathbf{a_1} + \mathbf{a_2}\right) & \text{if sublattice } B \end{cases} .$$

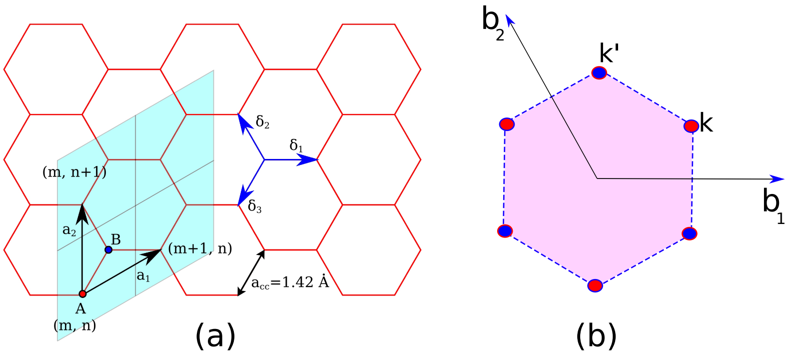

Figure 2.1: Schematic of graphene lattice and its Brillouin zone. (a) Shows the primitive vectors, $\mathbf{a_1}$ and $\mathbf{a_2}$ and the two atoms of the unit cell labeled by A and B. It also exhibits the way the cells are labeled by two indices (m, n). (b) The first Brillouin zone of graphene and reciprocal lattice primitive vectors shown by $\mathbf{b_1}$ and $\mathbf{b_2}$. The two special points, called Dirac points, labeled by $\mathbf{K}$ and $\mathbf{K}'$. Circles with similar color indicate equivalent Dirac points.

Accordingly, we call the reciprocal primitive vectors of graphene $\mathbf{b_1}$ and $\mathbf{b_2}$. These vectors are defined by the equation $\mathbf{a}_i \cdot \mathbf{b}_j = 2\pi\delta_{ij}$ and for our choice of lattice unit cell and primitive vectors the become,

$$\mathbf{b_1} = \frac{4\pi}{\sqrt{3}}\left(1, 0\right), \quad \mathbf{b_2} = \frac{4\pi}{\sqrt{3}}\left(-\frac{1}{2}, \frac{\sqrt{3}}{2}\right) . \tag{2.2}$$

These two vectors are essential in defining the Brillouin zone of graphene. We set the first Brillouin zone of the reciprocal lattice in the standard way, as bounded by the planes bisecting the vectors to the nearest reciprocal lattice points. This gives the first Brillouin zone (FBZ) of the graphene, which has the same form as the original hexagons of the graphene honeycomb lattice. The only difference is that the FBZ hexagon is rotated with respect to the original hexagons in graphene by $\frac{\pi}{2}$, see Fig. 2.1(b). The points at the corners of the FBZ consist of two groups of three points. Points in each group are equivalent, so we only consider one point from each group. There are labeled by K and K' as in the Fig. 2.1(b). Explicitly, their coordinates in momentum space are given by

$$\mathbf{K} = \frac{1}{3}\left(2\mathbf{b_1} + \mathbf{b_2}\right), \quad \mathbf{K'} = \frac{1}{3}\left(\mathbf{b_1} + 2\mathbf{b_2}\right). \tag{2.3}$$

These two special points are not equivalent, as there is no reciprocal lattice vector connecting them. This is clear as $\mathbf{K} - \mathbf{K'} = \frac{2}{3}\left(\mathbf{b_1} - \mathbf{b_2}\right)$ is not a reciprocal vector. It is convenient to note at this point that for an B-sublattice atom the three nearest-neighbor vectors in real space are given by

$$\boldsymbol{\delta_1} = a_{cc}\left(1, 0\right), \quad \boldsymbol{\delta_2} = a_{cc}\left(-\frac{1}{2}, \frac{\sqrt{3}}{2}\right), \quad \boldsymbol{\delta_3} = a_{cc}\left(-\frac{1}{2}, -\frac{\sqrt{3}}{2}\right). \tag{2.4}$$

The negatives of these vectors give the nearest neighbors of B-sublattice. We start by considering a tight-binding model with nearest-neighbor hopping only. The relevant atomic orbital is the single (p_z) (or more correctly π) C orbital which is left unfilled by the bonding electrons. This orbital is oriented normal to the plane of the graphene lattice. Each orbital can accommodate two electrons with two opposite spin projection ±1. If we denote an orbital by its position $\mathbf{R}_{m,n}$ on the plane and with the spin σ, then the nearest-neighbor tight-binding Hamiltonian takes the following form

$$H = -t \sum_{m,n,\sigma} b^{\dagger}_{\sigma}\left(\mathbf{R}_{m,n}\right)\left\{a_{\sigma}\left(\mathbf{R}_{m,n} + \boldsymbol{\delta_1}\right) + a_{\sigma}\left(\mathbf{R}_{m,n} + \boldsymbol{\delta_2}\right) + a_{\sigma}\left(\mathbf{R}_{m,n} + \boldsymbol{\delta_3}\right)\right\} + h.c.. \tag{2.5}$$

Where $a^{\dagger}\left(\mathbf{R}_{m,n}\right)$ and $b^{\dagger}\left(\mathbf{R}_{m,n}\right)$ are the creation of a particle with spin σ on an atom in position $\mathbf{R}_{m,n}$ on sublattice A and B, respectively. The numerical value of the nearest-neighbor hopping matrix element t, which sets the overall scale of the π-derived energy band, is believed to be about 2.8 eV [54]. Nonetheless, the exact value is unimportant for subsequent results.

We rewrite the latter Hamiltonian in a more compact form,

$$H = -t \sum_{m,n,\sigma} b^{\dagger}_{m,n,\sigma}\left\{a_{m,n,\sigma} + a_{m+1,n,\sigma} + a_{m,n+1,\sigma}\right\} + h.c.. \tag{2.6}$$

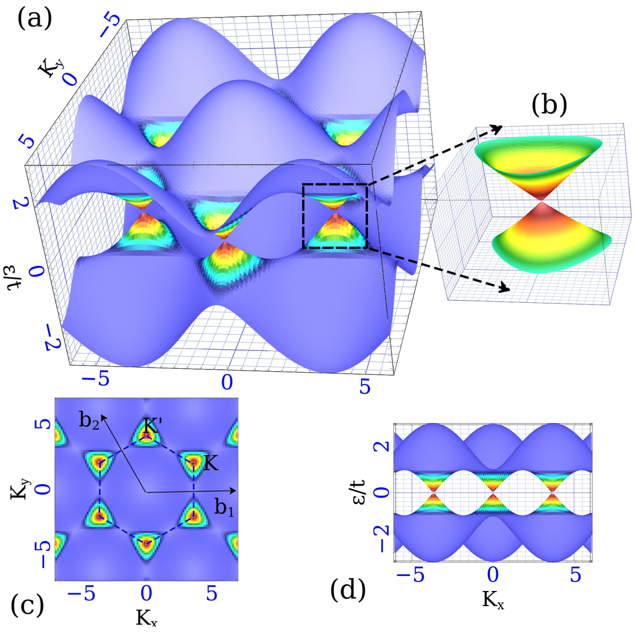

Figure 2.2: Graphene bandstructure. (a) shows the 3d plot of graphene bandstructure (b) exhibits the Dirac cone and the linear behavior of the dispersion near the charge neutrality point. (c) Top view of the bandstructure with superimposed reciprocal vectors and K pints. (d) The side view of the bandstructure.

To explore the nature of electronic states in graphene, we obtain its band structure, generated by the simple Hamiltonian Eq. (2.6). We diagonalize the latter Hamiltonian represented in creation and annihilation operators basis in order to get eigenenergies and, consequently, the band structure. Assuming periodic boundary conditions both in a_1 and a_2 directions and performing a Fourier transform along the two primitive vectors we end up with a 2×2 matrix, which is easy to diagonalize. We introduce two quantum numbers k_1 and k_2 where $k_1, k_2 \in [-\pi/a, \pi/a]$ and employ the Fourier transform in both primitive directions according to the following definitions,

$$a^{\dagger}(\mathbf{k}) = \frac{1}{\sqrt{N}} \sum_{\mathbf{r}} e^{i\mathbf{k}\cdot\mathbf{r}} a(\mathbf{r}),$$

$$b^{\dagger}(\mathbf{k}) = \frac{1}{\sqrt{N}} \sum_{\mathbf{r}} e^{i\mathbf{k}\cdot\mathbf{r}} b(\mathbf{r}).$$

By plugging these relations into Eq. (2.6) we obtain,

$$H = -t \sum_{k_1,k_2,\sigma} b_\sigma^\dagger (\mathbf{k})\, a_\sigma (\mathbf{k}) \left(1 + e^{i\mathbf{k}\cdot\mathbf{a_1}} + e^{i\mathbf{k}\cdot\mathbf{a_2}}\right) + h.c.\,. \tag{2.7}$$

The resulting Hamiltonian is a 2×2 matrix in the new basis $\Psi_{\mathbf{k}}^\dagger = \left[a^\dagger (k_1, k_2)\,, b^\dagger (k_1, k_2)\right]$ as,

$$H = -t \sum_{\mathbf{k},\sigma} \Psi_{\mathbf{k}}^\dagger \begin{bmatrix} 0 & f(\mathbf{k}) \\ f^*(\mathbf{k}) & 0 \end{bmatrix} \Psi_{\mathbf{k}} = \sum_{\mathbf{k},\sigma} \Psi_{\mathbf{k}}^\dagger H(\mathbf{k})\, \Psi_{\mathbf{k}}\,, \tag{2.8}$$

with $f(\mathbf{k}) = 1 + e^{i\mathbf{k}\cdot\mathbf{a_1}} + e^{i\mathbf{k}\cdot\mathbf{a_2}}$. Diagonalization of $H(\mathbf{k})$ results in the eigenvalues of the system labeled by quantum number $\mathbf{k}$,

$$\varepsilon(\mathbf{k}) = \pm |f(\mathbf{k})| = \sqrt{3 + 2\cos(\mathbf{k}\cdot\mathbf{a_1}) + 2\cos(\mathbf{k}\cdot\mathbf{a_2}) + 2\cos(\mathbf{k}\cdot(\mathbf{a_2} - \mathbf{a_1}))}\,.$$

It is convenient to write the TB orthogonal eigenmodes in the form of a spinor as,

$$\psi_{\mathbf{k}}^\pm = \frac{1}{2} \begin{pmatrix} 1 \\ \pm\frac{f^*(\mathbf{k})}{|f(\mathbf{k})|} \end{pmatrix}\,, \tag{2.9}$$

whose components correspond to the amplitudes on the A and B atoms respectively within the unit cell labeled. For each $\mathbf{k}$ there are two bands in the graphene bandstructure. These two bands, as it is shown in Fig. 2.2 have two peculiar properties. First, they touch each other at the corners of the first Brillouin zone, while gapped in the other regions and second, near the Fermi point where they meet, the dispersion relation is linear and isotropic in $\mathbf{k}$. Conventional semiconductors have gaps in their bandstructure, but the bandgap in graphene closes at Fermi point. In the next section, we show how one can engineer the band structure of graphene by introducing boundary disorders.

2.2.2 Graphene ribbons

Isolated graphene flakes have finite sizes and, consequently, edges known to be in general of two primary forms, zigzag or armchair. In this section, we focus on the electronic properties of graphene nanoribbons (GNRs). One can see them as the result of broken translational invariance in either one or two directions in an infinite graphene sheet. Depending on how the translational invariance is broken, one can get the so-called zigzag or armchair nanoribbons, ZGNR and AGNR, see

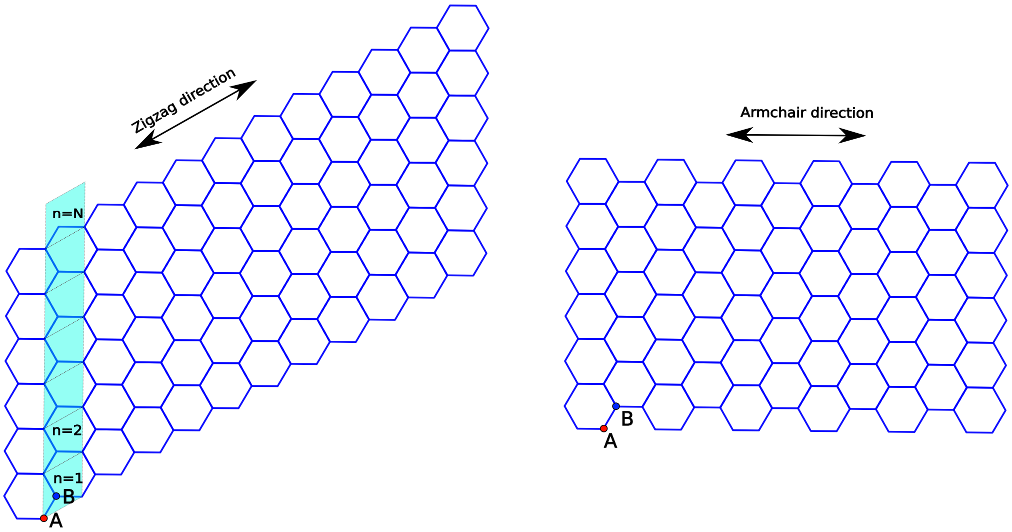

Figure 2.3: The two types of edges in graphene are shown. (a) Zigzag edge ribbon. Light blue rhombus is the construction bloc of ribbon. (b) Armchair edge ribbon.

Fig. 2.3. They have a 30° difference in their orientation within the lattice. Ribbons are narrow and straight-edged stripes of graphene, which are infinite in one direction while restricted in the other direction. The structure of the edge plays a major role in these electronic properties. In the scope of this work, we will only focus on the ZGNR type. The hybrid structure of monolayer-bilayer graphene (MBM), of which we will study the transport properties, is a compound system out of a wide zigzag edge ribbon and a bilayer region. As shown in Fig. 2.3, the ribbon has a width of N unit cell. Similar to the Hamiltonian of the graphene sheet, we Fourier transform the Hamiltonian, Eq. 2.6, in the direction with translational invariance. So, we can write the tight-binding Hamiltonian of ZGNR

$$\begin{aligned} H\left(k_1\right) = & -t \sum_{n=1,\sigma}^{N-1} b_{n,\sigma}^{\dagger}\left(k_1\right)\left\{a_{n,\sigma}\left(k_1\right)\left(1+e^{ik_1}\right)+a_{n+1,\sigma}\left(k_1\right)\right\} \\ & - t b_{N,\sigma}^{\dagger}\left(k_1\right) a_{N,\sigma}\left(k_1\right)\left(1+e^{ik_1}\right)+h.c, \end{aligned} \tag{2.10}$$

where k_1 is momentum in $\mathbf{a_1}$ direction. For a given quantum number k_1 we numerically diagonalize the Hamiltonian above. The result is shown in Fig. 2.4 . By increasing the width of the ribbon, as it is shown on the right panel, we end up in a region which determines the number of available states for a given energy. In fact, one could see the right panel as the projection of graphene band structure onto a plane normal to $\mathbf{b_2}$ primitive vector. Note that no gap appears in the bandstructure, so ZGNRs are always metallic.

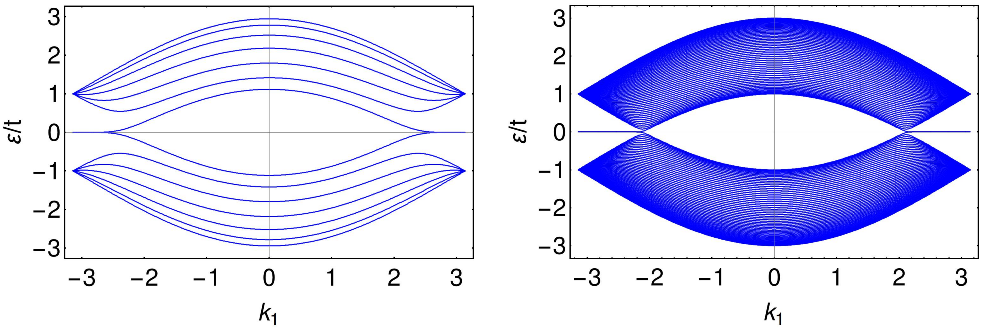

Figure 2.4: Band structure of zigzag edge nanoribbon with 14 and 122 atom thickness. The zero energy flatband is due to the boundaries. Note that no gap is present in this case for any given width of the ribbon

2.3 Bilayer graphene

This section includes a brief introduction to bilayer graphene. As we mentioned in the previous section, exfoliation of graphene out of HOPGs can also result in few-layer graphene. Bilayer graphene consists of two single-layer graphene sitting on top of the other layer binding by van der Waal (vdW) interaction. Bilayer graphene can exist in three different stacking. The three different configurations of the layers are called AA, AB, and twisted bilayer graphene. The AA stacked bilayer [55] is probably the simplest form of the bilayer in which each carbon atom of the top layer is placed precisely above the corresponding atom of the bottom graphene sheet. However, the AA stacked structure is likely to be metastable, and only a few authors reported manufacturing AA samples. In the AB bilayer, which is also called Bernal stacking, half of the carbon atoms of the top layer are above the atoms of the bottom layer, while other atoms located above the centers of the bottom layer hexagons. This is the usual order which happens in graphite in nature. The Bernal stacked bilayer graphene is considered as the most stable phase [56]. High-quality flakes of Bernal stacked graphene are produced and studied in many experiments.

The third type of bilayer graphene structure-twisted bilayer-consists of top graphene layer rotated with respect to the bottom layer by some angle θ [34, 57, 58]. Such a configuration of layers is also stable as the twisted flakes are produced. The electronic properties of the bilayer structures in different stacking are different. Hence, in the following subsections, we will consider the tight-binding model of each of them separately. Our focus will be on Bernal stacked and twisted bilayer graphene and exploring their transport properties in hybrid structures of monolayer-bilayer-monolayer (MBM). The theory of single-layer graphene is beneficial in understanding the electronic properties of its bilayer form. In fact, the theories of electronic properties of the bilayer graphene are built upon those of the electronic structure of graphene [54]. In the previous section, it was established that, for single-layer graphene, the sp^2 hybridization between the carbon s orbital and two p orbitals results in the formation of a σ bond between adjacent atoms. Indeed, the robustness of the lattice structure in all carbon allotropes is directly due to σ bonds. It is also mentioned that these bands have a filled shell because of the Pauli principle, which gives rise to a valence band. The p_z orbital, which is perpendicular to the graphene plane, binds covalently with carbon atoms nearby and leads to a so-called π band. Since every p orbital hosts one extra electron, the π band is half-filled. In Bernal stacked bilayer graphene hybridization of π bands of single-layer graphene forms the vdWs interaction between the layers and sticks the two layers together. In the twisted phase, the interlayer interaction is due to a combination of π and σ bands. The interlayer spacing in the AB bilayer is estimated [59] as $c = 3.35\,\AA$ in the equilibrium configuration. In the AA stacked and twisted bilayer cases, the interlayer separation could be somewhat different. The nature of the interaction between graphene sheets in bilayer graphene was analyzed by many authors [60, 61, 62, 63, 64].

The Hamiltonian of bilayer graphene may be viewed as a generalization of the graphene Hamiltonian, which results in a more complicated picture of electron and hole dispersion. For instance, the dispersion relation of AB stacked bilayer demonstrates parabolic shape at low energies, which is different from the linear behavior of graphene dispersion relation. The electronic dispersion relation of bilayer graphene can be engineered to develop a bandgap. Depending on a particular situation, the gap in the spectrum can be controlled by doping, gate voltage [65, 66]. From the point of view of electronic application, the feasibility of having a graphene-based system with a controllable gap is of great importance and interest in designing graphene-based transistors. While many macroscopic properties of bilayer graphene are similar to that of the monolayer, for some applications, due to larger possibilities for tuning their physical properties, bilayer graphene may have specific advantages over the monolayer. Here we end our general review of bilayer physics. A reader interested in more specialized aspects of the graphene bilayer may consider more topical works. For transport properties of bilayer graphene, one may look at the paper of Das Sarma et al. [67]. Bilayer photonics applications are discussed in Ref. [68]. There is a review paper by T. Stauber in Ref. [69] regarding plasmons in graphene-based systems. Ref. [70] has a review of nonlinear optical phenomena of single-layer, and Bernal stacked bilayer. There is a short review on twisted bilayer in Ref. [71]. Ref. [72] contains a detailed study of electronic and optical properties of twisted bilayer graphene.

2.3.1 AB-stacked bilayer graphene

In this thesis, we focus on Bernal-stacked bilayer graphene. As it is more stable and more commonly found in nature, it can be assumed any reference to bilayer graphene is that of a Bernal stacked formation. Following our discussion from previous sections, two graphene sheets typically take an AB-stacked formation, more commonly know as Bernal stacking, in which the A atoms in one layer are stacked below the B atoms in the upper layer such that the A atoms in the upper layer sit above the center of the hexagons formed in the lower layer, see Fig. 2.5. Like the monolayer, Bernal-stacked bilayer graphene also possesses remarkable properties. One of the most striking characteristics of bilayer graphene is its band structure tunability. In fact, when the bilayer is placed in an appropriately configured field-effect device, a tunable semiconducting gap can be generated. This causes the valence and conduction bands to no longer meet at the two Dirac points, see Fig. 2.7, in the graphene Brillouin zone [20, 65, 73, 74, 75]. In this section, we will give a tight-binding description of AB-stacked bilayer graphene and study the unique features of its band structure with a quantitative approach.

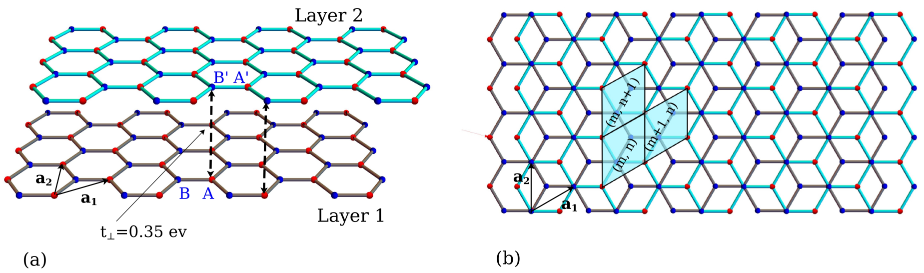

Figure 2.5: Bilayer graphene lattice. (a) Shows the AB-stacked bilayer graphene and the interlayer hopping $t_\perp = 0.35\,\text{eV}$ between A and B_1 atoms. (b) Exhibits the unit cell of bilayer graphene and the primitive vectors a_1 and a_2. The tuple (m, n) label the unit cells within the lattice.

2.3.1.1 Single electron tight-binding model

We begin our discussion of Bernal-stacked bilayer graphene by constructing the corresponding tight-binding Hamiltonian. The model we will use is similar to that of the monolayer, where we allow intralayer hopping between nearest neighbors and interlayer hopping between sites of AB stacking in the two layers indexed layer 1 and layer 2, see Fig. 2.5. As we now have two layers, we will have four atoms per unit cell and thus expect four energy bands. The tight-binding model of a single electron in AB-stacked bilayer graphene can be written as the sum of three Hamiltonians as,

$$H = H_1 + H_2 + H_\perp, \tag{2.11}$$

where H_1 and H_2 are the Hamiltonian of the first layer and the second layer, respectively. We use the term “first layer” to refer the bottom layer and “second layer” to call the top layer. The third term, $H_\perp$, is the interaction between the two layers. Similar to the case of graphene we use the indices m and n to label the unit cell of the bilayer graphene. The single-layer Hamiltonian reads,

$$H_l = -t \sum_{m,n,\sigma} b^\dagger_{l,m,n,\sigma} \left\{ a_{l,m,n,\sigma} + a_{l,m+1,n,\sigma} + a_{l,m,n+1,\sigma} \right\} + h.c. \qquad l = 1,2 \tag{2.12}$$

with l being the label for layers and $a^\dagger_{l,m,n,\sigma}$ $\left(b^\dagger_{l,m,n,\sigma}\right)$ creates an electron at the position

$$R^l_{mn} = \begin{cases} m\mathbf{a_1} + n\mathbf{a_2} & \text{if sublattice } A \\ m\mathbf{a_1} + n\mathbf{a_2} + \frac{1}{3}\left(\mathbf{a_1} + \mathbf{a_2}\right) & \text{if sublattice } B, \end{cases}$$

With $t_\perp = 0.35\,\text{eV}$ being the interlayer hopping energy the interlayer Hamiltonian $H_\perp$ for the AB-stacked bilayer graphene is

$$H_\perp = -t_\perp \sum_{m,n,\sigma} a^\dagger_{1,m,n,\sigma} b_{2,m,n,\sigma} + h.c. \tag{2.13}$$

Assuming periodic boundary conditions, a Fourier transform of the creation and annihilation operators transforms the total Hamiltonian into

$$H = \sum_{\mathbf{k},\sigma} \Psi^\dagger_{\mathbf{k}} H\left(\mathbf{K}\right) \Psi_{\mathbf{k}} \tag{2.14}$$

in the reciprocal space representation where

$$H\left(\mathbf{K}\right) = -t \begin{bmatrix} 0 & f\left(\mathbf{k}\right) & 0 & \frac{t_\perp}{t} \\ f^*\left(\mathbf{k}\right) & 0 & 0 & 0 \\ 0 & 0 & 0 & f\left(\mathbf{k}\right) \\ \frac{t_\perp}{t} & 0 & f^*\left(\mathbf{k}\right) & 0 \end{bmatrix} \tag{2.15}$$

is represented in the following basis

$$\Psi_{\mathbf{k}} = \begin{bmatrix} a_1\left(\mathbf{k}\right) \\ b_1\left(\mathbf{k}\right) \\ a_2\left(\mathbf{k}\right) \\ b_2\left(\mathbf{k}\right) \end{bmatrix}. \tag{2.16}$$

Solving the Schrödinger equation

$$H\left(\mathbf{k}\right)\left|\psi\left(\mathbf{k}\right)\right\rangle = \varepsilon\left(\mathbf{k}\right)\left|\psi\left(\mathbf{k}\right)\right\rangle$$

yields the following eigenvalues and corresponding eigenvectors,

$$\varepsilon_{r,s}\left(\mathbf{k}\right) = r\frac{t_{\perp}}{2t} + s\sqrt{\left(\frac{t_{\perp}}{2t}\right)^{2} + \left|f\left(\mathbf{k}\right)\right|^{2}}\,, \tag{2.17}$$

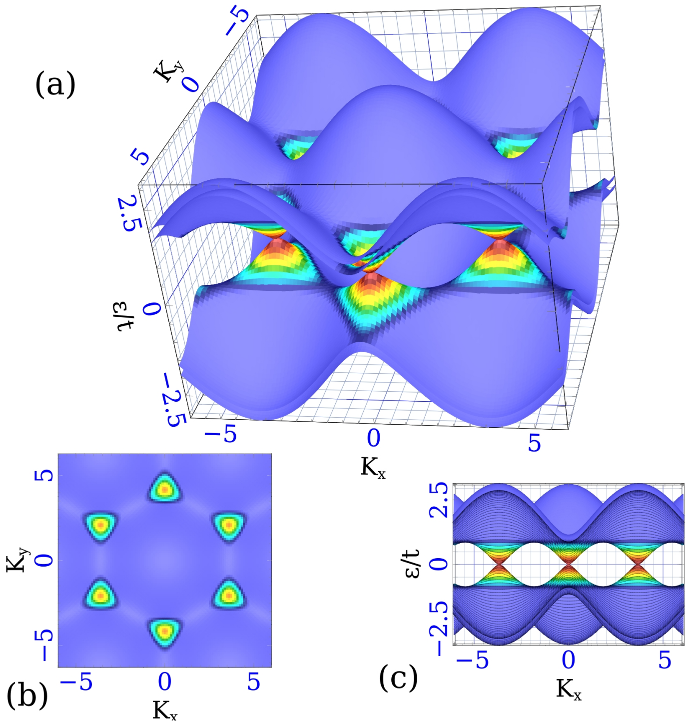

Figure 2.6: Bilayer graphene band structure. (a) Shows the **k** dependent 3D plot of four-band AB stacked bilayer graphene band structure. Due to broken sublattice symmetry, the sublattice degeneracy is lifted, and the bilayer develops a four-band band structure. (b) Top view of the band structure and the FBZ of the bilayer. Note that at the Dirac cone in the corners of BZ the band two parabolic bands meet. (c) Side view of 3D band structure exhibits the parabolic behavior of the dispersion relation at low energies near the Dirac point.

where $r, s \in \{-1, 1\}$. The corresponding eigenvectors can be represented as the column vector of,

$$\left|\psi_{r,s}\left(\mathbf{k}\right)\right\rangle \equiv \begin{bmatrix} r \\ \frac{\varepsilon_{r,-s}}{f(\mathbf{k})} \\ \frac{f(\mathbf{k})}{\varepsilon_{r,s}} \\ -r \end{bmatrix}. \tag{2.18}$$

Due to the nonzero interlayer hopping $t_\perp$, the broken sublattice symmetry in AB stacked bilayer graphene lifts the sublattice energy degeneracy and the bandstructure now shows a parabolic behavior at low energies, see Fig. 2.6. This is why electrons in AB bilayer is usually called massive fermions as their dispersion relation resembles that of particles with nonzero mass.

2.3.1.2 Effect of bias gate voltage and tunable bandgap

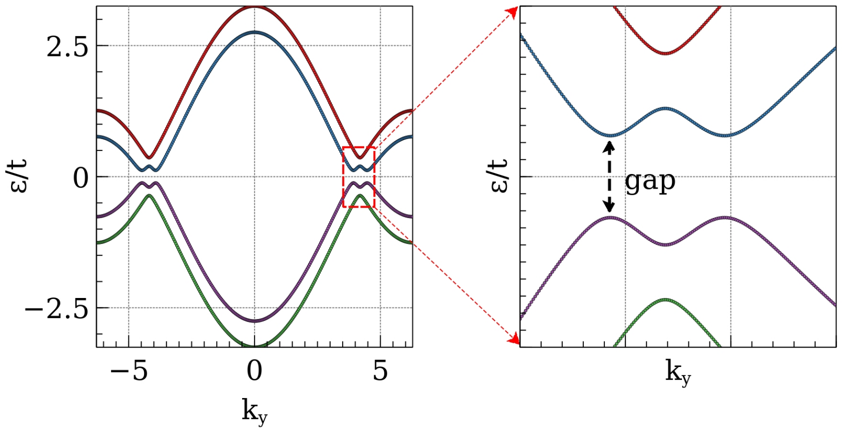

Figure 2.7: Biased bilayer graphene

When the two graphene planes are subjected to different electrostatic potentials, there is a breaking of symmetry between the two layers [76, 77, 78, 20]. The new Hamiltonian becomes the

$$H\left(\mathbf{k}\right) = -t \begin{bmatrix} \frac{V}{2} & f\left(\mathbf{k}\right) & 0 & \frac{t_\perp}{t} \\ f^*\left(\mathbf{k}\right) & \frac{V}{2} & 0 & 0 \\ 0 & 0 & -\frac{V}{2} & f\left(\mathbf{k}\right) \\ \frac{t_\perp}{t} & 0 & f^*\left(\mathbf{k}\right) & -\frac{V}{2} \end{bmatrix}, \tag{2.19}$$

where the onsite potential is defined as $-\frac{V}{2}$ and $\frac{V}{2}$ for the top and bottom layers, respectively.

$f\left(\mathbf{k}\right)$ is the same as for graphene. Diagonalization of the Hamiltonian above results in the following dispersion relation

$$\varepsilon_{r,s}\left(\mathbf{k}\right) = r\sqrt{2\left(\frac{t_\perp}{2t}\right)^2 + 2s\sqrt{\left(\frac{t_\perp}{2t}\right)^4 + |f\left(\mathbf{k}\right)|^2\left(\left(\frac{V}{2}\right)^2 + \left(\frac{t_\perp}{2t}\right)^2\right)}}, \quad r,s \in \{-1,1\} \tag{2.20}$$

The latter four-band dispersion relation shows the opening of a bandgap as it is shown in Fig. 2.7. The height of the bandgap changes as the onsite potential, $\frac{V}{2}$, varies. Note that the actual size of the gap is not necessarily equal to the externally applied potential difference V. Ref. [79] contains a discussion about the gap height and the self-consistent determination of the gap size.

2.3.2 Twisted bilayer graphene and emergent Moiré pattern

After we discussed the simple bilayer systems, namely the AB bilayers, we now explore the more complex phase of bilayer graphene called twisted-bilayer, see 2.8(a). Before diving into the electronic properties and underlying atomic geometry of twisted bilayer graphene, we first consider the experimental realization of such systems. Whenever two simple translationally periodic lattices are rotated with respect to each other, a new superstructure emerges, which is generally known as a Moiré pattern.

In the context of carbon systems, the existence of Moiré patterns has been observed a long time ago in graphite. Small-angle rotation faults, which exist naturally in graphite crystals due to the weak vdW interaction of the layers, are manifested via the long-periodic Moiré patterns, which have been observed with (STM) since 1990 [80, 81, 82].

Here we address two different contexts in which the relative rotation between two layers of graphene occurs and gives rise to Moiré patterns. One way of getting twisted bilayer graphene is by chemical exfoliation of highly ordered pyrolytic graphite. In this process, first, single layers of graphene are obtained by the exfoliation mechanism producing a suspension of single layers of graphene flakes [83, 84]. In the next step, when the flakes are deposited onto a substrate, the single-layer flakes may stick to each other with a rotational misalignment yielding twisted flakes [84, 85].

Moiré patterns can also be induced by depositing graphene onto a substrate whose lattice constant is different from that of graphene. For instance, vertical stacking of hexagonal boron nitride (hBN) and graphene can also give rise to Moiré patterns, thus producing a bilayer hybrid system with a large-scale Moiré structure. One interesting point regarding this hybrid structure is that there is a similarity between the atomic structure of graphene and hBN and in particular due to the weak interlayer bonding, the electronic features of graphene are preserved [86, 87, 88]. It has been shown that as a result of the small lattice mismatch between hBN and graphene ($\Delta a = 1.8\%$ [89]), a Moiré structure with a periodicity of about $\sim 14\,nm$ is present even without a mutual rotation. The particulary interesting feature of large Moiré periodicity is that such a system is ideal for studying the effect of a long periodic potential on the electronic structure. Many of the cited articles, as well as Chapter 4 of this thesis, consider twist bilayers, reveal a pronounced influence of the Moiré structure on the electron spectrum and on transport properties.

Commensurability in twisted bilayer

It is important to note that, in general, not any relative rotation of the layers yields a periodic system. The existence of a perfect periodicity, or in another words, translational symmetry, is necessary to employ Bloch's theorem, which significantly simplifies the calculation of the electronic structure. Although, the exact periodicity is still possible for some special rotation angles, the translational invariance is revoked for twisted bilayer structures. Structures that preserve translational invariance are called commensurate. Commensuration conditions are known to arise for angles $\theta = \theta_{mr}$ such that:

$$\sin\left(\frac{\theta_{mr}}{2}\right) = \frac{r}{2\sqrt{3m^2 + 3mr + r^2}}\,, \tag{2.21}$$

where m and r are mutually prime natural numbers. The detailed derivation of the latter condition can be found in the article by Shallcross et al. [90]. A similar derivation was presented by Lopes dos Santos et al. in [34] and more generally in a later work [57]. An example of a commensurate structure is given in Fig. 2.8(a) for rotation angles of $\theta = 21.73°$. Note that for this angle the Moiré is the supercell of the tBLG. This example has the smallest supercell, among the commensurate structures with $r = 1$, with only $N = 14$ atoms/layer. For smaller commensurate angles, the supercell can host thousands of atoms.

2.3.2.1 Single electron tight-binding model

Similar to AB stacked bilayer graphene, the single electron tight-binding model of tBLG can be seen as the sum of three Hamiltonians as $H = H_1 + H_2 + H_{12}$ where $H_{1(2)}$ is the single layer Hamiltonian of the first (second) layer and H_{12} describes the interaction of the layers. Unlike the Bernal stacked bilayer in which the interlayer hopping $t_\perp$ is constant over the graphene bilayer plane, in the twisted case, the interlayer hopping energy has a spatial distribution. A generic form of the interlayer hopping Hamiltonian can be written as,

$$H_{12} = \sum_{c\in\{A,B\}} \sum_{|R_1-R_2|<r} t_\perp\left(R_1, R_2\right) c_1^\dagger\left(R_1\right) c_2\left(R_2\right) + h.c. \tag{2.22}$$

where $R_1\left(R_2\right)$ runs over the lattice points in the first (second) layer and r is the vicinity radius, see Fig. 2.8(b). Atom C_1 is connected to atom C_2 if their spatial separation is less than r. This is to decrease computation costs. The position-dependent $t_\perp\left(R_1, R_2\right)$ determines the interlayer hopping between a pair of atoms sitting on different layers. It is usually a fast decaying function of the distance between the two atoms. In Chapter 4 we give an explicit expression for $t_\perp$.

In general, the corresponding Schrodinger equation of the total Hamiltonian H of tBLG can only be solved numerically. At low energies, some semi-analytical approaches can also be employed to derive quasi-band structures for tBLG [72]. In this thesis, we will mostly rely on numerical analysis so we will not consider those semi-analytic analysis.

2.3.2.2 Van Hove singularities in tBLG

The low energy bandstructure calculations for tBLG has shown that its bandstructure is similar to that of graphene [72]. The theory also predicted that the linear dispersion relation near the Fermi level is present with a suppressed Fermi velocity. In fact, the avoided crossing of the two Dirac cones of the layers decreases the band velocity, which gives rise to saddle points in the bandstructure of tBLG, see Fig. 2.8(d), and consequently to two singularities in the density of states (DOS), known as Van Hove Singularities (VHS). [91, 92, 93, 94]. For smaller angles $< 2°$ the suppression of the Fermi velocity continues until the appearance of a flatband, with very small or no dispersion, gives rise to a sharp DOS peak in the vicinity of Dirac point [58]. This weakly dispersive flatbands happen at the so-called magic angles [95, 57, 96, 91, 90], see Fig. 4.8.

2.4 Density of states: kernel polynomial method

The density of states $\rho\left(\varepsilon\right)$ is the number of electrons with particular energy, say, ε. It is succinctly described by the Dirac δ-function expression. Denoting by $\{\varepsilon_n\}$ and $\{|n\rangle\}$ the eigenvalues and eigenvectors of a Hamiltonian $\hat{\mathcal{H}}$ that describes the dynamics of an electron system, the DOS is

$$\rho\left(\varepsilon\right) \propto \sum_n \delta\left(\varepsilon - \varepsilon_n\right) = Tr\left[\delta\left(\varepsilon - \hat{\mathcal{H}}\right)\right]. \tag{2.23}$$

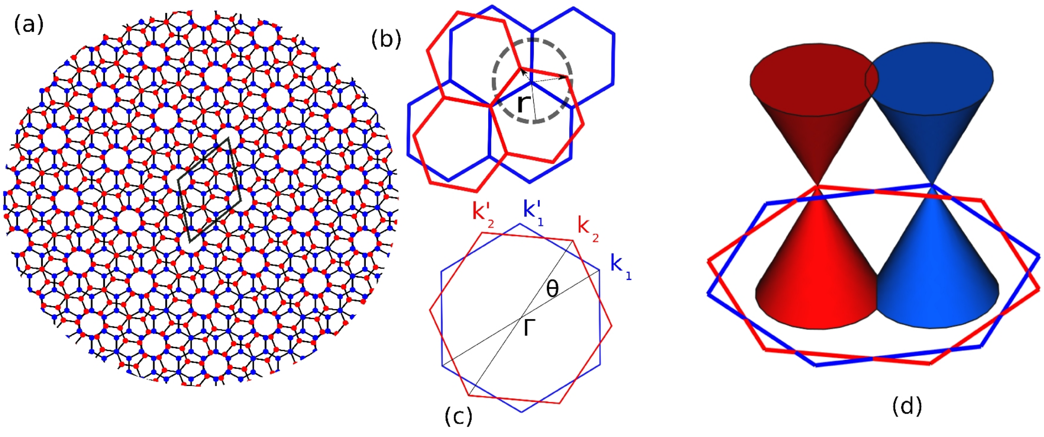

Figure 2.8: Twisted bilayer graphene. (a) A circular region of the tBLG superlattice for the commensurate angle structure of $\theta = 21.7868°$. The black rhombus is the unit supercell of the lattice. Blue (red) dots are the atoms of the first (second) graphene layer. Interlayer hoppings are not plotted. (b) The vicinity circle with a radius, r, is shown. Atoms from both layers are linked if they fall in the vicinity circle. (c) The relative rotation of FBZs of the two layers is shown where K_1 (K_2) is the Dirac point of the first (second) layer. (d) The voided crossing of Dirac cones of two layers and Van Hove points are shown.

Exactly calculating the DOS implies the diagonalization of the Hamiltonian matrix. However, the computational resources used by diagonalization algorithms scale up rapidly with system size as L^3, which makes it challenging to model large systems. This has placed great importance on the development of more efficient exact algorithms as well as novel approximative methods. A fundamentally different approach is to set aside the requirement for exact solutions (avoid diagonalization altogether) and instead use approximative methods to calculate the properties of interest. In this section, we present one such approach, the kernel polynomial method (KPM), based on Chebyshev polynomials expansion. One of the most desirable properties of KPM is computation time, which scales linearly with sparse matrix size N_{nz} . The procedure is numerically very stable, so no additional computation is wasted [97]. The approximative nature of the method presents an opportunity for additional performance tuning. Results may be computed very quickly at low accuracy to get an initial estimate for the problem at hand. Once the final results are required, the accuracy can be increased at the cost of longer computation time. KPM has been successfully applied to large quantum problems in solid-state physics [98, 99]. It can also be used to approximate the local density of states within a tight-binding framework [100].

The expansion of a function in terms of Chebyshev polynomials is of the following form, see Appendix 2.5.1,

$$f\left(x\right)=\frac{1}{\sqrt{1-x^2}}\left(\mu_0+\sum_{n=1}^{\infty}\mu_nT_n\left(x\right)\right) \tag{2.24}$$

with

$$\mu_n=\int_{-1}^{1}dxf\left(x\right)T_n\left(x\right) \tag{2.25}$$

and T_ns are the Chebyshev polynomials of the first kind and can be obtained using the following recursive relation,

$$T_{n+1}\left(x\right)=2xT_n\left(x\right)-T_{n-1}\left(x\right), \tag{2.26}$$

and

$$T_0\left(x\right)=1,\ T_1\left(x\right)=T_{-1}\left(x\right)=x\ .$$

Chebyshev polynomials stand out as a very good choice for numerical applications. They have good convergence properties and a close relation to the Fourier transform, which allows the partial reuse of existing numerical tools. Furthermore, the recursive relationship between Chebyshev polynomials enables the development of a very efficient iterative routine for computing the expanded function.

The expansion Eq. (2.24) exactly replicates function $f(x)$ by using an infinite series of polynomials. However, if a finite series is used instead, the expansion is only an approximation of $f(x)$. This is the case for numerical implementations where the order cannot possibly be infinite. For an efficient numerical solution, the key is to find a finite set of moments μ_n which gives the best estimate of the desired function. The simplest approximation is just to truncate the infinite series, limiting the expansion to the first N moments,

$$f\left(x\right)\approx\frac{1}{\sqrt{1-x^2}}\left(\mu_0+\sum_{n=1}^{N}\mu_nT_n\left(x\right)\right)\ . \tag{2.27}$$

A common feature of basically all Chebyshev expansions is the requirement for a rescaling of the underlying matrix or Hamiltonian $\hat{\mathcal{H}}$. In principle, the Chebyshev polynomials of both first and second kind are defined on the real interval $[-1,1]$, whereas the quantities we are interested in depend on the eigenvalues $\{\varepsilon_n\}$ of the considered (finite-dimensional) matrix. To fit this spectrum into the interval $\{\varepsilon_n\}$ we apply some linear transformation to the Hamiltonian and all energy scales. We use the following scaling transformations:

$$\varepsilon \to \tilde{\varepsilon} = \frac{\varepsilon - \varepsilon_0}{W}\,, \tag{2.28}$$

$$\varepsilon_n \to \tilde{\varepsilon_n} = \frac{\varepsilon_n - \varepsilon_0}{W}\,, \tag{2.29}$$

$$\hat{\mathcal{H}} \to \hat{h} = \frac{\hat{\mathcal{H}} - \varepsilon_0}{W}\,, \tag{2.30}$$

where ε_0 is the middle point of the energy spectrum of $\hat{\mathcal{H}}$. This corresponds to rescale the spectrum of $\hat{\mathcal{H}}$ into the range $[-1, 1]$, i.e., ϵ, $\epsilon_n \in [-1, 1]$. We rewrite the equation (2.23) in the following form.

$$\begin{aligned} \rho(\varepsilon) &= \frac{s}{\Omega_a} \sum_n \delta(\varepsilon - \varepsilon_n) = \frac{s}{\Omega_a} \sum_n \langle n|\delta\left(\varepsilon - \hat{\mathcal{H}}\right)|n\rangle \\ \rho(\tilde{\varepsilon}) &= \frac{s}{\Omega_a W} Tr\left(\delta\left(\tilde{\varepsilon} - \hat{h}\right)\right)\,, \end{aligned} \tag{2.31}$$

where $s = 2$ is for the spin degeneracy, Ω_a is the area associated with each atom in the material sample, i.e., $a = c/N_a$ where c is the sample area, N_a is the total number of atoms, W is the energy bandwidth, and the symbol "$Tr[...]$" denotes the trace of operator. In this way we can use the Chebyshev polynomial series to represent operator functions.

Before looking at the moments for the DOS function, it is important to note that the eigenvalues of $T_n\left(\hat{h}\right)$ are $T_n(\tilde{\varepsilon})$. This relation actually is valid for all polynomials and is not a specific property of the Chebyshev polynomials. Applying this to the momentum expansion, we get

$$\begin{aligned} \mu_n &= \int_{-1}^{1} d\tilde{\varepsilon} \rho(\tilde{\varepsilon})\, T_n(\tilde{\varepsilon}) \\ &= \frac{s}{\Omega_a W} \int_{-1}^{1} d\tilde{\varepsilon} Tr\left(\delta\left(\tilde{\varepsilon} - \hat{h}\right)\right) T_n(\tilde{\varepsilon}) \\ &= \frac{s}{\Omega_a W} Tr\left(T_n\left(\hat{h}\right)\right)\,. \end{aligned} \tag{2.32}$$

An additional numerical simplification consists of a statistical approach to calculate moments of the trace form efficiently. This together with Eq. (2.26) can be used to compute the momenta of the distribution. We will not dive into the details of the statistical approach here as it is a well-known concept, and we will not implement it directly in our calculations and computer programs. We use Kwant [52], which is a free Python package to compute the DOS whenever needed. In Kwant, the user can either set the number of moments N or the desired energy resolution in order to get the DOS. An example of Python code is given in Appendix.

2.5 Quantum transport

Historically, the Drude-Sommerfeld model of transport in solid state physics was one of the first breakthroughs that shed light on the electric and thermal conduction in metals. The model was based on the idea that Fermi-Dirac distribution applies for electrons in metals and only those electrons who are close to the Fermi level contribute to the conduction. The semiclassical Drude-Sommerfeld theory could explain Ohm's law in metals. It related the conductance to material's specific quantities, such as the electron density and their scattering rate and to the geometry of a specific sample [101].

A full quantum mechanical picture of electronic transport was established between 1950 and 1960. Kubo and Greenwood developed a quantum theory of the conductance based on linear response theory, which is known as Kubo–Greenwood formula for the electrical conductance [102, 103, 104]. At about the same time Landauer proposed a different theoretical view on quantum transport [105]. He related the electric current to the transmission probability of an electron that moves from the source contact and scatters through a sample into the drain contact [106].

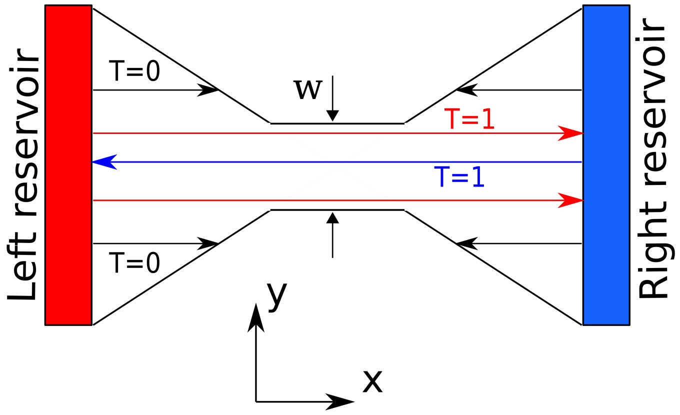

Figure 2.9: Schematic of ballistic transport in a scattering free 1D channel. $k > 0$ denotes positive velocity and gives a sense of current direction from left to right.

Before providing a general formulation of quantum charge transport in semiconductor nanostructures, let us consider a scattering free two terminal device as it is shown in Fig. 2.9. We define the current as sum of all available channels as,

$$I = 2 \sum_{n \in \{L,R\}} \int_{-\infty}^{\infty} \frac{dk_x}{2\pi} ev\left(k_x\right) f_n\left(k_x\right), \tag{2.33}$$

with the electron velocity being $v_x = k_x/m$. The filling factors $f_{L.R}\left(k_x\right)$ are different for open $(T = 1)$ and closed $(T = 0)$ channels, see Fig. 2.9, where T is the channel transmission. If the channel is closed, all electrons passing the cross-section from the left are reflected from the barrier and subsequently pass the same cross-section from the right. Therefore, in a closed channel there is the same amount of right- and left-going electrons, and the filling factors are the same for the two momentum directions, $f_{L(R)}\left(k_x\right) = f_{L(R)}\left(-k_x\right)$. Since their velocities are opposite, the contribution of the closed channels to the net current vanishes. Thus, we concentrate on open channels. For open channels, the filling factors for the two momentum directions are not the same. To realize this fact, we have to understand how the electrons get to the waveguide. This leads us to the concept of a reservoir. Any nanostructure taking part in quantum transport is part of an electric circuit. This means that it is connected to large, macroscopic electric pads each kept at a certain voltage (electrochemical potential). These pads contain a large number of electrons at thermal equilibrium. These electrons are characterized by the filling factor, which depends only on the energy and the chemical potential of the corresponding reservoir. In our setup, the waveguide is connected to two such reservoirs: left $(x \to -\infty)$ and right $(x \to \infty)$. Electrons with $k_x > 0$ come from the left reservoir and have the filling factor $f_L\left(E\right) \equiv f_F\left(E - \mu_L\right)$ and $f_R\left(E\right) \equiv f_F\left(E - \mu_R\right)$. Electrons with $k_x < 0$ come to the cross-section, having passed the constriction. Therefore, they carry the filling factor of the right reservoir, $f_R\left(E\right) \equiv f_F\left(E - \mu_R\right)$. Since the filling factors depend only on the energy, it is natural to replace k_x in favor of the total energy E for each momentum direction. Since the velocity is $v_x = \frac{1}{\hbar}\frac{\partial E}{\partial k_x}$, we have $dE = \hbar v\left(k_x\right) dk_x$, and this cancels the velocity in Eq. (2.33). Thus, we end up with the remarkably simple expression,

$$\begin{aligned} I &= \frac{2e}{\hbar}\frac{1}{2\pi}\int_{\mu_L}^{\mu_R} dE\left[f_L\left(E\right) - f_R\left(E\right)\right] \\ &= \frac{2e}{\hbar}\frac{1}{2\pi}\left(\mu_L - \mu_R\right) \\ &= \frac{2e^2}{h}V \\ &= G_0 V, \end{aligned} \tag{2.34}$$

where we assumed zero temperature. The proportionality coefficient is called the conductance quantum and conventionally defined as $G_0 = \frac{2e^2}{h}$. This is because conductance of the system, I/V, appears to be quantized in units of G_0 . This factor is made up from fundamental constants, does not depend on material properties, nanostructure size, and geometry, or from a concrete theoretical model used to evaluate the transport properties

2.5.1 Landauer-Buttiker formalism of transport

The equation. (2.34) is a specific case of the celebrated Landauer formula [106]. We have derived the formula for the case when the transmission $T(E)$, is either zero or one. The general case is treated in this section, where we introduce scattering to the transport problem. Modern fabrication technology allows for sophisticated semiconductor heterostructures, combining and shaping different metals, using nanotubes, molecules, and even single atoms as elements of electron transport circuits. Various means can be used to control the transport properties of a fabricated nanostructure. There is a common feature of all fabrication methods: two nanostructures that are intended to be identical, that is, are made with the same design and technology, are never identical. Besides the artificial features brought by design, there is also a disorder originating from defects of a different kind inevitably present in the structure. The position of and/or potential created by such defects is random, and in most cases, can be neither controlled nor measured.

The defects scatter electrons, affecting the transport properties. The conductance of the structure is thus random, depending on a specific realization of disorder in the structure and in the leads; this means there is a formidable number of uncontrollable parameters. Fortunately, the transport properties of any nanostructure can be expressed through a smaller set of parameters. The condition for this is that electrons traverse the structure without energy loss, so they experience only elastic scattering. These conditions for a given structure are always achieved at sufficiently low temperature and applied voltage. The scattering is characterized by a scattering matrix that contains information about electron wave functions far from the structure. There are many papers and textbooks covering and explaining the details of Landauer formalism [106, 107]. Here we follow a very simple idea in order to get the formalism without complications.

We now turn to the calculation of the current, using Eq. (2.33) as the starting point. Let us calculate the current through a cross-section located in the left waveguide (lead). The electrons with $k_x > 0$ originate from the left reservoir, and their filling factor is therefore $f_L(E)$. Now, the electrons with $k_x < 0$ in a given channel n are coming from the scattering region. A fraction of these electrons originate from the left reservoir and are reflected; they carry the filling factor $f_L(E)$. This fraction is determined by the probability of being reflected to channel n from all possible

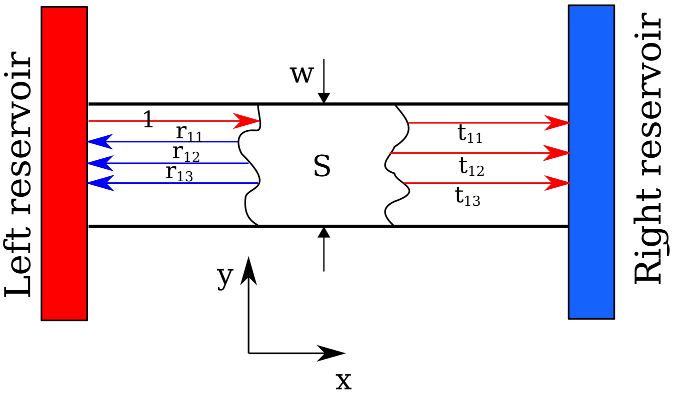

Figure 2.10: Schematic of ballistic transport in a two-terminal multi-channel. Structure of two-terminal scattering matrix. We show reflection and transmission amplitudes of the electron wave coming from the left in the second transport channel, $n' = 1$.

starting channels n,

$$R_n\left(E\right) = \sum_{n'} r_{nn'}\,. \tag{2.35}$$

Other electrons are transmitted through the scattering region, their filling factor being $f_R\left(E\right)$. The resulting filling factor for $k_x < 0$ is therefore

$$R_n\left(E\right) f_L\left(E\right) - \left(1 - R_n\left(E\right)\right) f_R\left(E\right)\,. \tag{2.36}$$

For the current flowing from left to right we write

$$I^{+} = 2\sum_{n}\int_{0}^{\infty}\frac{dk_x}{2\pi} ev\left(k_x\right) f_L\left(E\right), \tag{2.37}$$

while for the current moving from right to left we have

$$I^{-}=2\sum_{n}\int_{-\infty}^{0}\frac{dk_x}{2\pi}ev\left(k_x\right)\left[R_n\left(E\right)f_L\left(E\right)+\left(1-R_n\left(E\right)\right)f_R\left(E\right)\right]. \tag{2.38}$$

The net current is the sum of these two currents

$$\begin{aligned}I&=I^{+}+I^{-}\\&=2\sum_{n}\int_{0}^{\infty}\frac{dk_x}{2\pi}ev\left(k_x\right)\left(1-R_n\left(E\right)\right)\left[f_L\left(E\right)-f_R\left(E\right)\right] \qquad (2.39)\\&=2\sum_{n}\int_{0}^{\infty}\frac{dk_x}{2\pi}ev\left(k_x\right)T_n\left(E\right)\left[f_L\left(E\right)-f_R\left(E\right)\right], \qquad (2.40)\end{aligned}$$

where

$$T_n\left(E\right)=1-R_n\left(E\right).$$

To derive the final equation line, we have changed k_x to $-k_x$ in the second integral in Eq. (2.38). Now we repeat the trick of the previous section, changing variables from k_x to E, and we arrive at the following expression:

$$I=\frac{2e}{h}\int dE\sum_{n}T_n\left(E\right)\left[f\left(E-\mu_L\right)-f\left(E-\mu_R\right)\right]. \tag{2.41}$$

Assuming $\mu\equiv\mu_L=\mu_R+\delta\mu$, with $\delta\mu\ll\mu$, we can linearize the Landauer formula [108] to obtain the conductance $G\equiv e\delta I/\delta\mu$, which can be written as

$$G\left(\mu\right)=-G_0\int d\epsilon\sum_{n}T_n\left(E\right)\frac{\partial f\left(\epsilon-\mu\right)}{\partial\epsilon}, \tag{2.42}$$

where $G_0=\frac{2e^2}{h}$ is the conductance quantum. For a system at zero temperature, Eq. (2.42) can be simplified to $G=G_0T\left(\mu\right)$.

Calculation of the current in the right waveguide gives the same result: current is conserved.

A.1 Proof of tight binding model in second quantization

In this section, using second quantization formalism, we want to introduce tight-binding Hamiltonian.

As we know from Bloch's theorem, eigenstates of a periodic Hamiltonian can be presented in the form of Bloch waves

$$\psi_k\left(r\right) = e^{ik.r} u_k\left(r\right) \ ,$$

where the components of the crystal momentum k take values inside the Brillouin zone, $k \in [-\frac{\pi}{a}, \frac{\pi}{a}]$, and we have assumed that the periodicity of the lattice potential is the same in all directions, i.e. $V(r + ae_i) = V(r)$

$$\left(\frac{p^2}{2m} + V\left(r\right)\right)\psi_k\left(r\right) = E_k\psi_k\left(r\right) \ .$$

In the second quantization formalism one can write the Hamiltonian above as follows

$$\hat{H} = \int d^d r a^\dagger\left(r\right)\left(\frac{-\nabla^2}{2m} + V\left(r\right)\right)a\left(r\right) \ . \tag{2.43}$$

Let us define Wannier states as

$$|\psi_R\rangle = \frac{1}{\sqrt{N}}\sum_k e^{-ik\cdot R}|\psi_k\rangle \quad , \quad |\psi_k\rangle = \frac{1}{\sqrt{N}}\sum_R e^{ik\cdot R}|\psi_R\rangle \, . \tag{2.44}$$

The first thing to notice is that the Wannier states $\{|\psi_R\rangle\}$ form an orthonormal basis of the singleparticle Hilbert space, i.e. the transformation between the real space and the Wannier representation is unitary,

$$|r\rangle = \sum_R |\psi_R\rangle\langle\psi_R|r\rangle = \sum_R \psi_R^*\left(r\right)|\psi_R\rangle \, ,$$

or

$$a^\dagger\left(r\right) = \sum_R \psi_R^*\left(r\right) a_R^\dagger \, . \tag{2.45}$$

Similarly, the unitary transformation between Bloch and Wannier states Eq. 2.44 induces an operator transformation

$$a_R^\dagger = \frac{1}{\sqrt{N}} \sum_k e^{-ik\cdot R} a_k^\dagger, \tag{2.46}$$

$$a_k = \frac{1}{\sqrt{N}} \sum_R e^{ik\cdot R} a_R \,. \tag{2.47}$$

We can now use the transformation formulae Eq. (2.45) and Eq. (2.46) to formulate a Wannier representation of the Hamiltonian Eq. (2.43). Using the fact that the Bloch states diagonalize the single-particle Hamiltonian, we obtain

$$\begin{aligned}
\hat{H} &= \int d^d r a^\dagger(r) \left(\frac{-\nabla^2}{2m} + V(r)\right) a(r) \\
&= \int d^d r \left(\sum_R \psi_R^*(r)\, a_R^\dagger\right) \left(\frac{-\nabla^2}{2m} + V(r)\right) \left(\sum_{R'} \psi_R(r)\, a_{R'}\right) \\
&= \sum_{R,R'} a_R^\dagger a_{R'} \int d^d r \psi_R^*(r) \left(\frac{-\nabla^2}{2m} + V(r)\right) \psi_{R'}(r) \\
&= \sum_{R,R'} a_R^\dagger a_{R'} \int d^d r \frac{1}{\sqrt{N}} \sum_k e^{-ik\cdot R} \psi_k^*(r) \left(\frac{-\nabla^2}{2m} + V(r)\right) \frac{1}{\sqrt{N}} \sum_{k'} e^{-ik'\cdot R'} \psi_{k'}(r) \\
&= \sum_{R,R'} a_R^\dagger a_{R'} \frac{1}{N} \sum_{k,k'} e^{-ik\cdot R} e^{-ik'\cdot R'} \int d^d r \psi_k^*(r) \left(\frac{-\nabla^2}{2m} + V(r)\right) \psi_{k'}(r) \\
&= \sum_{R,R'} a_R^\dagger a_{R'} \frac{1}{N} \sum_{k,k'} e^{-ik\cdot R} e^{-ik'\cdot R'} \int d^d r \psi_k^*(r)\, E_{k'} \psi_{k'}(r) \\
&= \sum_{R,R'} a_R^\dagger a_{R'} \frac{1}{N} \sum_{k,k'} E_{k'} e^{-ik\cdot R} e^{-ik'\cdot R'} \int d^d r \psi_k^*(r)\, \psi_{k'}(r) \\
&= \sum_{R,R'} a_R^\dagger a_{R'} \frac{1}{N} \sum_{k,k'} E_{k'} e^{-ik\cdot R} e^{-ik'\cdot R'} \delta_{k,k'} \\
&= \sum_{R,R'} a_R^\dagger a_{R'} \frac{1}{N} \sum_k E_k e^{-ik\cdot(R-R')} \\
&= \sum_{R,R'} a_R^\dagger a_{R'} t_{RR'} \,.
\end{aligned}$$

A.2 Polynomial expansion of a function

In general, the expansion of a given function $f\left(x\right)$ in terms of a polynomial set $p_n\left(x\right)$ can be introduced as:

$$f\left(x\right)=\sum_n \alpha_n p_n\left(x\right)\ , \tag{2.48}$$

where the expansion coefficients α_n are proportional to the scalar product of f and p_n,

$$\alpha_n=\frac{\langle f|p_n\rangle}{\langle p_n|p_n\rangle}\,. \tag{2.49}$$

The polynomial set $p_n\left(x\right)$ must fulfill the orthogonality relations

$$\langle p_n|p_m\rangle=\frac{\delta_{nm}}{\langle p_n|p_n\rangle}\,. \tag{2.50}$$

The scalar product $\langle f|g\rangle$ between functions $f(x)$and $g(x)$ is defined on the interval $[a,b]$ with a positive weight $w(x)$,

$$\langle f|g\rangle=\int_a^b w\left(x\right)f\left(x\right)g\left(x\right)dx\,. \tag{2.51}$$

An expansion can be used to approximately reconstruct the desired function. It shifts the problem from the direct solution of $f(x)$ to the computation of expansion moments α_n . Given a good choice of the polynomial set $p_n\left(x\right)$, the moment computation can be implemented in a very efficient way

3 Quantum transport in hybrid monolayer-bilayer-monolayer structures

3.1 Outline of the chapter

In this chapter we explore the nature of electronic transmission in a compound system of monolayer-bilayer-monolayer (MBM) in one and two dimensions. As we pointed out in Sec. 2.2 the process of obtaining graphene by exfoliation technique leads to flakes of stacked single layers together with monolayers, hence such an MBM structures can occur naturally in experiments. Understanding transport in such systems is not only interesting but also potentially useful for electronic device applications. Motivated by graphene based MBM structures, we develop a framework to solve for transmission and reflection coefficients in such hybrid strips, and calculate the strip conductance in several setups. We focus on two distinct systems. One is an MBM structure in 1D which is basically a chain-ladder-chain system, see Fig. 3.2, and the other is a graphene based MBM system for which we compute the transport and discuss the results in detail.

First, we outline some generic features and assumptions regarding our MBM structure:

1. Monolayers are semi infinite lattices for which Bloch theorem applies, i.e. the wave amplitude $\psi(\mathbf{r})$ from one site to another site on the lattice, is different only by a phase, meaning $\psi(\mathbf{r}+\mathbf{R}) = e^{i\mathbf{k}\cdot\mathbf{R}}\psi(\mathbf{r})$ where $\mathbf{R}$ is a lattice vector.
2. Monolayers are metallic and act as carrier reservoirs or contacts which we refer to as leads.
3. Bilayer region is essentially made by stacking two monolayer flakes. Hence, leads and bilayer region are made from the same material.

We will see in the following sections that the assumptions above in general result in some simplification in the calculation while they preserve the generality of the study. The first two assumptions also require that the monolayer leads are connected to batteries far away from the bilayer region. This is the case in most electronic devices since the wire bondings are usually longer than the device itself, so one can employ Bloch theorem in the leads.

This chapter is based on both unpublished work and on the following publication by the candidate:

- *Transmission across a bilayer graphene region,* Hadi Z. Olyaei, Pedro Ribeiro, and Eduardo V. Castro Phys. Rev. B 99, 205436 – Published 29 May 2019

This chapter is organized as follows: In Sec. 3.2, we study the transport in a hybrid chain-ladder-chain structure both using wave matching method and using the transfer matrix method. In Sec. 3.3.1, we introduce the model of the physical setup and the corresponding tight-binding formulation as well as the method for obtaining the transmission across the bilayer region using the transfer matrix formulation. In Sec. 3.3.2-5, some representative results of transmission are presented, including the new types of micro-structured gated bilayer graphene. Sec. 3.3.6 contains a short summary and the conclusions. In Sec. 3.4, we present some of the details of the calculation of the transmission.

3.2 MBM in 1D: Transport in chain-ladder-chain hybrid structure

In this section, we investigate the quantum transport in a 1D hybrid structure of chain-ladder-chain (CLC) as it is shown in Fig. 3.2. We use its simplicity to establish the theory and methodology we later employ to explore the more complex case of graphene based MBM. In fact, the analysis of this toy-model helps us to understand the essence of quantum transport in confined 1D and 2D systems. We will show that the 2D graphene based MBM structure can actually be reduced to a proper 1D problem. Hence, it is worth exploring the conductance properties of our CLC model in detail.

As we discussed in Sec. 2.5, in mesoscopic systems where the coherent phase length is much longer than the linear system size we can use the celebrated Landauer-Buttiker formula in order to characterize the conductance of the system [107]. At zero temperature, the conductance is given in units of quantum conductance $\frac{2e^2}{h}$ as

$$G\left(\mu\right)=\frac{2e^2}{h}T\left(\mu\right)\ ,$$

where the factor $T\left(\mu\right)$ is the transmission probability integrated over all available channels in the leads and μ is the chemical potential. Hence, the conductance problem at zero temperature is equivalent to the transmission problem.

3.2.1 CLC model

Our system consists of two similar semi-infinite chains of atoms, with parameter a, connected to a finite size ladder forming a hybrid structure. We use the nearest-neighbor tight-binding Hamiltonian [109], to model the single electron in the chain as,

$$H_{chain} = -t\sum_{m} a^{\dagger}(m)\, a(m-1) + h.c \tag{3.1}$$

and for the ladder with interlayer hopping of $t_{\perp}$

$$H_{ladder} = t_{\perp}\sum_{m} a_1^{\dagger}(m)\, a_2(m) - t\sum_{j=1}^{2}\sum_{m} a_j^{\dagger}(m)\, a_j(m-1) + h.c\,, \tag{3.2}$$

where $a^{\dagger}(a)$ creates(annihilates) an electron in position $R_m = ma$ and t is the hopping energy of the electron from one atom to its nearest neighbors atoms. We obtain the energy spectrum of the electron in the chain by diagonlizing the Hamiltonian above. The following Fourier transform

$$a^{\dagger}(k) = \frac{1}{\sqrt{N}}\sum_{m} e^{ika} a^{\dagger}(m)\,,$$

diagonalizes the Hamiltonian, H, with N being the number of atoms in the chain. In $\left\{a^{\dagger}(k)\right\}$ basis, the Hamiltonian is written as,

$$H = \sum_{k} a^{\dagger}(k)\left[-2t\cos(ka)\right] a(k)\ , \tag{3.3}$$

which yields the spectrum of the chain,

$$\varepsilon = -2t\cos(ka)\ . \tag{3.4}$$

3.2.2 Transfer matrix method

A general method for solving the scattering problem is to use the wave matching method at the boundaries. This requires the wavefunction inside the central region. In order to avoid determining the wave amplitudes in the scattering region we make use of transfer matrix method [110].

For the chain, the solution for the time independent Schrodinger equation $H|\psi\rangle = \varepsilon|\psi\rangle$ determines the eigenstate, $|\psi\rangle$, and eigenenergy, ε, of the electron. We introduce the onsite amplitude as $\psi(m) = \langle m|\psi\rangle$ and rewrite the Schrodinger equation in its discrete form as,

$$\epsilon\psi(m) = -t\psi(m+1) - t\psi(m-1) \tag{3.5}$$

We rewrite Eq. (3.5) in a more convenient form as

$$\psi(m+1) = -\frac{\epsilon}{t}\psi(m) - \psi(m-1)\ . \tag{3.6}$$

The first equality relates the amplitude of the wave on site $m+1$ with its amplitude on two preceding sites. In other words, given amplitudes on two consecutive sites, the amplitude on the next site can be obtained. The equations Eq. (3.6) can be written in a matrix equation form,

$$\Psi(m+1) = \mathbb{T}(\varepsilon)\Psi(m)\ , \tag{3.7}$$

where the energy dependent transfer matrix $\mathbb{T}(\varepsilon)$ (Transfer matrix) and the vector wavefunction $\Psi(m)$ read,

$$\mathbb{T}(\varepsilon) = \begin{bmatrix} -\frac{\epsilon}{t} & -1 \\ 1 & 0 \end{bmatrix}, \qquad \Psi(m) = \begin{bmatrix} \psi(m) \\ \psi(m-1) \end{bmatrix}.$$

It is important to note that the 2×2 matrix $\mathbb{T}$ is always invertible as $\det(\mathbb{T}) = 1$. Having unit determinant denotes that its eigenvalues λ_1 and λ_2 are nonzero and,

$$\lambda_1\lambda_2 = 1.$$

The recursive method formulated with Eq. (3.7) can be employed to any finite size chain. It is also applicable to the semi-infinite chain of our setup, Fig. 3.2. Recalling that the Bloch theorem in the semi-infinite chain

$$\Psi(m+1) = e^{ika}\Psi(m)\ , \tag{3.8}$$

we can rewrite Eq. (3.7) in the from of [111, 112],

$$\mathbb{T}(\varepsilon)\Psi(m) = e^{ika}\Psi(m)\ . \tag{3.9}$$

The equation above is nothing but the eigenvalue problem of the transfer matrix. by solving the equation

$$\mathbb{T}(\varepsilon)\zeta = \lambda\zeta\,, \tag{3.10}$$

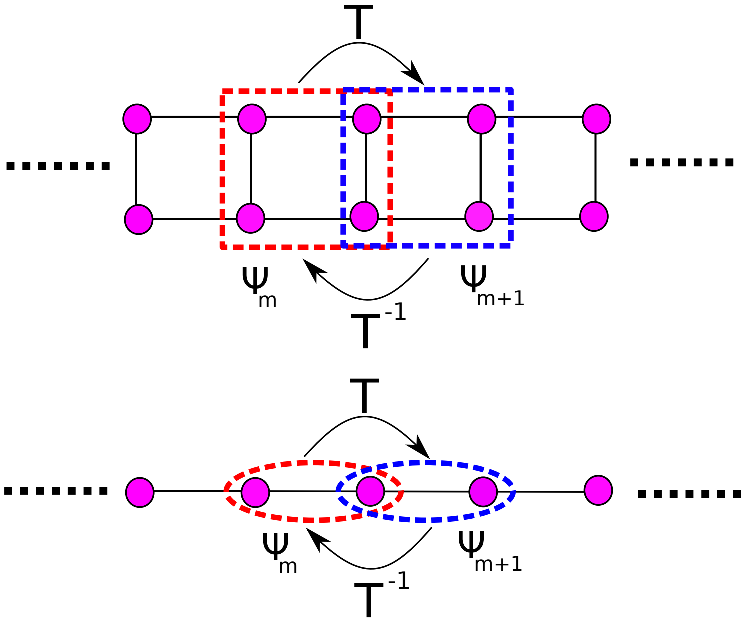

Figure 3.1: Transfer matrix operation for a double chain (top) and chain (bottom). The $\mathbb{T}$ matrix relates the amplitude within the blue ellipse (square) to the amplitudes in red ellipse (square). The inverse operation is also valid as $\mathbb{T}^{-1}$ exist for every values of ε. Note that the number of atoms within the dashed square dictates the dimension of the transfer matrix.

we obtain

$$\lambda_{\pm} = -\frac{\varepsilon}{2t} \pm \sqrt{\left(\frac{\varepsilon}{2t}\right)^2 - 1}, \qquad \zeta^{\pm} = \frac{1}{\sqrt{2}} \begin{pmatrix} 1 \\ \frac{-1}{\frac{\varepsilon}{2t}+\lambda_{\pm}} \end{pmatrix}. \tag{3.11}$$

If we plug the spectrum for the chain given by Eq. (3.4) into the equation above we confirm that

$$\lambda_{+} = \lambda_{-}^{-1} = e^{ika}\,. \tag{3.12}$$

As it is shown in Fig. 3.1 the act of transfer matrix by construction transfers the wave amplitude from left to right. Hence, we interpret ζ^{+} (ζ^{-}) as the mode moving from left to right (right to left) according to the sign in the exponential of the corresponding eigenvalue. So, for the semi-infinite chain the wave amplitudes on lattice points can be written as a superposition of the two left and right moving modes as [113],

$$\Psi\left(m\right)=A^{+}\lambda_{+}^{m}\zeta^{+}+A^{-}\lambda_{-}^{m}\zeta^{-}\;. \tag{3.13}$$

One more useful relation is obtained if we define $U=\left[\zeta^{+},\zeta^{-}\right]$,

$$\Psi\left(m\right)=U\left[\begin{array}{c} A^{+}\lambda_{+}^{m}\\ A^{-}\lambda_{-}^{m} \end{array}\right]. \tag{3.14}$$

Now, we take similar steps for the central region of our MBM setup. The discrete Schrodinger equation for the central region can be written as,

$$\epsilon\psi_{1}\left(m\right)=-t\psi_{1}\left(m+1\right)-t\psi_{1}\left(m-1\right)+t_{\perp}\psi_{2}\left(m\right) \tag{3.15}$$
$$\epsilon\psi_{2}\left(m\right)=-t\psi_{2}\left(m+1\right)-t\psi_{2}\left(m-1\right)+t_{\perp}\psi_{1}\left(m\right)\;, \tag{3.16}$$

where $\psi_{j}\left(m\right)=\langle j,m|\psi\rangle$, with $|j,m\rangle$ for the local-state on site m of the chain $j=1,2$. We end up again with two recursive coupled equations for the central region. In general the central region has a finite size. In general the central region and plays the role of a scatterer which may have a complex structure. In fact the transfer matrix formalism help us to avoid explicit solving of the Schrodinger equation in the central region. The equations in Eq. (3.15) and Eq. (3.16) in its transfer matrix form can be written as,

$$\Psi_{B}\left(m+1\right)=\mathbb{T}_{B}\left(\varepsilon\right)\Psi_{B}\left(m\right)\;, \tag{3.17}$$

where the four by four transfer matrix, $\mathbb{T}_{B}\left(\varepsilon\right)$, and the amplitude vector, $\Psi_{B}\left(m\right)$, are represented as,

$$\mathbb{T}_{B}\left(\varepsilon\right)=\left[\begin{array}{cccc} -\frac{\epsilon}{t} & -\frac{t_{\perp}}{t} & -1 & 0\\ -\frac{t_{\perp}}{t} & -\frac{\epsilon}{t} & 0 & -1\\ 1 & 0 & 0 & 0\\ 0 & 1 & 0 & 0 \end{array}\right],\quad \Psi_{B}\left(m\right)=\left[\begin{array}{c} \psi_{1}\left(m\right)\\ \psi_{2}\left(m\right)\\ \psi_{1}\left(m-1\right)\\ \psi_{2}\left(m-1\right) \end{array}\right]. \tag{3.18}$$

3.2.3 Chain ladder interface and transmission coefficient

With the electron wavefunction in both leads and in the central region at hand, we are in position to express the transmission and reflection of an electron in the left

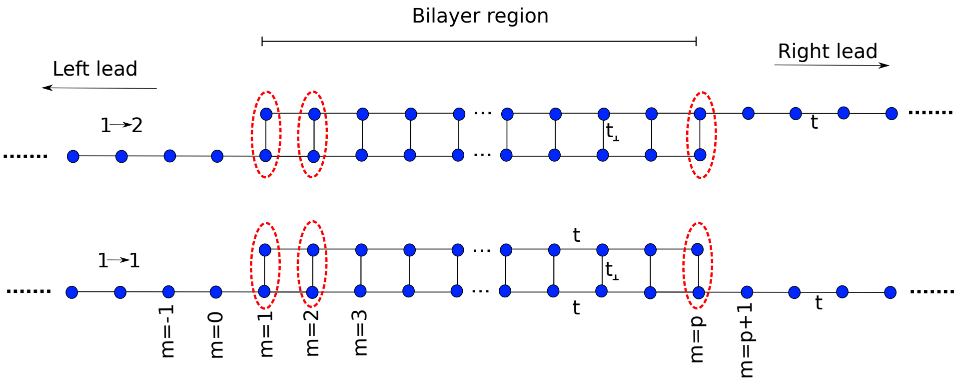

Figure 3.2: Hybrid chain-ladder-chain structure. Top: Shows $1 \rightarrow 2$ configuration where two semi infinite leads are connected to the ladder in the central region in opposite layers. Bottom: Exhibits $1 \rightarrow 1$ setup where the leads are connected to same layer. The index m labels the position of the atoms. The interalyer hopping is shown by t where the interlyer hopping is $t_{\perp}$.

lead approaching the central region. We intuitively expect a scattering process as the central region can be considered as a barrier. As discussed in Sec. 2.5.1 determining the transmission and reflection probabilities is of utmost importance in the Landauer-Buttiker formula for conductance. For the current scattering problem the relation (3.14) can be rewritten in terms of transmission and reflection coefficients, respectively τ and r . In the left lead,

$$\Psi_L(m) = \begin{bmatrix} \psi_L(m) \\ \psi_L(m-1) \end{bmatrix} = U \begin{bmatrix} \lambda_+^m \\ \lambda_-^m r \end{bmatrix} , \tag{3.19}$$

where we set the amplitude, A^+, of the right moving mode, ζ^+, to be one and A^- is replaced by the reflection factor r. Similarly, we set, $A^+ = \tau$ and $A^- = 0$ for the right lead, so that,

$$\Psi_R(m) = \begin{bmatrix} \psi_R(m) \\ \psi_R(m-1) \end{bmatrix} = U \begin{bmatrix} \lambda_+^{m-p} \tau \\ 0 \end{bmatrix} . \tag{3.20}$$

For a given eigen-energy, ε, the transfer matrix of the central region transfers the wave amplitudes in position $m = 1$ to the amplitude in $m = p + 1$ as follows,

$$\Psi_B(p+1) = \mathbb{M}(\varepsilon)\,\Psi_B(1) , \tag{3.21}$$

where

$$\mathbb{M}\left(\varepsilon\right) = \left(\mathbb{T}_B\left(\varepsilon\right)\right)^p ,$$

is the p-step transfer matrix. It actually relates the amplitudes at the two interfaces, $m = 1$ and $m = p$, as

$$\begin{bmatrix} \psi_1\left(p\right) \\ \psi_2\left(p\right) \\ \psi_1\left(p+1\right) \\ \psi_2\left(p+1\right) \end{bmatrix} = \mathbb{M}\left(\varepsilon\right) \begin{bmatrix} \psi_1\left(1\right) \\ \psi_2\left(1\right) \\ \psi_1\left(0\right) \\ \psi_2\left(0\right) \end{bmatrix} . \tag{3.22}$$

In general, two different configurations exist for the MBM hybrid structure. The first case is when the two chains are connected to the same layer in the central region and the second case happens when the leads are connected to opposite layers, see Fig. 3.2. We name the first setup 1 → 1 (one to one) and call the second one as 1 → 2 (one to two) configuration. For the 1 → 1 setup as it is seen in Fig. 3.2, $\psi_2\left(0\right) = \psi_2\left(p+1\right) = 0$. These amplitudes are zero due to missing atoms. With these conditions at the two interfaces, the equation (3.22) reads,

$$\begin{bmatrix} \psi_1\left(p+1\right) \\ 0 \\ \psi_1\left(p\right) \\ \psi_2\left(p\right) \end{bmatrix} = \mathbb{M}\left(\varepsilon\right) \begin{bmatrix} \psi_1\left(1\right) \\ \psi_2\left(1\right) \\ \psi_1\left(0\right) \\ 0 \end{bmatrix} . \tag{3.23}$$

The matrix equation above has six unknowns and four equations. So, we restate it in terms of the two amplitudes in the left lead as,

$$\begin{bmatrix} \psi_1\left(p+1\right) \\ \psi_1\left(p\right) \end{bmatrix} = \mathcal{M}_{1\to 1} \begin{bmatrix} \psi_1\left(1\right) \\ \psi_1\left(0\right) \end{bmatrix} . \tag{3.24}$$

Where $\mathcal{M}_{1\to 1}$ relates the amplitudes of two leads of the system. One last step is to replace the amplitudes in terms of transmission and reflection coefficients as follows,

$$\begin{bmatrix} 1 \\ r \end{bmatrix} = U^{-1}\mathcal{M}_{1\to 1}U \begin{bmatrix} \tau \\ 0 \end{bmatrix} , \tag{3.25}$$

with,

$$\mathcal{M}_{1\to 1} = \frac{1}{\mathbb{M}_{22}} \begin{bmatrix} (\mathbb{M}_{22}\mathbb{M}_{21} - \mathbb{M}_{21}\mathbb{M}_{11}) & (\mathbb{M}_{23}\mathbb{M}_{22} - \mathbb{M}_{23}\mathbb{M}_{13}) \\ (\mathbb{M}_{41}\mathbb{M}_{22} - \mathbb{M}_{42}\mathbb{M}_{21}) & (\mathbb{M}_{43}\mathbb{M}_{22} - \mathbb{M}_{42}\mathbb{M}_{23}) \end{bmatrix}. \tag{3.26}$$

For the $1 \to 2$ setup, using $\psi_2(0) = \psi_1(p+1) = 0$, we can repeat similar steps to get,

$$\mathcal{M}_{1\to 2} = \frac{1}{\mathbb{M}_{12}} \begin{bmatrix} (\mathbb{M}_{12}\mathbb{M}_{21} - \mathbb{M}_{22}\mathbb{M}_{11}) & (\mathbb{M}_{23}\mathbb{M}_{12} - \mathbb{M}_{22}\mathbb{M}_{13}) \\ (\mathbb{M}_{41}\mathbb{M}_{12} - \mathbb{M}_{42}\mathbb{M}_{11}) & (\mathbb{M}_{43}\mathbb{M}_{12} - \mathbb{M}_{42}\mathbb{M}_{13}) \end{bmatrix}. \tag{3.27}$$

We use the Landauer-Buttiker formula, see Sec. 2.5.1, to obtain the zero temperature conductance of the hybrid structure from its transmission coefficient, τ.

$$G(\varepsilon) = G_0 |\tau(\varepsilon)|^2 ,$$

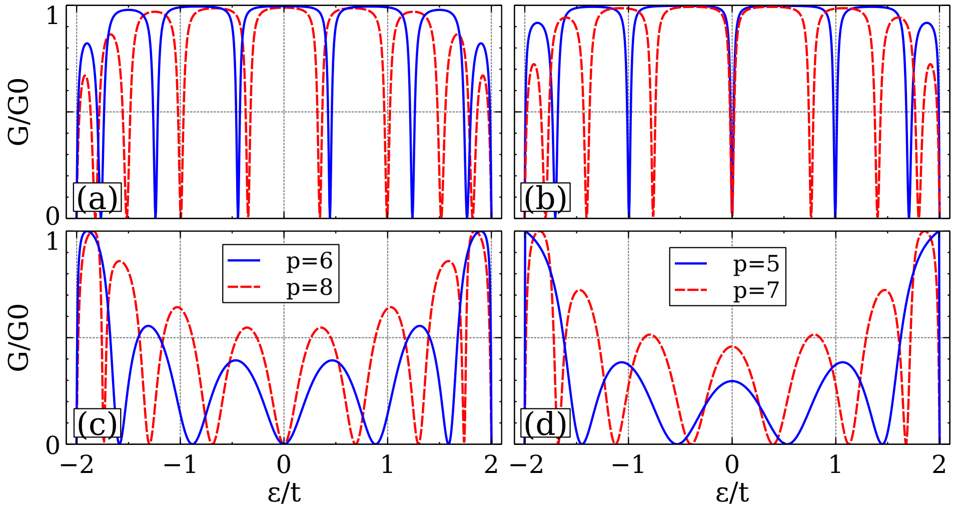

Figure 3.3: Chain-ladder-chain conductance is shown for $1 \to 1$ setup (a-b) and $1 \to 2$ setup (c-d) for several central region lengths. Note that the number of maxima in the conductance is related with the ladder length, p. A ladder with length p exhibits $p+1$ maxima in its conductance.

where $G_0 = \frac{2e^2}{h}$. We show some representatives of the conductance in Fig. 3.3 for both $1 \to 1$, the panel (a) and (b) and $1 \to 2$, the panel (c) and (d), configurations. We also checked these results against Kwant. The interlayer hopping is set to be

$t_\perp = 0.1t$. This is on purpose as in the van der Waals structures the interlayer hopping is smaller than the intraleyer hopping t. An immediate consequence of such choice, $t_\perp < t$, is that the transport in the vertical direction, in general, is smaller. This explains the lower conductance of $1 \rightarrow 2$ configuration compared to $1 \rightarrow 1$ setup. Both setups exhibit resonant transmission as a result of interference of partial waves scattering from the chain/ladder interfaces and mismatch in wavefunctions of leads and the ladder [114, 115, 116].

3.3 MBM in 2D: Transmission across a bilayer graphene region

Now we turn our attention to the problem of conductance in two dimensional MBM structure. Our case of study is graphene honeycomb based MBM. For such system the transmission across a graphene bilayer region is calculated for two different types of connections to monolayer leads. A transfer matrix algorithm based on a tight binding model is developed to obtain the ballistic transmission beyond linear response. We show that the two configurations behave similarly when no gate voltage is applied. For a finite gate voltage, both develop a conductance gap characteristic of a biased bilayer, but only one to one case shows a pronounced conductance step at the gap edge. A gate voltage domain wall applied to the bilayer region renders the conductance of the two configurations similar. For a microstructure consisting of equally spaced domain walls, we find a high sensitivity to the domain size. This is attributed to the presence of topologically protected in-gap states localized at domain walls, which hybridize as the domain size becomes of the order of their confining scale. Our results show that transmission through a bilayer region can be manipulated by a gate voltage in ways not previously anticipated.

The unique band structure of graphene gives rise to several alluring phenomena which have been the subject of intense research since its experimental discovery in 2004 [8, 53, 117, 54]. In particular, its high charge-carrier mobility has rendered graphene a highly attractive and promising component for electronic and optoelectronic devices [118, 119]. Another appealing feature of graphene for device application is its stability at the nanometer scale, ensured by the covalent bonds among the carbon atoms [120], which is highly desirable for device-miniaturization. A graphene-based electronic device, entirely made out of micro-structured graphene sheets, is thus expected to reduce significantly energy dissipation and optimize device-miniaturization and functionality [121, 122, 123]. The recent realization of a short channel field-effect transistor, using just 9- and 13-atom wide graphene nanoribbons [124], is a convincing step in that direction. This is to be contrasted with mainstream semiconductor technology which usually integrates different materials and where component-interfacing can be difficult to scale-down [125].

Although a gapless conductor, the versatility of the electronic properties of graphene make it possible to easily induce a gap. This can be done by several means: cutting it into nanoribbons with zigzag or armchair edges [126, 127, 128, 113]; by breaking inversion symmetry with an appropriate substrate [129]; or applying an out-of-plain electric filed in graphene bilayer structures [65, 130, 76, 21].

Compared to monolayer graphene, the possibility of tuning the induced gap by an external, perpendicular electrical field, which is easily introduced through a gate potential, makes the bilayer more suitable for device applications [131]. Not only the gap can be tuned by a gate bias, but also a twist angle can be engineered between the two layers [132, 94]. This leads to a strong reconstruction of the band structure at low energies [133]. The recent observation of superconductivity and insulating behavior in twisted bilayer graphene at the magic angles clearly shows the high degree of tunability of this system [134, 135]. Further manipulation of the bilayer response is possible by inserting an insulator between the two graphene layers, out of which tunnel field effect transistors have been realized [136, 122, 137, 138, 139, 140].

Another advantage of the graphene bilayer is that its electronic structure can be manipulated by a layer-selective potential, induced by a gate voltage. The possibility of sharply reversing the sign of voltage, thus creating a well-defined one-dimensional boundary separating regions of constant potential, has been demonstrated recently [50]. These domain walls support confined one-dimensional states that are topologically protected and can be used as purely one-dimensional channels [141, 142].

The ballistic transport across a bilayer graphene region has been studied at length [42, 43, 143, 44, 45, 144, 46, 47, 48, 49]. Particular attention has been given to a setup where a gate voltage is applied within the bilayer region [43, 143, 145, 144, 146, 49]. These studies already revealed a high degree of tunability of the transport properties. However, the effects of further manipulations of the gate voltage, namely through the creation of a domain wall affecting the bilayer region [50] are yet to be investigated. Furthermore, the possibility of a microstructured gate voltage with several built-in domain walls opens up new avenues to engineer electronic transport at the nanoscale.

The aim of this section is to study ballistic transport of micro-structured bilayer graphene flakes with different types of connection to monolayer. Using a tight-binding model of an AB staked bilayer flake, taken to be infinite in the transverse direction, we observe that the conductance displays aperiodic oscillations as a function of chemical potential. The conductance in the presence of a single voltage domain is shown to be compatible with previous results obtained within a low energy approximation. We compute the conductance in the presence of a domain wall in the gate bias and show that, in this case, geometries with different types of connection to monolayer leads behave similarly. We further study the effect of a micro-structured gate bias with multiple domain walls. By changing the separation between domain-walls we explore the crossover form well separated domain-wall states to the fully hybridized regime where in-gap states start to contribute to the conductance. Finally, we have studied the viability of an integrated nano-transistor for experimentally reasonable conditions finding that this setup can achieve on/off ratios of the output current within $50 \lesssim I_{\text{on}}/I_{\text{off}} \lesssim 200$.

3.3.1 Model and methods

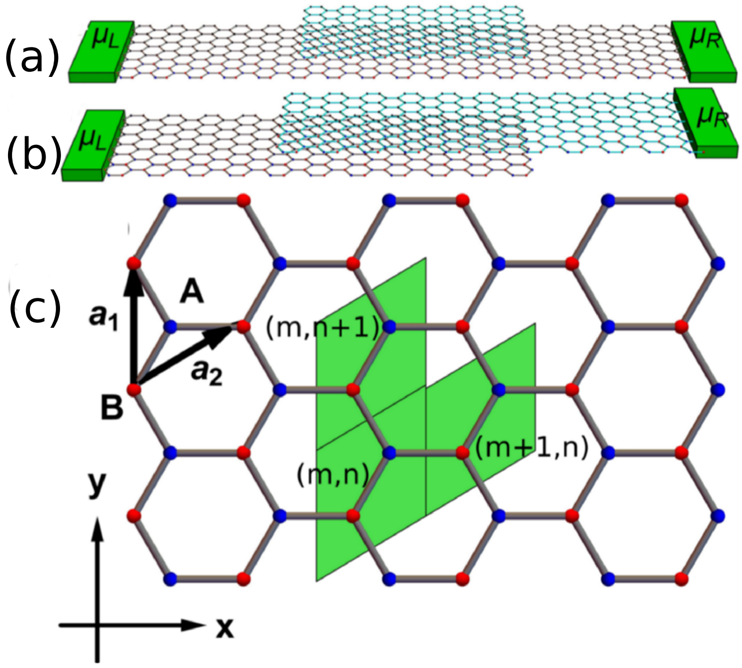

Figure 3.4: System setups with a bilayer region used in this work: (a) the 1 → 1 setup; (b) the 1 → 2 setup. (c) Primitive vectors $\boldsymbol{a}_1$ and $\boldsymbol{a}_2$, sublattice labels A (blue) and B (red), and unit cell labeling of the monolayer strucuture.

Schematics of the setup for which the transmission and the conductance are studied is shown in Fig. (3.4). The case of Fig. 3.4(a) consists of a single layer graphene with a flake of another layer on top, the 1 → 1 setup. The second configuration is obtained from two sheets of graphene that are partially overlapped, the 1 → 2 setup, as shown in Fig. 3.4(b). In both we consider A-B stacking. Translational invariance along the transverse direction (y-axis) is presumed. We are interested in the ballistic regime where the electronic mean free path is larger than the typical length of the device. For simplicity, we consider the case of perfect contacts, which can be replaced by infinite leads.

We model electrons in the structure using the conventional tight-binding approach for p_z-electrons [54] hopping between nearest neighbor carbon sites of the atomic lattice shown in Fig. (3.4)(c), which can be written as $H = H_1 + H_2 + H_\perp$. Here,

$$H_j = -t \sum_{m,n} a^\dagger_{j,m,n} \left[b_{j,m,n} + b_{j,m+1,n} + b_{j,m,n+1} \right] \tag{3.28}$$

$$+ \sum_{m,n \in \mathrm{BL}} V_j \left[a^\dagger_{j,m,n} a_{j,m,n} + b^\dagger_{j,m,n} b_{j,m,n} \right] + h.c \tag{3.29}$$

is the Hamiltonian of the $j = 1, 2$ layer, and

$$H_\perp = -t_\perp \sum_{m,n \in \mathrm{BL}} a^\dagger_{1,m,n} b_{2,m,n} + h.c\,. \tag{3.30}$$

is the inter-layer hopping term, with $a_j^\dagger \left(b_j^\dagger\right)$ the creation operators of a particle in sublattice $A\,(B)$ in the (m,n) unit cell of the jth layer. The effect of an applied gate voltage within the bilayer region is modeled by V_j. The BL restriction in the summation stands for sites belonging to the bilayer region.

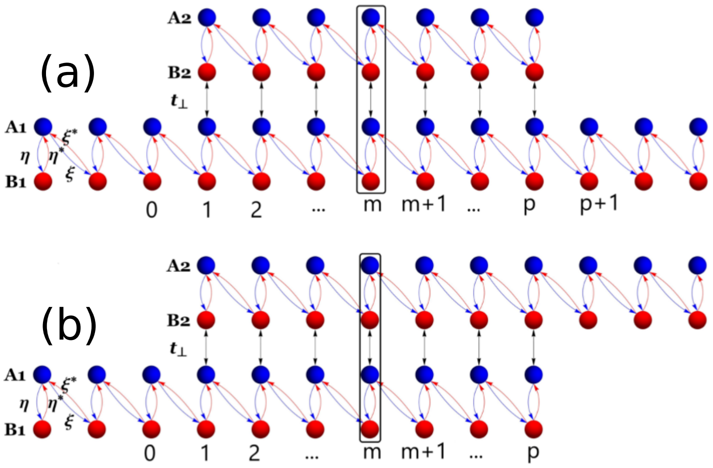

Figure 3.5: 1D effective chain obtained after Fourier transform, as described in the main text: (a) The $1 \to 1$ configuration; (b) the $1 \to 2$ configuration.

After Fourier transformation in the $y-$direction, the stationary states of the 1D effective chain for the two cases shown in Fig. (3.5) can be written as

$$|\psi_k\rangle = \sum_{j=1,2} \sum_m \left(\psi^{A,j}_{m,k} a^\dagger_{j,m,k} + \psi^{B,j}_{m,k} b^\dagger_{j,m,k}\right) |0\rangle\,, \tag{3.31}$$

with k the wave number along the y direction. Within the monolayer (lead) region, we define the column vector $\Psi^j_k\,(m) = \left[\begin{array}{cc} \psi^{A,j}_{m-1,k} & , \psi^{B,j}_{m,k} \end{array}\right]^T$ which obeys the transfer matrix equation (see Appendix 3.4),

$$\Psi^{1(2)}_k\,(m+1) = \mathbb{T}_L \Psi^{1(2)}_k\,(m)\ , \tag{3.32}$$

where $\mathbb{T}_L$ is given by

$$\mathbb{T}_L = \frac{1}{\xi\eta^*}\left[\begin{array}{cc} -|\xi|^2 & -\epsilon\xi \\ \epsilon\xi^* & \epsilon^2-|\eta|^2 \end{array}\right], \tag{3.33}$$

with $\eta = t\left(1+e^{ik}\right)$ and $\xi_k = t$. For the bilayer region ($1 \leq m \leq p$) we define $\boldsymbol{\Psi}_k\left(m\right) = \left[\begin{array}{cc} \Psi_k^1\left(m\right) & \Psi_k^2\left(m\right) \end{array}\right]^T$ obeying

$$\boldsymbol{\Psi}_k\left(m+1\right) = \mathbb{T}_{BL}\boldsymbol{\Psi}_k\left(m\right)\ , \tag{3.34}$$

where the transfer matrix $\mathbb{T}_{BL}$ is given by

$$\mathbb{T}_{BL} = \frac{1}{\eta^*\xi}\left[\begin{array}{cccc} -|\eta|^2 & -\epsilon\eta & 0 & 0 \\ \epsilon\eta^* & \epsilon^2-|\xi|^2 & 0 & -t_\perp \\ t_\perp\frac{|\eta|^2}{\xi^*} & t_\perp\frac{\epsilon\eta}{\xi^*} & -|\eta|^2 & -\epsilon\eta \\ -t_\perp\frac{\epsilon\eta^*}{\xi^*} & -t_\perp\frac{\epsilon^2}{\xi^*} & \epsilon\eta^* & \epsilon^2-|\xi|^2 \end{array}\right]. \tag{3.35}$$

The amplitudes at the left and the right interfaces can be related by,

$$\boldsymbol{\Psi}_k\left(p+1\right) = \left(\mathbb{T}_{BL}\right)^p\boldsymbol{\Psi}_k\left(1\right) \tag{3.36}$$

and by the boundary conditions: $\psi_{0,k}^{A2} = \psi_{p+1,k}^{B2} = 0$ for the 1 → 1 case, and $\psi_{0,k}^{A2} = \psi_{p+1,k}^{B1} = 0$ for the 1 → 2 case, as can be seen in Figs. 3.5(a) and 3.5(b). With these boundary conditions one obtains the matrix $\mathcal{M}_{1\to1(2)}$ relating the layer 1 in the left to layer 1(2) in the right,

$$\Psi_k^{1(2)}\left(p+1\right) = \mathcal{M}_{1\to1(2)}\Psi_k^1\left(1\right)\ , \tag{3.37}$$

where $\mathcal{M}_{1\to1(2)}$ are defined from Eq. (3.36) in Appendix 3.4.

Within the semi-infinite leads, Eq. (3.32) can be solved by assuming the ansatz

$$\Psi_k^{1(2)}\left(m\right) = \alpha_+\lambda_+^{m-1}\zeta_k^+ + \alpha_-\lambda_-^{m-1}\zeta_k^-\ ,$$

with $\mathbb{T}_L\zeta_k^\pm = \lambda_\pm\zeta_k^\pm$. The eigenvalues $\lambda_\pm$ and the eigenmodes $\zeta_k^\pm$ are explicitly derived in Appendix 3.4. In the leads we only consider propagating modes, so that $|\lambda| = 1$. The eigenmodes are thus interpreted as left-moving, ζ_j^-, and right-moving, ζ_j^+, modes, according to their group velocity (see Appendix 3.4). We then use the

$\zeta_k^{\pm}$ eigenbasis to write the wave function in the leads,

$$\Psi_k^{1(2)}(m) = \lambda_+^{m-1}\zeta_k^+ + \lambda_-^{m-1} r_k \zeta_k^- \quad , \quad m < 1 \tag{3.38}$$

$$\Psi_k^{1(2)}(m) = \lambda_+^{m-p-1}\tau_k \zeta_k^+ \quad , \quad m > p \, , \tag{3.39}$$

from which we define transmission and reflection coefficients, respectively τ and r. The transmission and reflection coefficients are given by,

$$\begin{bmatrix} \tau_k \\ 0 \end{bmatrix} = U^{-1}\mathcal{M}_{1\to 1(2)} U \begin{bmatrix} 1 \\ r_k \end{bmatrix} , \tag{3.40}$$

where $U = \begin{bmatrix} \zeta_k^+, & \zeta_k^- \end{bmatrix}$.

The transmission probability is then defined as $T(\epsilon, k), = 1 - |r_k|^2 = |\tau_k|^2$, and the overall transmission per transverse unit length is given by,

$$\bar{T}(\epsilon) = \frac{1}{2\pi}\int_{-\pi}^{\pi} dk T(\epsilon, k) \; . \tag{3.41}$$

Using the Landauer formula [147], we find the current per transverse unit length across the bilayer region,

$$I = \frac{2e}{h}\int d\epsilon \bar{T}(\epsilon)\left[f(\epsilon - \mu_L) - f(\epsilon - \mu_R)\right] \tag{3.42}$$

where $f(\epsilon)$ is the Fermi distribution function and $\mu_L(\mu_R)$ are the chemical potential in the left (right) lead (in the following we assume $\mu_L > \mu_R$). Assuming $\mu \equiv \mu_L = \mu_R + \delta\mu$, with $\delta\mu \ll \mu$, we can linearize the Landauer formula [108] to obtain the conductance $G \equiv e\delta I/\delta\mu$, which can be written as

$$G(\mu) = -G_0 \int d\epsilon T(\epsilon) \frac{\partial f(\epsilon - \mu)}{\partial \epsilon} , \tag{3.43}$$

where $G_0 = \frac{2e^2}{h}$ is the conductance quantum. For a system at zero temperature, Eq. (3.43) can be simplified to $G = G_0 T(\mu)$.

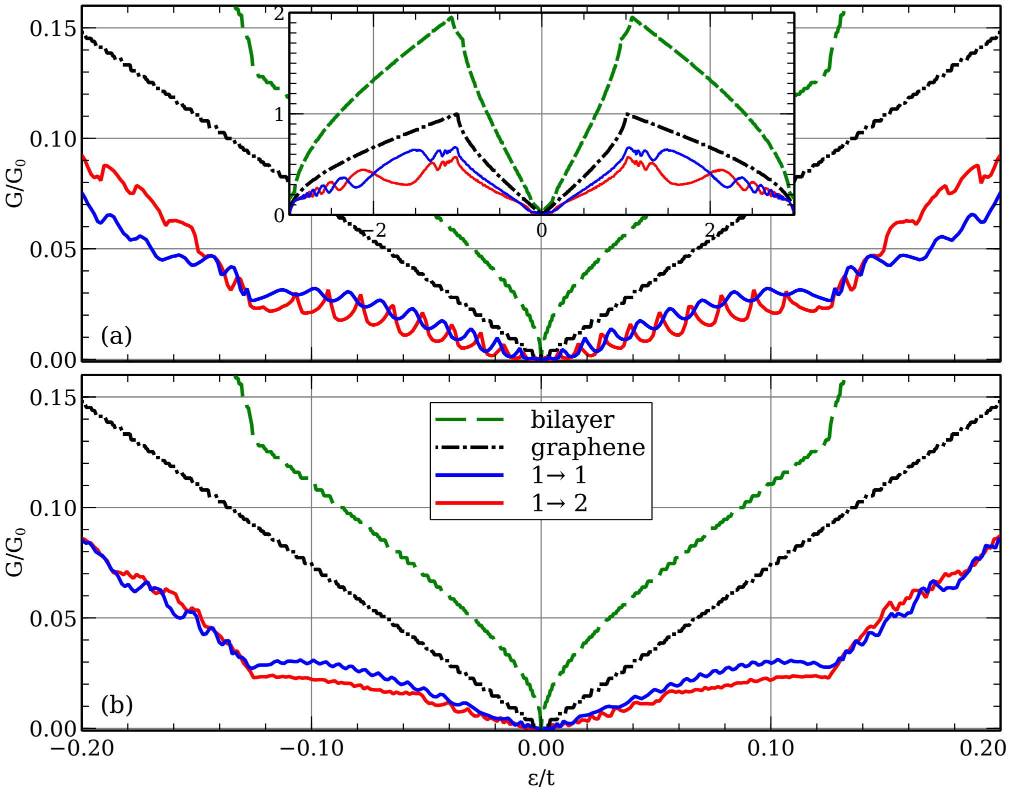

Figure 3.6: Transmission per transverse unit length near the Fermi-level for the $1 \to 1$ (blue), $1 \to 2$ (red) geometries plotted for $p = 200$ (a) and $p = 1500$ (b). The transmission for an infinite graphene layer (black dashed-dotted) and for an infinite bilayer (green dashed) are plotted for comparison. Inset: Transmission for the whole bandwidth for $p = 200$.

3.3.2 Transmission through a bilayer graphene region

In this section, we compute the transmission amplitudes for the $1 \to 1$ and $1 \to 2$ cases. A simplifying feature is that, for both cases, there is only one propagating incident mode associated with given ϵ, hence the corresponding transfer matrix of the leads is a two by two. Note that, due to electron-hole symmetry, $T(\epsilon, k) = T(\pm\epsilon, k)$.

Figure 3.6 shows the conductance for energies near the Fermi-level for the $1 \to 1$ (blue) and $1 \to 2$ (red) geometries and for two values of the scattering region size, $p = 200$, (a), and for $p = 1500$, (b). For comparison, the conductance through an infinite system consisting of a single (black dashed-dotted) or a double (green dashed) graphene layer is also depicted. Note that, in these cases the total transmission in Eq. (3.41) is simply determined by the dispersion relation. Therefore, for low energies it behaves as $\propto |\varepsilon|$ for the single layer and as $\propto |\varepsilon|^{1/2}$ for the bilayer.

For both geometries, the low energy conductance is almost twice as low as for pristine graphene and vanishes faster, with a $\propto |\varepsilon|^2$ scaling behavior. The inset of Fig. 3.6(a), depicting G for the all energies within the bandwidth, shows that, even away from the Fermi-level, G never attains the value of the pristine case.

Another pronounced low energy feature of the transmission is the sudden increase for energies around $t_\perp$. Thus, as also seen in the pristine double layer case, the conductance resolves the appearance of the higher energy band, after which two propagating modes become available for transport within the bilayer region.

The differences between the $1 \to 1$ and $1 \to 2$ geometries are more pronounced for higher energies. At low energies, they can be completely masked out by the finite-size effects that yield the characteristic jumps in the conductance, Fig. 3.6(a). For larger values of p, when the finite-size oscillations are reduced, the $1 \to 1$ case is seen to have a higher conductance. This is to be expected since in this case, the transmitted electrons do not have to change layer, which is suppressed for low values of $t_\perp$.

3.3.3 Conductance through a *gated* bilayer graphene region

3.3.3.1 Homogeneous case

In this section, we study the effect on the transmission of a gate voltage applied within the bilayer region. We assume that only one of the layers is affected by the gate while the other remains at zero voltage. We study the cases for which the voltage of the lower, V_1, or upper layers, V_2, is $0.04t$ or ten times larger $0.4t$, which correspond to typical values of gate voltages that can be implemented experimentally. Fig. 3.7 shows the conductance through a gated bilayer graphene region in different cases together with a plot of the band structure of the bilayer and the single layer leads around zero energy (computed assuming an infinite system). Fig. 3.7(b) depicts the $1 \to 1$ geometry for $V_1 = 0.04t$ and $V_2 = 0$ (blue) and for the swapped voltage configuration $V_1 = 0$ and $V_2 = 0.04t$ (green). The most pronounced features are the suppression of transport for $\varepsilon \in \{0, |\Delta V|\}$ and a jump in the conductance for $\varepsilon \approx |\Delta V|$ seen in 3.7(b) blue, which is not present when the gate voltages are swapped in 3.7(b) (green). The illustrations of the band structures in Figs. 3.7(a) and 3.7(c) help to understand this behavior. The effect of the gate voltage is to open up a gap in the dispersion relation of the bilayer. Moreover, while for $V_1 = V_2 = 0$, the wave-function's amplitudes are equally distributed between the two layers of the bilayer system, for finite voltages their distribution changes drastically near the gap edges (valence band maximum and conduction band minimum). The color coding in Fig. 3.7(a) and 3.7(c) shows the localization of the wave-function in the upper or lower layers. This energy-dependent layer distribution can simply explain the conduction jump: in the case depicted in 3.7(a), after passing the energy gap the system has suddenly available a large density of transmission modes within the lower layer. Such matching conditions (same color, at a given energy, for the leads and

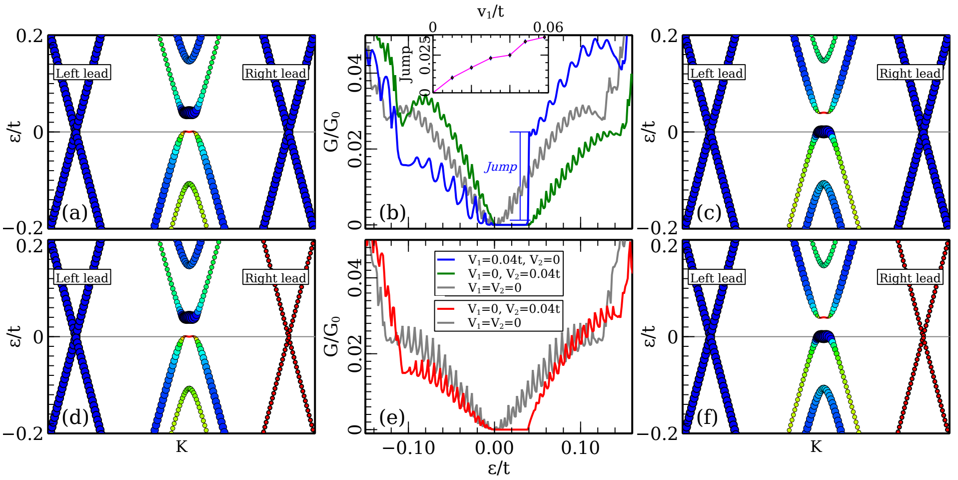

Figure 3.7: Conductance for a gated bilayer region. Upper panels refer to the geometry 1 → 1 (a-c) and lower panels to 1 → 2 (d-f). (b) Blue and (e) red correspond to $V_1 = 0.04t$ and $V_2 = 0$, computed for $p = 400$. For (b) green and (e) red: the values of the voltage are swapped, i.e. $V_1 = 0$ and $V_2 = 0.04t$. Notice that the geometry 1 → 2 is unchanged under swapping the gate voltage. The unbiased case $V_1 = V_2 = 0$ is depicted as a gray line for comparison. The dispersion relations at low energies, computed for an infinite system, corresponding respectively to the setups (b) blue , (b) green, and (e) red are given in (a), (c), (d) and (f). In each panel, the central dispersion corresponds to the bilayer region and the color (and the circle's radius) encodes whether the wave-function is localized in the bottom (blue and larger radius) or in the upper (red and smaller radius) layers. The left and right dispersions correspond to a single layer and follow the same color coding. Inset: The height of the jump in the conductance as a function of gate voltage.

the bilayer region) never arises in the opposite case, 3.7(b) green, as can be seen in 3.7(c). The height of the jump as a function of V_1 is shown in 3.7(b) as an inset. Figs. 3.7(e) depicts the transmission for the 1 → 2 geometry. This case is symmetric under the swapping of the voltages. In this case Figs. 3.7(d) and 3.7(f) show that the perfect matching conditions seen in 3.7(a) are never attained and thus no jump in conductance is observed.

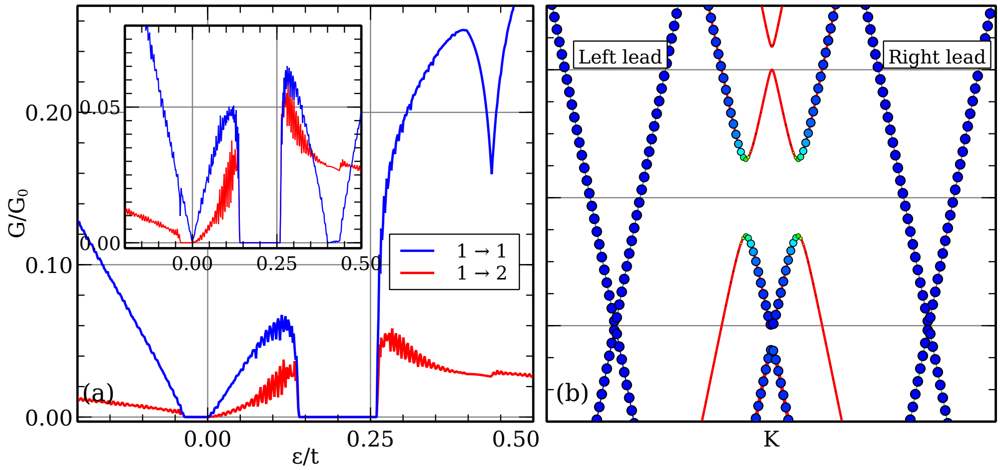

Figure 3.8: (a) Conductance for the gated bilayer region computed for $p = 400$ for the $1 \to 1$ (blue) and $1 \to 2$ (red) geometries with $V_1 = 0.4t$ and $V_2 = 0$. The inset depicts the opposite voltage configuration: $V_1 = 0$ and $V_2 = 0.4t$. (b) The dispersion relations at low energies, computed for an infinite system, corresponding to the setup (a). The central dispersion corresponds to the bilayer region and the color (and the circle's radius) encodes whether the wave-function is localized in the bottom (blue and larger radius) or in the upper (red and smaller radius) layers. The left and right dispersions correspond to a single layer and follow the same color coding.

The conductance attained when the gate voltage is increased by one order of magnitude is depicted in Fig. 3.8(a) for the two geometries $1 \to 1$ (blue) and $1 \to 2$ (red) for $V_1 = 0.4t$ and $V_2 = 0$. The inset shows the voltage swapped case, $V_1 = 0$ and $V_2 = 0.4t$. Fig. 3.8(b) depicts the band structure, with the same color coding as before, corresponding to the case $1 \to 1$ and $V_1 = 0.4t$ and $V_2 = 0$. An interesting feature of the transmission in Fig. 3.8(a) is that there are two regions where the conduction seems to vanish. One, at higher energies, corresponds to the band-gap and thus the suppression of the conductance is not surprising. However, the second arises within a region where the density of states is finite. Again, the plot of the band structure in Fig. 3.8(b) can simply explain this effect: the gap in conductance corresponds to a region where the conducting states with support on the lower layer become gapped, so although the total density of states is finite, there are no states contributing to transport.

3.3.3.2 Inhomogeneous case: single domain wall

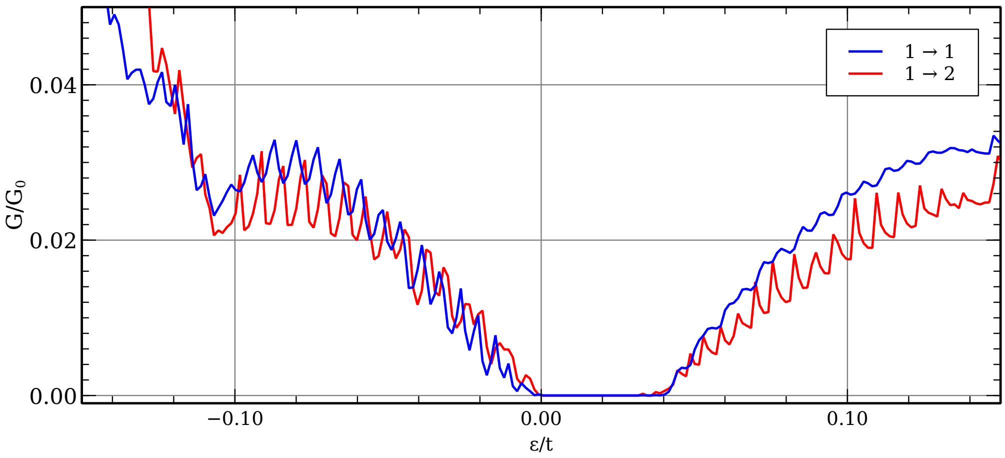

Figure 3.9: Conductance for the bilayer region with a gate voltage domain wall in the middle, computed for $p = 400$ in the $1 \to 1$ (blue) and $1 \to 2$ (red) geometries with $V_0 = 0.04t$.

In this section, we study how the transmission is affected by the presence of an inhomogeneous gate voltage. We consider the simplest case where a gate voltage domain wall is present in the bilayer region. We assume that the local potential at cell m, layer j (see Fig. 3.5) is given by $V_{m,j} = V_0\Theta\left[(-1)^j\left(m - \frac{p}{2}\right)\right]$, with $\Theta(x)$ the Heaviside function. Therefore, the potential difference on the left half ($m < p/2$) is $V_1 - V_2 = V_0$ while on the right half ($m > p/2$) it is $V_1 - V_2 = -V_0$, which implies a domain wall right at the middle of the bilayer region. This domain wall structure is known to support confined states, localized in the transverse direction and extending along the wall [141], with important consequences regarding transport in the direction of the wall [50]. The impact of a domain wall on charge transport in the perpendicular direction has not been studied before and is analyzed in the following. In Fig. 3.9 we show the conductance for the geometries $1 \to 1$ (blue) and $1 \to 2$ (red) for $V_0 = 0.04t$. The two geometries now have very similar conductance, which contrasts with the case when no domain wall is present, depicted in Figs. 3.7(b) and 3.7(f). A noticeable difference is the absence of the jump in conductance observed for the $1 \to 1$ geometry in Fig. 3.7(b). Since the domain wall reverses the layer distribution of the wave-function's amplitudes, the perfect matching conditions seen in 3.7(a) are never attained and thus no jump in conductance is observed. We conclude that the domain wall erases the difference between the two geometries. As shown in Ref. [141], the states confined at the domain wall originate one-dimensional bands dispersing inside the bulk gap. In Fig. 3.9 the impact of those states is unnoticeable, as a well resolved gap of order $\sim V_0$ is still apparent. This can be understood as a consequence of transverse confinement. At low energies, the wave function of these states has a decay length of the order $\beta \approx a_0 t/\sqrt{V_0 t_\perp} \gg a_0$, where a_0 is the carbon-carbon distance [141]. For $V_0 = 0.04t$ the decay length is $\beta \approx 8a_0$, much smaller than the distance $l = 200a_0$ between the domain wall and the edges of the scattering region. Therefore, for a single domain wall, these states do not contribute in propagating charge across the bilayer region.

3.3.4 Conductance through a *microstructured* biased bilayer graphene region

We now generalize our study to multiple domain walls. Our aim is to show how these microstructures, that are now routinely fabricated, can be used to engineer the transmission. We consider the potential of the previous section generalized for a periodic gated region of size l, $V_{m,1} = V_0 \Theta_l\left[m\right]$, where

$$\Theta_l\left[m\right] = \begin{cases} 1 & \text{if } 2kl/a_0 < m < \left(2k+1\right) l/a_0 \text{ for } k \in \mathbb{Z} \\ 0 & \text{if else} \end{cases},$$

and $V_{m,2} = V_0 \left(1 - \Theta_l\left[m\right]\right)$. As a function of l, there are two qualitatively different cases that we consider in the following: a large domain length, $l \gg \beta$, where the edge modes along the domain wall do not hybridize and thus do not contribute to the transport properties; and a small domain length, $l \lesssim \beta$, for which there is hybridization of edge modes and thus transport for energies within the bulk gap becomes possible. Figure 3.10 shows the evolution of the conductance curves with l. We consider, as before, $V_0 = 0.04t$ corresponding to $\beta \approx 8a$. In Fig. 3.10(a) we show the conductance for $l = 80a_0 \gg \beta$. As for the $l = p/2$ case in the previous section, the differences between the two geometries are not significant and there is almost no conductance within the gap, for $\varepsilon \in \{0, V_0\}$. Figure 3.10(b) depicts the conductance for a smaller value of $l = 20a_0$. Here, there are already some states within the gap that contribute to transport which result from the hybridization of the edge modes along the domain walls. In Fig. 3.10(c) we set $l = 5a_0$, for which the domain wall states are already fully hybridized. Note the striking similarity between the low energy conductance and that obtained for an unbiased bilayer region, shown in Fig. 3.6 and as a background in Figs. 3.7(b-c) and 3.7(f-g). It is clear that the effect of the gap has been completely washed out. At higher energies, however, the system still shows the conductance asymmetry typical of a gate biased bilayer region [see Figs. 3.7(b-c) and 3.7(f-g)].

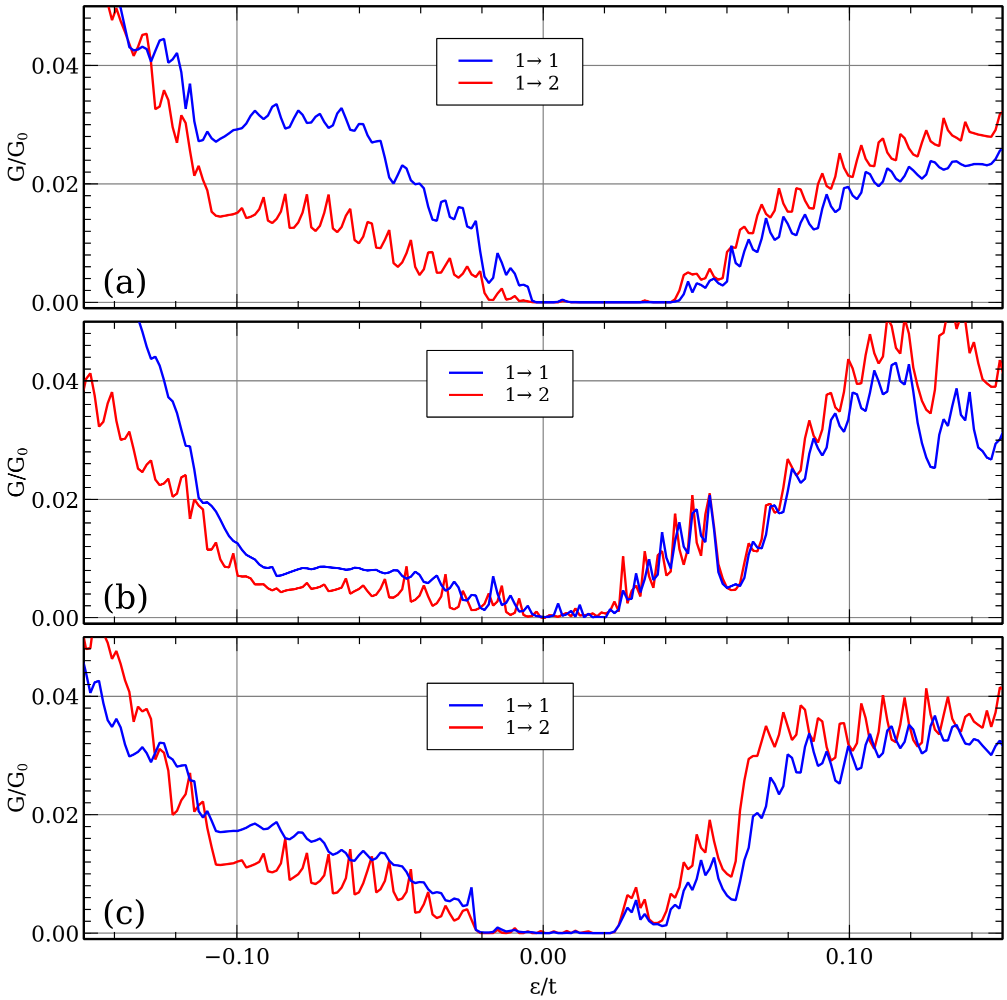

Figure 3.10: Conductance for the 1 → 1 (Blue) and the 1 → 2 (red) geometries in the presence of multiple domain walls separated by l lattice spacings, computed for $V_0 = 0.04t$. (a) $l = 80a_0 \gg \xi$. (b) $l = 20a_0 > \xi$. (c) $l = 5a_0 \approx \xi$.

3.3.5 Results for current at finite temperature and device application

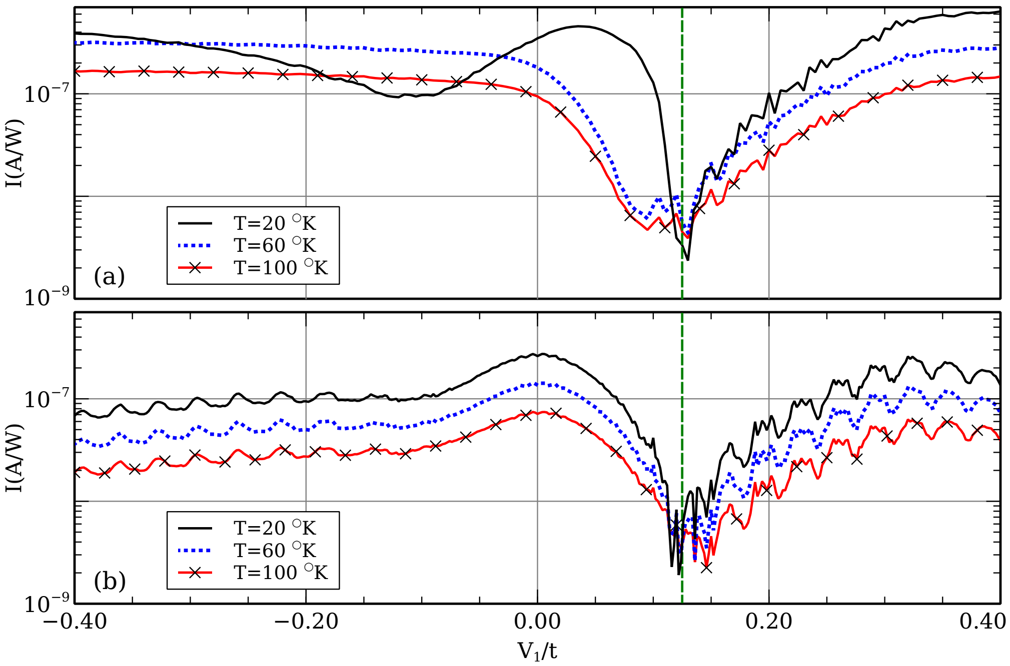

Figure 3.11: Current as a function of gate voltage for the setup of Fig. 3.7(b) as a function of V_1 (for $V_2 = 0$) computed for $p = 200$ and different values of the temperature for the $1 \to 1$ (a) and $1 \to 2$ (b) geometries. For ease of reading the curves are equally shifted.

In this section, we study the viability of an integrated nano-transistor based on the $1 \to 1$ or $1 \to 2$ geometries. For this device, one aims to maximize the current ratio between the "on" and "off" currents, $I_{\rm on}$ and $I_{\rm off}$, passing through the terminals, when changing between two values of the applied gate voltage. Due to its low resistance and versatility, graphene is a natural candidate for transistor implementations. However, due to the nature of its band structure, achieving a high on/off ratio is a technical challenge especially at finite temperature. We exploit the non-linear behavior of the conductance obtained with the setup of Fig. 3.7(b) to optimize the $I_{\rm on}/I_{\rm off}$ and study its behavior at finite temperature. Figure (3.11) shows the logarithmic plot of the current for the $1 \to 1$, panel (3.11)(a), and $1 \to 2$, panel (3.11)(b), setups for different temperatures as a function of gate voltage V_1. The chemical potentials on the left and right leads were fixed at the experimentally reasonable values of $\mu_{\rm L} = 0.1t$ and $\mu_{\rm R} = 0$. In the gate voltage interval $0 < V_1 < 0.2t$ this setup can achieve $50 \lesssim I_{\rm on}/I_{\rm off} \lesssim 200$.

3.3.6 Chapter conclusion

In this chapter we have studied the conductance in hybrid monolayer-bilayer-monolayer structuteres both in 1D, chain-ladder-chain, and in 2D, for the case of honeycomb lattice. We observed resonant transmission across a ladder where the number of oscillations changes with ladder length, p. These Fabry-Perot like fluctuations are reproducible. They are maybe due to the mismatching between the lead and bilayer wavefunctions at the interfaces. We have also studied the conductance across a graphene bilayer region for two different positions of the single layer leads: the case when the leads connect to the same layer, the $1 \to 1$ configuration; and the case when the leads connect to different layers, $1 \to 2$ configuration. We have worked in the limit of an infinitely wide scattering region, to avoid edge effects, and developed a transfer matrix, tight-binding based methodology which allows going away from linear response. We have found that, when there is no gate bias applied to the bilayer region, the two setups, $1 \to 1$ and $1 \to 2$, have a similar behavior, with a slightly higher conductance in the $1 \to 1$ configuration. The presence of a bias gate voltage differentiates between the two configurations. Both of them develop a conductance gap which mimics the spectral gap of a biased bilayer, but only the $1 \to 1$ configuration shows a pronounced conductance step at one of the gap edges, extending the results obtained in the continuum limit [43] and for ribbons of finite width [144]. This step is not present if the gate polarity is reversed. Introducing a domain wall in the gate bias applied to the bilayer region, the conductance step disappears and the two configurations, $1 \to 1$ and $1 \to 2$, behave again in a similar way. We have also studied the effect of a gate bias with a multiple domain wall microstructure applied to the bilayer region. When the separation between domains is much larger than the localization length of the states confined at the domain walls, the multiple domain walls states behave independently and the result is similar to the case of a single domain wall. On decreasing the separation between domain walls, the localized states start to hybridize and a finite conductance starts to appear inside the gap. At even smaller distances, the gap is completely washed out, and only at higher energies a conductance asymmetry characteristic of a gate biased bilayer region is present. Finally, we have studied the viability of an integrated nano-transistor based on the $1 \to 1$ or $1 \to 2$ geometries. For experimentally reasonable chemical potential difference ($\sim 0.3\,\mathrm{eV}$) and gate voltage interval (from 0 up to $\sim 0.6\,\mathrm{eV}$) we have found that this setup can achieve $50 \lesssim I_{\mathrm{on}}/I_{\mathrm{off}} \lesssim 200$. Summing up all the finds, it is clear the transmission through a bilayer region can be manipulated by a gate bias in ways not previously anticipated.

3.4 Chapter Appendix

A. The transmission through a bilayer region

Here we detail the transfer matrix method used to obtain the transmission coefficient. We apply Fourier transformation,

$$a^{\dagger}_{j,m,k}\left(b^{\dagger}_{jm,k}\right) = \frac{1}{\sqrt{N_y}}\sum_{n}\exp\left(ikn\right)a^{\dagger}_{j,m,n}\left(b^{\dagger}_{j,m,n}\right),$$

to the tight-binding Hamiltonian (3.28) and obtain

$$\begin{aligned} H_k = &-\sum_{j,m} a^{\dagger}_{j,m,k}\left[\eta b_{j,m,k} + \xi b_{j,m+1,k}\right] \\ &+\sum_{j,m}^{BL} V_j\left[a^{\dagger}_{j,m,k}a_{j,m,k} + b^{\dagger}_{j,m,k}b_{j,m,k}\right] + \text{H.c.} \\ &- t_{\perp}\sum_{m}^{BL} a^{\dagger}_{1,m,k}b_{2,m,k} + \text{H.c.} \end{aligned} \tag{3.44}$$

where η and ξ are defined in the main text.

By multiplying $H_k|\psi_k\rangle = \epsilon_k|\psi_k\rangle$by $\langle m,l,\mu|$, for a given lattice point (m,l,μ), where m stands for position, l for layer, and $\mu = A, B$ labels sublattices, one obtains, for the leads where $m < 0$ or $m > p+1$,

$$\begin{aligned} \epsilon\psi^{A1}_{m,k} &= -\eta\psi^{B1}_{m,k} - \xi\psi^{B1}_{m+1,k} \\ \epsilon\psi^{B1}_{m,k} &= -\eta^{*}\psi^{A1}_{m,k} - \xi^{*}\psi^{A1}_{m-1,k}, \end{aligned}$$

with $\psi^{\mu l}_{m,k} = \langle m,\mu,l|\psi_k\rangle$. We rewrite the latter equations in a matrix equation form as

$$\begin{bmatrix} \epsilon & \xi \\ \eta^{*} & 0 \end{bmatrix}\begin{bmatrix} \psi^{A1}_{m,k} \\ \psi^{B1}_{m+1,k} \end{bmatrix} = -\begin{bmatrix} 0 & \eta \\ \xi^{*} & \epsilon \end{bmatrix}\begin{bmatrix} \psi^{A1}_{m-1,k} \\ \psi^{B1}_{m,k} \end{bmatrix}, \tag{3.45}$$

which is equivalent to Eq. (3.32).

Similar steps can be taken to build the transfer matrix for the bilayer region where $1 \leq m \leq p$,

$$\begin{aligned}
(\epsilon_k - V_1)\,\psi^{A1}_{m,k} &= -\eta\psi^{B1}_{m,k} - \xi\psi^{B1}_{m+1,k} - t_\perp\psi^{B2}_{m,k} \\
(\epsilon_k - V_1)\,\psi^{B1}_{m,k} &= -\eta^*\psi^{A1}_{m,k} - \xi^*\psi^{A1}_{m-1,k} \\
(\epsilon_k - V_2)\,\psi^{A2}_{m,k} &= -\eta\psi^{B2}_{m,k} - \xi\psi^{B2}_{m+1,k} \\
(\epsilon_k - V_2)\,\psi^{B2}_{m,k} &= -\eta^*\psi^{A2}_{m,k} - \xi^*\psi^{A2}_{m-1,k} - t_\perp\psi^{A1}_{m,k},
\end{aligned}$$

from which we obtain Eq. (3.34) in matrix form.

By imposing the boundary conditions for setup 1 → 1, and defining $\mathbb{M} = (\mathbb{T}_{BL})^p$, we can re-write Eq. (3.36) as

$$\begin{bmatrix} \psi^{A1}_{p,k} \\ \psi^{B1}_{p+1,k} \end{bmatrix} = \mathcal{M}_{1\to 1} \begin{bmatrix} \psi^{A1}_{0,k} \\ \psi^{B1}_{1,k} \end{bmatrix} , \tag{3.46}$$

or equivalently,

$$\Psi^1_k\,(p+1) = \mathcal{M}_{1\to 1}\Psi^1_k\,(1)\ , \tag{3.47}$$

where

$$\mathcal{M}_{1\to 1} = \frac{1}{\mathbb{M}_{44}} \begin{bmatrix} \mathbb{M}_{11}\mathbb{M}_{44} - \mathbb{M}_{14}\mathbb{M}_{41} & \mathbb{M}_{12}\mathbb{M}_{44} - \mathbb{M}_{14}\mathbb{M}_{42} \\ \mathbb{M}_{21}\mathbb{M}_{44} - \mathbb{M}_{24}\mathbb{M}_{41} & \mathbb{M}_{22}\mathbb{M}_{44} - \mathbb{M}_{24}\mathbb{M}_{42} \end{bmatrix} .$$

Using the boundary condition for the setup 1 → 2, we obtain, after similar steps,

$$\Psi^2_k\,(p+1) = \mathcal{M}_{1\to 2}\Psi^1_k\,(1)\ , \tag{3.48}$$

where

$$\mathcal{M}_{1\to 2} = \frac{1}{\mathbb{M}_{24}} \begin{bmatrix} \mathbb{M}_{24}\mathbb{M}_{31} - \mathbb{M}_{34}\mathbb{M}_{21} & \mathbb{M}_{24}\mathbb{M}_{32} - \mathbb{M}_{34}\mathbb{M}_{22} \\ \mathbb{M}_{24}\mathbb{M}_{41} - \mathbb{M}_{44}\mathbb{M}_{21} & \mathbb{M}_{24}\mathbb{M}_{42} - \mathbb{M}_{44}\mathbb{M}_{22} \end{bmatrix} .$$

The last step is to represent wave amplitudes $\Psi^{1(2)}_k\,(m)$ in the eigenbasis of the transfer matrix of the leads. The characteristic equation for the eigenvalue problem $\mathbb{T}_L\zeta_k = \lambda\zeta_k$ reads,

$$(\xi_k\eta^*_k)\,\lambda^2 - \left(\varepsilon^2 - |\xi_k|^2 - |\eta_k|^2\right)\lambda + \xi^*_k\eta_k = 0\,, \tag{3.49}$$

yielding two eigenvalues,

$$\lambda_\pm = \frac{1}{\xi_k\eta^*_k}\left(\varepsilon^2 - |\xi_k|^2 - |\eta_k|^2 \pm \sqrt{\left(\varepsilon^2 - \delta^2_+\right)\left(\varepsilon^2 - \delta^2_-\right)}\right)\ , \tag{3.50}$$

where $\delta_{\pm} = |\xi_k| \pm |\eta_k|$, corresponding to the normalized eigenvectors

$$\zeta_k^{\pm} = \frac{1}{\sqrt{2}} \begin{pmatrix} 1 \\ \frac{-\varepsilon}{\xi_k^* + \eta_k^* \lambda_{\pm}} \end{pmatrix} . \tag{3.51}$$

A mode with positive (negative) group velocity is considered to be the right-moving(+) (left-moving(-)) mode. Recalling that in the leads $|\lambda| = 1$ and using Bloch theorem for the Pristine graphene $\lambda = e^{iq(k,\varepsilon)}$, where $q\,(k, \varepsilon)$ is the conjugate momentum in $\mathbf{a}_1$(propagating) direction, and plugging the latter expression into Eq. (3.49) we obtain the mode group velocity in the propagating direction as:

$$v_g = \frac{d\varepsilon}{dq} = \frac{-1}{\varepsilon} Im\left(\xi_k \eta_k^* \lambda\,(k, \varepsilon)\right) . \tag{3.52}$$

4 Quantum transport through a twisted bilayer graphene region

4.1 Outline of the chapter

This chapter continues the discussion of the previous chapter on the transport properties in monolayer-bilayer-monolayer (MBM) structure. Here the bilayer central region is twisted bilayer graphene (tBLG). Following the introductory section 2.3.2, small angle rotation faults, may naturally exist in graphite crystals as a result of the weak van der Waals (vdW) interaction of the layers. This relative rotations are manifested via the long-periodic Moiré patterns. It is therefore worthwhile to consider transport in the presence of such patterns. In general, such patterns do not lead to a regular lattice nor a well-defined reciprocal lattice as translational invariance is broken. In the absence of Bloch's theory, most computation tools that take the advantages of translational symmetry to simplify the calculations are no longer available. Even, semi-analytical approaches, have limited validity and need to be validated against numerical analysis. Thereforethe foundation of this chapter is mainly based on numerical analysis. For some specific twist angles we also use an approximation method to provide a better picture of transport in our hybrid structure.

Similar to previous chapter, we outline some important features and assumptions valid for our system,

1. Monolayers are semi infinite zigzag graphene ribbons with width, W.
2. Monolayers are metallic and act as carrier reservoirs or contacts which we refer to as leads.
3. Bilayer region is essentially made by stacking of two monolayer flakes with a relative rotation, θ, of the top layer with respect to the bottom layer.
4. In order to keep the number of atoms in the bilayer region almost constant for different rotations, the central region is in a disk shape, see Fig. 4.1.

This chapter is based on both unpublished work and on the following publication by the author:

- *Charge transport in twisted bilayer graphene,* Hadi Z. Olyaei, Bruno Amorim, Pedro Ribeiro, and Eduardo V. Castro to be submitted soon.

The structure of the chapter is as follows: Sec. 4.2 includes an introduction to the twisted bilayer graphene and and a literary survey. In Sec. 4.3, we we introduce the model and describe the methodology used to calculate the conductance and the DOS. In Sec. 4.4, some representative results of transmission are presented for different angle regimes. Section 4.5 contains a short summary and the conclusions.

4.2 Transport in monolayer-twisted bilayer-monolayer hybrid structure

We study the conductance across a twisted bilayer graphene coupled to single-layer graphene leads. We find a strong angle dependence with three qualitatively different regimes. For large angles ($\theta \gtrsim 10^\circ$) there are strong commensurability effects. For large incommensurate angles, the two graphene layers effectively decouple. Large commensurate angles, corresponding to a small unit cell, appear as sharp features in the conductance. For intermediate angles ($3^\circ \lesssim \theta \lesssim 10^\circ$), we find a correlation of the conductance features with the twist angle, which suggests that conductance measurements can be used to determine the twisting angle. For small twisting angles ($1^\circ \lesssim \theta \lesssim 3^\circ$) we find that commensurate effects are washed out and the conductance becomes a smooth function of the angle. Conductance can be used to probe the almost flat bands appearing in this regime. Our results agree with the recent experimental findings where zero conductance regions have been correlated with gaps in the density of states.

The discovery of both correlated insulating phases [135] and superconductivity [134] in twisted bilayer graphene (tBLG) is a paradigmatic example of tunability in two-dimensional quantum systems. By changing the twist angle between the two graphene layers a strong renormalization of the Fermi velocity can be achieved, with small velocities occurring for smaller angles [34]. In the small angle regime, $\theta \lesssim 1^\circ$, extremely narrow bands appear at low energies, with the Fermi velocity vanishing at specific *magic angles* when the bands become flat [95, 57, 96, 91, 90]. It is in this extremely narrow band regime that unexpected insulating and superconducting states are observed, pointing to electron correlations as key players. This triggered an intense research interest both from the theory [148, 149, 150, 151, 152, 153, 154, 155, 156, 157, 158, 159, 160, 161, 162, 163, 164, 165, 166, 167, 168, 169, 170, 171, 172, 173, 174, 175, 176, 177, 178, 179, 180, 181, 182, 183, 184, 185, 186, 187, 188, 189, 190, 191, 192, 193, 194, 195, 196, 197] and the experimental [198, 199, 200, 201, 202, 203, 204, 205, 206, 207, 208, 209] sides. The flat band regime induced by a finite twist has also been explored experimentally in graphene double bilayers [210, 211, 212] and trilayers [213, 214], and is also relevant to other two-dimensional materials [215, 216].

The rotation between layers introduces a long-wavelength modulation of the lattice structure called Moiré pattern [72]. For small angles, the Moiré wavelength is much larger than the carbon-carbon distance, with the ratio growing as $1/\theta$. This represents an additional difficulty regarding the theoretical description of the system, since a single Moiré may contain several thousands of atoms in the low angle regime. While the minimum Wannier-like tight binding parametrization describing the narrow band sector on the Moiré scale is still debated [217, 149, 148, 155, 158, 186], the original atomic tight binding model rests a faithful description, despite the large unit cells at smaller angles [95, 57, 91, 90, 218, 35].

Transport measurements in tBLG have been crucial to characterize the small angle regime around the neutrality point. The existence of transport gaps delimiting the Moiré band energy sector have been observed in Refs. [219, 31, 198] for tBLG with $\theta \sim 2°$. These are the so called *superlattice* induced gaps, observed when the Moiré bands are completely occupied, for a carrier density $n = +n_{\mathrm{S}}$, or fully empty, $n = -n_{\mathrm{S}}$. Conductance measurements as a function of n have been performed for $\theta \approx 1.1°$, close to the first magic angle. Apart from the gaps at $n = \pm n_{\mathrm{S}}$, insulating behavior was detected at half-filling, $n = \pm n_{\mathrm{S}}/2$, which cannot be explained within the single particle picture [135]. By changing the carrier density around $n = \pm n_{\mathrm{S}}/2$, the resistance drops to zero signaling the transition to a superconducting state for temperatures below $T \approx 1.0\,\mathrm{K}$ [134, 199]. Measuring the conductance allowed also to detect insulating behavior at the fractional fillings $n/n_{\mathrm{S}} = 1/4, 3/4$ [199, 200, 209, 220], and for a larger angle, $\theta \simeq 1.27°$, after applying pressure [199]. Furthermore, transport measurements are sensitive to the atomic reconstruction seen at smaller angles, $\theta < 1°$ [221], and transport have been an essential tool to inspect for similar physical behavior in twisted double bilayers [212, 210]. Conductance measurements have also been employed recently to analyze the role of Coulomb screening in both insulating and superconducting phases of tBLG [222].

The transport properties of tBLG have been studied theoretically in the linear regime using the Kubo formalism in Ref. [223]. The conductivity due to small disorder broadening of the energy states has been obtained as a function of the twist angle. A finite concentration of vacancies was shown to suppress the conductivity in a wide energy region. In Refs. [224, 225], impurity and phonon scattering, with particular emphasis on the temperature dependence of the resistivity, have been discussed. In the ballistic regime, an earlier work addressed the transport properties of nanoribbons with a large angle tBLG section [226]. The importance of edge effects have been put forward due to the small width of the considered nanoribbons. Recently, a wider single layer graphene nanoribbon with a twisted graphene flake on top was studied in Ref. [227]. An interesting orbital magnetic structure have been predicted at finite source-drain voltage applied only to the graphene nanoribbon. This effect is attributed to the presence of counterflow currents first discussed in [95]. The effect of a spatially inhomogeneous twist angle - twist disorder - in transport properties has recently been considered in Ref. [228]. However, the ballistic conductance of tBLG in the full twist angle regime and for both commensurate and incommensurate structures, to the knowledge of the authors, has not been considered before. Given the importance of conductance measurements to study the physics of this system, usually at very low temperatures using high quality samples, knowing the behavior of the conductance in the clean, ballistic regime is of paramount importance.

In this chapter, we address the transport properties of tBLG in the ballistic regime from large to small twist angles. The conductance was computed both for commensurate and incommensurate angles. In the large angle regime, the results are shown to be sensitive to commensurability effects. For intermediate angles, we find conductance features correlating with the position of the van Hove singularities in the density of states (DOS), which is also computed. In the small angle regime, commensurability effects completely disappear. Superlattice induced gaps are clearly resolved, in agreement with experiments.

4.3 Model and methods

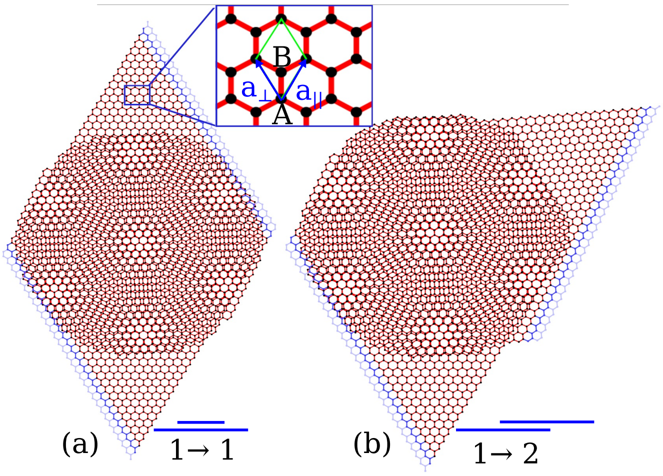

Figure 4.1: Twisted bilayer setups used in this work: (a) 1 → 1 and (b) 1 → 2 setup. Vanishing blue color denotes the beginning of semi-infinite leads. Lateral views are shown under each setup. The typical linear size of the scattering region is hundred of nanometers.

In order to study the conductance of tBLG as a function of twist angle we define two different setups, schematically shown in Fig. 4.1. In the first setup, shown in Fig. 4.1(a) and denoted 1 → 1, a graphene ribbon is overlaid by a disk of single layer graphene. The diameter of the disk is the same as the width of the ribbon. The orientation of the disk is chosen so that the two layers define a circularly shaped tBLG region with the desired twist angle. The second setup, denoted 1 → 2, is shown in Fig 4.1(b). In this case we use two semi-infinite graphene ribbons with overlapping ends. Semi-circular edges at the end of each ribbon define an almost circular tBLG region. By adjusting the relative orientation of the ribbons we fix the twist angle. In both setups, the remaining of the monolayer ribbons define semi-infinite leads.

We model p_z electrons in tBLG through a microscopic tight binding Hamiltonian reading $H = H_1 + H_2 + H_\perp$, where H_l, with $l = 1, 2$, is the Hamiltonian for a single layer, and $H_\perp$ is the interlayer coupling. For the single layer Hamiltonian we write,

$$H_l = -t \sum_{\substack{\mathbf{R}_l, \mathbf{R}'_l \\ |\mathbf{R}_l - \mathbf{R}'_l| \leq a}} c^\dagger_{l,\alpha} \left(\mathbf{R}_l\right) c_{l,\beta} \left(\mathbf{R}'_l\right) \,, \tag{4.1}$$

where $c^\dagger_{l,\alpha} \left(\mathbf{R}_l\right)$ creates an electron at the Bravais lattice position $\mathbf{R}_l$, of layer l and sublattice $\alpha = A, B$, and the constraint $|\mathbf{R}_l - \mathbf{R}'_l| \leq a$, with $a = 1.42\,\text{Å}$ for the carbon-carbon bond length, ensures nearest neighbor hopping in each layer. The interlayer coupling is written as $H_\perp = H_{12} + H_{21}$, with

$$H_{12} = \sum_{\mathbf{R}_1, \mathbf{R}_2} t^{\alpha\beta}_{12} \left(\mathbf{R}_1, \mathbf{R}_2\right) c^\dagger_{1,\alpha} \left(\mathbf{R}_1\right) c_{2,\beta} \left(\mathbf{R}_2\right) \,, \tag{4.2}$$

where $t^{\alpha\beta}_{12} \left(\mathbf{R}_1, \mathbf{R}_2\right)$ is the interlayer hopping in the tight binding basis.

To parameterize the interlayer hopping in Eq. (4.2), we use the two-center approximation and assume $t^{\alpha\beta}_{12} \left(\mathbf{R}_1, \mathbf{R}_2\right)$ depends only on the distance r between the two p_z-orbitals,

$$t^{\alpha\beta}_{12} \left(\mathbf{R}_1, \mathbf{R}_2\right) \equiv t^{\alpha\beta}_{12}(r) \,,$$

with $r^2 = d^2_\parallel + d^2_\perp$ for an interlayer separation $d_\perp = 3.35\,\text{Å}$ and an in-plane projected distance $d_\parallel = \mathbf{R}_1 + \boldsymbol{\tau}_{1,\alpha} - \mathbf{R}_2 - \boldsymbol{\tau}_{2,\beta}$ between, where $\boldsymbol{\tau}_{l,\alpha}$ are the positions of the orbital centers in the unit cell of each layer. Since the sites in A and B sublattices correspond to the same p_z orbital, we further assume that the interlayer hopping does not depend on the sublattice index, $t^{\alpha\beta}_{12}(r) \equiv t_\perp(r)$. Using the Slater-Koster parameterization [229], we write

$$t_\perp \left(r\right) = \cos^2 \left(\gamma\right) V_{pp\sigma} \left(r\right) + \sin^2 \left(\gamma\right) V_{pp\pi} \left(r\right) \,, \tag{4.3}$$

where the angle γ is such that $\cos^2 \left(\gamma\right) = d^2_\perp / r^2$, and following Ref. [230] the spatial dependence of the parameters is given by

$$\begin{aligned} V_{pp\sigma}(r) =& t_\perp \exp\left[q_\sigma\left(1-\frac{r}{d_\perp}\right)\right], \\ V_{pp\pi}(r) =& -t\exp\left[q_\pi\left(1-\frac{r}{a}\right)\right]. \end{aligned} \tag{4.4}$$

From the second neighbor intralayer hopping, $t' = 0.1t$, we fix $q_\pi = 3.15$, and assuming $q_\pi/a = q_\sigma/d_\perp$ yields $q_\sigma = 7.42$ [72]. For the remaining parameters, we consider $t = 2.79\,\mathrm{eV}$ and $t_\perp = 0.35\,\mathrm{eV}$.

To model the interlayer coupling $H_\perp$, we retain hopping from each site in layer 1 to the closest sites of layer 2 in either sublattice, and vice versa, as long as $|\mathbf{R}_1 - \mathbf{R}_2| < 0.9a$. Including further distance interlayer hopping terms does not alter the description of tBLG in a fundamental way [57]. One advantage of the truncation we have chosen is that the first magic angle occurs at a slightly larger value, $\theta^* \approx 1.6°$, thus for a slightly smaller Moiré *cell.*

The conductance, G, is computed within the Landauer approach. At zero temperature and in the linear regime, the conductance is proportional to the transmission, $T(\epsilon)$, for a system with chemical potential ϵ. We define $\bar{T}(\epsilon) = T(\epsilon)/w$, where w is the width of the leads, and write the conductance as $G = G_0\bar{T}(\epsilon)$, where $G_0 = \frac{2e^2}{h}$ is the conductance quantum. For both setups shown in Fig. 4.1, the circular tBLG region with diameter w defines the scattering region, which, by construction, is connected to two semi-infinite leads of width w. We compute the transmission, $T(\epsilon)$, from the left lead to the right lead using the Kwant package [52]. Conductance calculations are performed with a scattering region containing $\mathcal{N} = 3.77 \times 10^5$ carbon atoms for twist angles $2° < \theta < 58°$. For structures with smaller twisting angles, $0 < \theta \leq 2°$ and $58 \leq \theta < 60°$, the size is four times larger, $\mathcal{N} = 1.56 \times 10^6$ carbon atoms. The number of Moiré *cells* in the scattering region ranges from $\gtrsim 150$ for the smallest angles to several thousands for larger angles. DOS calculations for incommensurate angles are done based on the kernel polynomial method, also provided in Kwant. In this case, the size of the tBLG circular region was kept at $\mathcal{N} = 1.56 \times 10^6$ carbon atoms for angles in the range $2° < \theta < 58°$, and $\mathcal{N} = 4.6 \times 10^6$ carbon atoms for smaller angles, $0 < \theta \leq 2°$ and $58 \leq \theta < 60°$. The DOS for commensurate structures was obtained through exact diagonalization.

4.4 Results and Discussion

In this section, we present results for the conductance through a tBLG region as a function of the twist angle between the two layers for both setups shown in Fig. 4.1. We start with the analysis of general features regarding the twist angle dependence, and then move on to discuss three dinstinct regimes: large, intermediate, and small angles.

4.4.1 General features

The conductance, G, of tBLG as a function of twist angle, θ, for an energy window $\varepsilon \in [-t, t]$, is shown in Figs. 4.2(a) and 4.2(b) for the two setups $1 \to 2$ and $1 \to 1$, respectively. Generally, the conductance is lower at lower energies, increasing non monotonously with energy for both setups, irrespective of the angle. For $\theta = 0°$, we recover AB-stacked bilayer graphene where this general trend has previously been observed [231]. This behavior occurs even if the scattering region is replaced by graphene itself, in which case it is totally determined by the increasing number of channels in the leads.

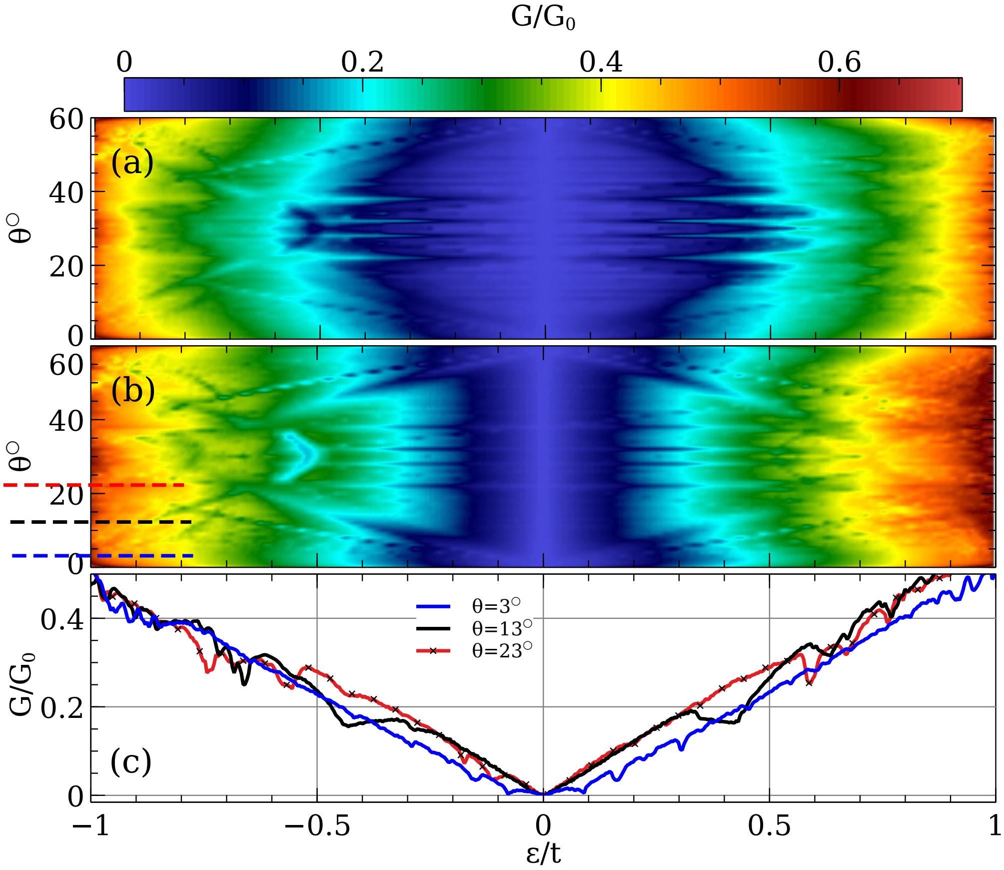

Figure 4.2: Density plot of the conductance, G, as a function of twist angle, θ, and energy, ε, for the two setups considered in this work, $1 \to 2$ (a) and $1 \to 1$ (b). Panel (c) shows G vs ε for three particular angles, $\theta = 3°$, $13°$ and $23°$, depicted as dashed horizontal lines in panel (b).

In Fig. 4.2(c) the conductance of the $1 \to 1$ setup is shown as a function of energy for three representative twist angles [corresponding to the three horizontal dashed lines in Fig. 4.2(b)]. Appart from the general trend of increasing conductance with increasing energy, characteristic features of tBLG for small, intermediate, and large angles can be appreciated. For small angles, the conductance is suppressed in a wider energy region around $\varepsilon = 0$ when compared with the other two angles. This low energy behavior is associated with the flatband regime in tBLG, and will be further discussed below. Intermediate and large twist angles have similar $G(\varepsilon)$ at low energies. As will be shown below, at higher energies the intermediate angle case first deviates from the large angle behavior at the characteristic energy of the van-Hove singularities in tBLG. In the large angle regime, particular features of tBLG are better appreciated as a function of twist angle. A series of peaks and deeps can be seen in Figs. 4.2(a) and 4.2(b). As will be discussed below, these features appear at commensurate twist angles.

4.4.2 Large twisting angles

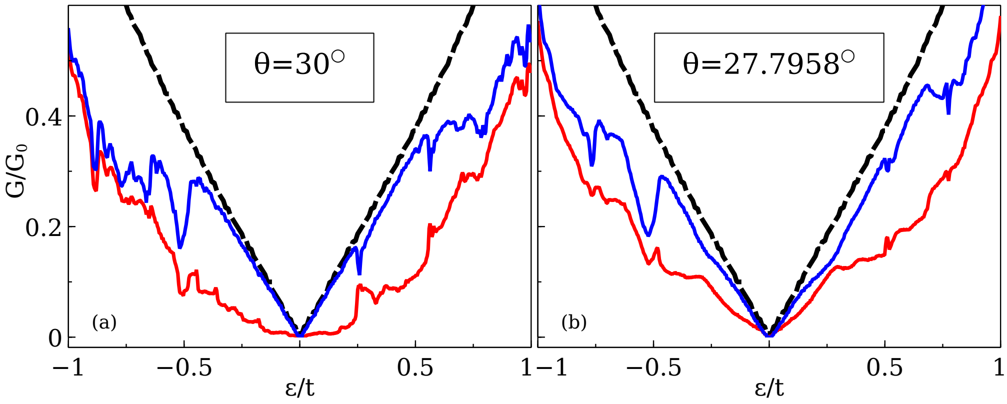

Figure 4.3: Conductance, G, as a function of energy, ε, for the $1 \to 1$ (blue) and $1 \to 2$ (red) setups computed at two large angles: an incommensurate structure with twist angle $\theta = 30°$ (a) and a commensurate strucutre with $\theta = 27.7958°$ (b). The black dashed curve is the conductance of graphene.

For large, incommensurate twist angles and low energies ($\varepsilon \ll t$), the two layers become effectively decoupled: the conductance of the $1 \to 1$ setup approaches that of monolayer graphene, while for the $1 \to 2$ setup it is strongly suppressed as the electrons need to tunnel to the other layer to conduct. This can be seen in particular for $\theta = 30°$ in Fig. 4.3(a), where we also show the graphene conductance as a dashed line for comparison. The low energy decoupling of large angle tBLG has also been obtained with the Kubo formalism within the linear response regime in Ref. [223]. However, at higher energies, deviations from the single layer conductance for the $1 \to 1$ setup and an increasing conductance for the $1 \to 2$ setup can be seen in Fig. 4.3(a). This indicates that there is always some remnant coupling even for the largest angles, in agreement with the observations of Ref. [232].

The $\theta = 30°$ tBLG considered above is an example of an incommensurate structure where no true Bravais lattice can be identified, despite the presence of the Moiré period. In particular, for the twist angle $\theta = 30°$, tBLG has been identified as a new type of quasicrystalline lattice with 12-fold rotational symmetry [233, 234]. For commensurate large angles, however, the conductance of tBLG behaves differently. This can be seen by directly inspecting Fig. 4.3(b), where we show the conductance $G(\varepsilon)$ for a commensurate angle close to $\theta = 30°$. For the $1 \to 1$ setup, $G(\varepsilon)$ starts to deviate from single layer graphene at lower energies, and for the $1 \to 2$ setup, the low energy conductance is not suppressed as for incommensurate angles.

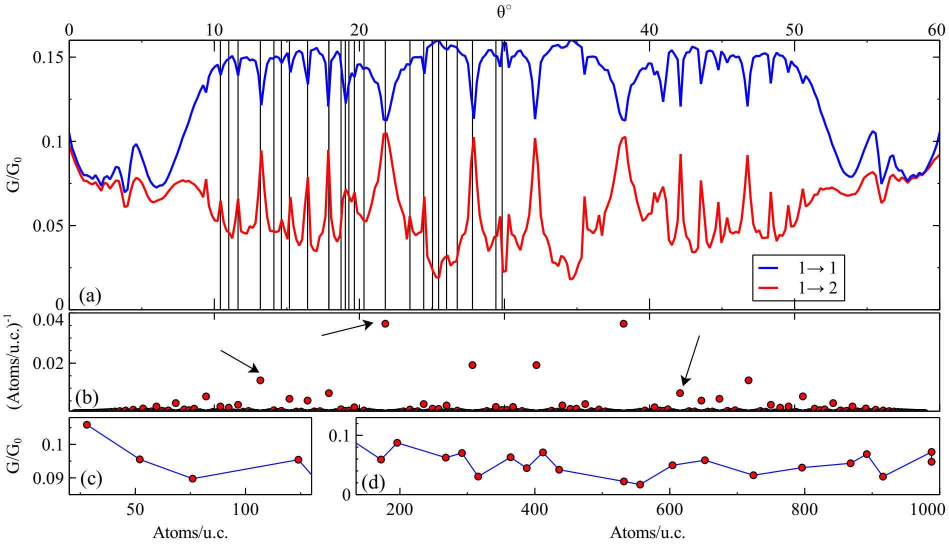

Figure 4.4: Conductance, G, as a function of twist angle, θ, for the $1 \to 1$ (blue) and $1 \to 2$ (red) setups calculated at the energy $\varepsilon = 0.225t$ (a). The black grey vertical lines depict the position of commensurate angles, as given by Eq. (4.5) in the main text. Panel (b) exhibits the inverse of the size of the Wigner-Seitz unit cell for commensurate structures versus the angle. Panel (c-d) show the conductance values of the $1 \to 2$ setup for commensurate structures as a function of size of the Wigner-Seitz unit cell for small and large unit cells respectively.

The difference between incommensurate and commensurate structures at large twist angles is better appreciated in Fig. 4.4(a), where we plot the conductance as a function of twist angle at the fixed energy $\varepsilon = 0.225t$ (easily reached via back gate field effect). For the $1 \to 1$ setup a series of deaps and for the $1 \to 2$ setup a series of peaks are clearly seen. These are the same peaks and deeps observed in Figs. 4.2(a) and 4.2(b). As shown in Fig. 4.4(a), the peaks/deeps match perfectly the vertical lines. It is also apparent that the conductance curves are symmetric with respect to the twist angle $\theta = 30°$, and for that reason we only plot vertical lines for $\theta < 30°$. The vertical lines correspond to a series of commensurate angles, obtained according to the relation

$$\sin\left(\frac{\theta_{mr}}{2}\right) = \frac{r}{2\sqrt{3m^2+3mr+r^2}}\,, \tag{4.5}$$

where m and r are positive coprime numbers [57]. Therefore, the peaks/deeps are conductance signatures of commensurability. A few of the largest peaks for the $1 \to 2$ setup have been reported also in the incoherent regime [235]. In the ballistic regime we see that the structure is very rich, with peaks at many commensurate angles. In fact, we are lead to speculate that peaks (deeps) may be present at every commensurate angle, though its relative height (depth) may hinder the observation of most of them. This is corroborated by an apparent correlation between the height (depth) of the peak (deep) and the size of the Wigner-Seitz unit cell for the corresponding commensurate lattice structure, as shown in Fig. 4.4(b). There, the inverse of the size of the Wigner-Seitz unit cell, measured in terms of the number of atoms inside the cell, is plotted as a function of the respective commensurate angle. By inspection it can be seen that the higher the conductance peak in Fig. 4.4(a) for the $1 \to 2$ setup (the lower the deep for the $1 \to 1$ setup) the smaller the respective Wigner-Seitz unit cell. The six peaks reported in Ref. [235] for the incoherent regime correspond precisely to the six twist angles with smallest Wigner-Seitz unit cell (higher conductance).

The conductance as a function of the size of the Wigner-Seitz unit cell for commensurate structures is shown in Fig. 4.4(c). In the large angle regime (unit cell sizes $\lesssim 100$), it is clear that the conductance decreases as the size of the cell increases. For intermediate to low angles (unit cell sizes $\gtrsim 100$), this commensurability effect is lost. This agrees with the fact that $r = 1$ structures, for which the unit cell coincides with the Moiré cell, are special in the small-angle limit and determine the physics of all types of commensurate structures [57]. For very small angles, all commensurate structures are almost periodic repetitions of structures with $r = 1$.

In order to better understand the large angle commensurability effect, we have computed the interlayer local current measured from the bottom layer to the top layer in the $1 \to 2$ setup. To that purpose, the bond current operator between a bottom layer site and a top layer site was evaluated at the energy $\varepsilon = 0.225t$. All the contributions that connect to a given site in the bottom layer were then added up and the obtained local interlayer current was assigned to that bottom layer site. The corresponding map is shown in Figs. 4.5(a-c) for three different commensurate angles [marked with an arrow in Fig. 4.4(b)]. Positive and negative values mean interlayer current flowing in and out of the given bottom layer site. The presence of a periodic pattern is apparent for the three angles, as can be seen in Figs. 4.5(a-c). We took the Fourier transform of the interlayer current by considering a rhombus with 50×50 unit cells in the scattering region. The corresponding map is shown in Figs. 4.5(d-f), respectively for the three angles considered. The Fourier transform is extremely peaked, as inferred from the very small dark dots on a whitish background in Figs. 4.5(d-f). The peaks exactly fall onto the first star of reciprocal lattice vectors

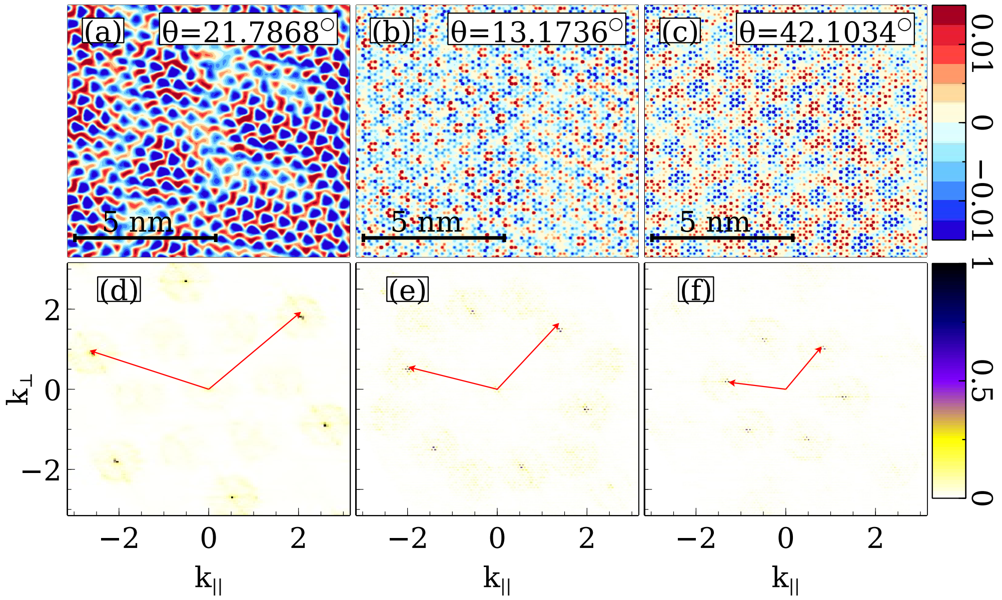

Figure 4.5: (a-c) Interlayer current mapped onto the bottom layer as a density plot at $\varepsilon = 0.225t$ for three commensurate structures. (d-f) 2D Fourier transform of the interlayer current shown in (a-c) as a function of $k_{||}$ and $k_{\perp}$, respectively the longitudinal and transverse momenta relative to the direction of the bottom lead ribbon. The arrows are two representative vectors of the first star of reciprocal lattice vectors for the respective commensurate structure.

for the respective commensurate structure. Two representative vectors out of the six in the first star are indicated in each panel of Fig. 4.5(d-f). These vectors coincide with the primitive vectors of the superlattice. The primitive vectors of the superlattice are given in Ref. [57] as,

- if $\gcd(r, 3) = 1$

$$\begin{bmatrix} \mathbf{u_1} \\ \mathbf{u_2} \end{bmatrix} = \begin{bmatrix} m & m+r \\ -m-r & 2m+r \end{bmatrix} \begin{bmatrix} \mathbf{a_1} \\ \mathbf{a_2} \end{bmatrix} \tag{4.6}$$

- if $\gcd(r, 3) = 3$

$$\begin{bmatrix} \mathbf{u_1} \\ \mathbf{u_2} \end{bmatrix} = \begin{bmatrix} m+\frac{r}{3} & m+\frac{r}{3} \\ -\frac{r}{3} & m+\frac{2r}{3} \end{bmatrix} \begin{bmatrix} \mathbf{a_1} \\ \mathbf{a_2} \end{bmatrix} \tag{4.7}$$

where gcd is the greatest common divisor of r and m. It follows that the observed periodicity for the interlayer current in Figs. 4.5(a-c) mimics the periodicity of the commensurate structure. The picture that emerges is that each Wigner-Seitz unit cell contributes roughly the same to the interlayer current, so that a higher conductance is obtained for a higher number of Wigner-Seitz unit cells in he scattering region. Keeping the number of atoms in the scattering region roughly the same, commensurate angles with smaller Wigner-Seitz unit cells should have higher conductance, as observed.

4.4.3 Moderate twisting angles

Figure 4.6(a) and 4.6(b) shows the conductance at three representative angles in the moderate twist angle regime, respectively for the 1 → 1 and 1 → 2 setups and energies $|\varepsilon| < 0.4t$. A salient feature in this regime is the shoulder like behavior of the conductance around two particular energies roughly symmetric around zero. The behavior is more pronounced in the 1 → 1 setup [Fig. 4.6(a)] which has a higher conductance, but it is clearly present in both setups. The energy scale associated with this feature correlates with the position of the two Van Hove singularities characteristic of tBLG at moderate twist angles. This is clearly seen with the help of Fig. 4.6(c), where the DOS of the system (scattering region) is shown for the three considered twist angles. The beginning of the shoulder-like feature just signals the strong suppression of the DOS after the Van Hove singularity. A similar effect is known to happen in single layer graphene after the Van Hove singularity [231], though at much higher energies.

The presence of Van Hove singularities in the DOS of tBLG for the moderate twist angle regime originates from saddle points in the energy dispersion. These saddle points are easily understood as a consequence of the hybridization between single layer Dirac cones [34, 57]. Due to rotation by the twist angle θ, and considering for the moment uncoupled layers with $t_\perp = 0$, the single layer Dirac cones appear separated in reciprocal space by a distance $\Delta K = 2K\sin\left(\frac{\theta}{2}\right)$, with $K = 4\pi/3\sqrt{3}a$. Turning on the interlayer coupling $t_\perp$, an avoided crossing at the energy scale $\varepsilon = \pm\hbar v_f \Delta K/2$ gives rise to saddle points at the approximate energies

$$\varepsilon_{vh} \approx \pm\left(\hbar v_f \frac{\Delta K}{2} - \frac{t_\perp}{2}\right). \tag{4.8}$$

In Fig. 4.6 the vertical dashed lines are obtained through Eq. (4.8) for the three twist angles considered. The beginning of the shoulder-like feature in the conductance as we increase energy is very well captured by the energy scale ε_{vh}, as can be seen in Figs. 4.6(a-b).

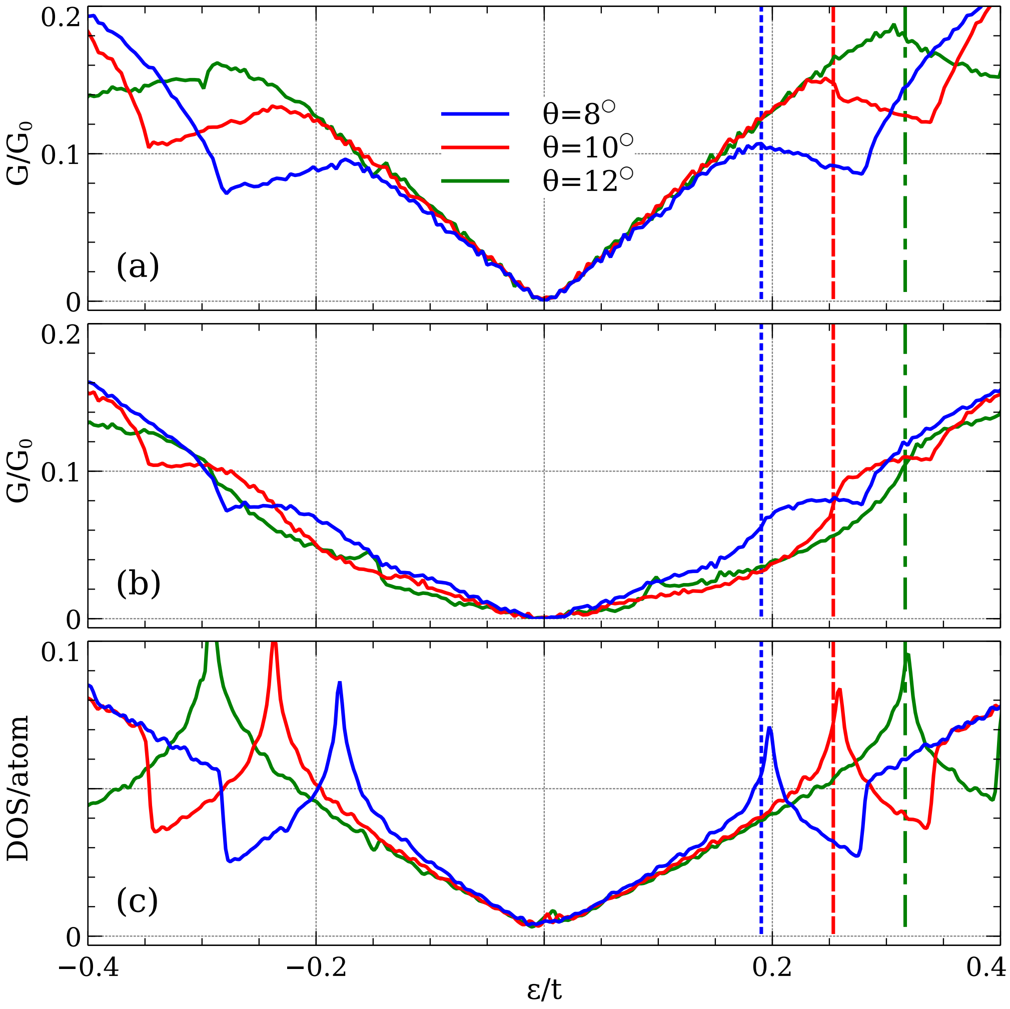

Figure 4.6: Conductance, G, as a function of energy, ε, at three twist angles $\theta = 8, 10, 12°$, for the $1 \rightarrow 1$ (a) and $1 \rightarrow 2$ (b) setups. The corresponding DOS is shown in (c). Vertical dashed lines depict the positions of Van Hove singularities computed through the approximate analytical expression given in Eq. (4.8) for the positive energy side.

4.4.4 Small twisting angles

It is in the small angle regime that most of the interesting novel phases have been found [135, 134, 198, 199, 200, 201, 202, 203, 204, 205, 206, 207, 208, 209], associated to the presence of extremely narrow bands at low energies. Given the importance of transport measurements in accessing these phases, and the fact that the model we use here is considered a proper single particle description of tBLG, we address the question of what are the conductance characteristics for this model at low twist angles. The first result is that in the small angle regime $1 \to 1$ and $1 \to 2$ setups have very similar conductance at low energies. This is an indication that in this regime the scattering region is dominated by tBLG low energy properties, which weakens the differences between the two setups. This is to be expected whenever the scattering region is big enough to include a considerable number of Moiré cells, as is the case for the angles we consider. In the following we show results only for the $1 \to 1$ setup.

We start with incommensurate angles. In Fig. 4.7(a1-a3) the conductance at three representative small twist angles around de flat band regime is shown for energies $|\varepsilon| \lesssim 0.04t$. For the model considered in this work, the flat band regime occurs at $\theta^* \approx 1.6^\circ$, so that in Fig. 4.7(a1) the conductance if for an angle slightly below θ^*, in Fig. 4.7(a2) very close to θ^*, and in 4.7(a3) slightly above. To confirm that the scattering region is indeed displaying tBLG behavior around the flat band regime we have calculated the DOS using the Kwant package [52]. This is shown in Fig. 4.7(b1-b3) at exactly the same angles (blue curves). The peaked DOS around zero energy, particularly for $\theta \approx \theta^*$, is a signature of tBLG behavior. Further confirmation comes from the DOS obtained with the plane wave expansion method [72], suitable for incommensurate structures [133, 236]. The results are also shown in Fig. 4.7(b1-b3) as red curves, along with the result obtained through the Kwant package (blue curves). The agreement is remarkable despite the fact that Kwant is a construction in real space using kernel polynomial methods while the plane wave expansion method works in reciprocal space. The plane wave expansion method allows also for the calculation of the band structure, which is displayed in Fig. 4.7(c1-c3). There, the appearance of very narrow bands at low energies, which become especially flat near θ^*, is apparent.

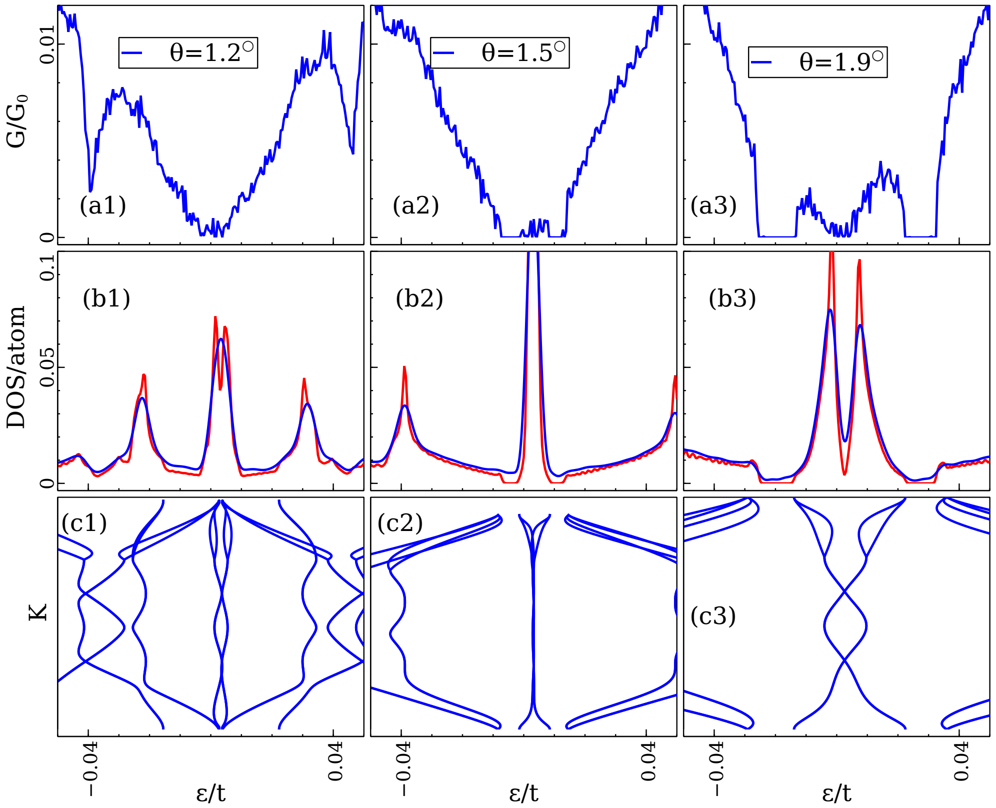

Figure 4.7: (a1-a3) Conductance, G, as a function of energy, ε, at three incommensurate twist angles around the first *magic angle* $\theta^* \approx 1.6°$ for the $1 \rightarrow 1$ setup. (b1-b3) DOS of the scattering region used in (a1-a3) is represented in blue. The DOS obtained using the plane wave expansion method is shown in red. (c1-c3) Band structure obtained by the plane wave expansion method.

The conductance in Figs. 4.7(a2) and 4.7(a3) has a low energy behavior which is not found at intermediate or large twist angles, nor in single or AB-stacked bilayer graphene [231]: low energy finite conductance flanked by transport gaps where the conductance vanishes. This is perfectly seen at θ^* and when we approach θ^* from above. Comparison with DOS and band structure, respectively in Figs. 4.7(b) and 4.7(c), shows that the transport gaps correlate perfectly with spectral gaps surrounding the low energy narrow bands. These transport gaps are in perfect agreement with those obtained experimentally when the low energy narrow bands are completely occupied, for a carrier density $n = +n_{\text{S}}$, or fully empty, $n = -n_{\text{S}}$ [135, 134, 199, 200, 209, 220]. Note also the similarity between the inverted double-well-like conductance seen at low energies for $\theta \simeq 2°$ in Fig. 4.7(a3) and the measurements of Ref. [219] (compare with conductivity) and Refs. [31, 198] (compare with inverse resistance). This points to the conclusion that the observed behavior at small angles $\theta \gtrsim \theta^*$ is still captured by the single particle description. Only very close to the *magic angle* θ^* are correlation effects expected to become relevant. For angles $\theta \lesssim \theta^*$, as the one shown in Fig. 4.7(a1), the conductance still correlates well with the electronic structure. In particular, the two side peaks seen in the DOS of Fig. 4.7(b1) clearly match the beginning of a shoulder like feature in conductance as energy increases in absolute value. As can be appreciated in Fig. 4.7(c1), the low energy narrow bands are no longer well isolated from the other bands. This is the reason why there is no transport gaps in the conductance at low energy.

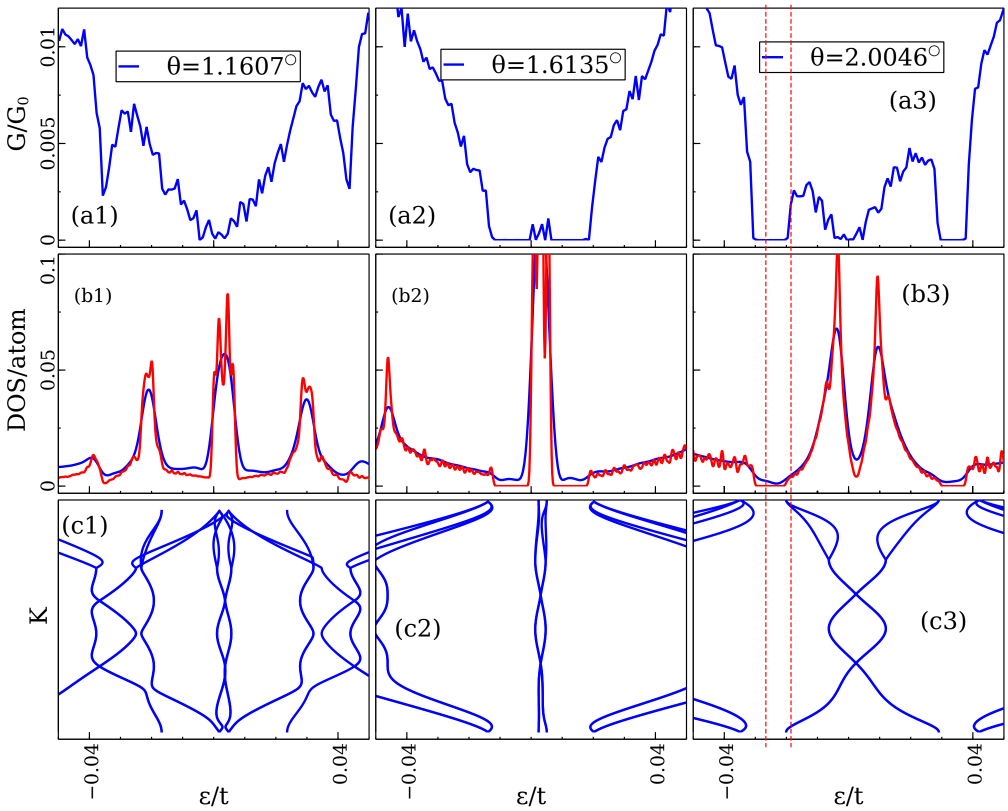

Figure 4.8: Conductance and density of states of several small commensurate angles for 1 → 1 geometry. Panel(a1-a3) exhibit the evolution of the emergent conductance gap with small twist angle. Panel(b1-b3) show the evolution of the Van Hove peaks in the density of states with angle. Panel (c1-c3) depict the corresponding band structure obtained by exact diagonalization of the periodic system. For comparison the DOS data obtained by exact diagonalization is also added as red curves. The finiteness of the DOS within the band gap obtained by Kwant is due to the boundary effects.

The results for commensurate angles are shown in Fig. 4.8. There is a close similarity with the results obtained for nearby commensurate angles, presented in Fig. 4.7. Commensurability effects, if present in the small twist angle regime, are significantly milder than at large angles. Note in particular how the transport gaps perfectly correlate with the spectrum, as is indicated by the vertical lines on the right panels of Fig. 4.8. We note *en passant* that the DOS of the scattering region, shown in blue in Fig. 4.8(b), does not vanish in the energy region where transport gaps occur [this also happens for the incommensurate angles shown in Fig. 4.7]. However, the plane wave expansion method has vanishing DOS (in red) compatible with spectral gap shown in Fig. 4.8(c). The reason is due to the open edges of the scattering region where localized states, not contributing to conductance, exist.

4.5 Chapter conclusion

We have studied the ballistic charge transport phenomena across a twisted bilayer graphene region. A strong angle dependence has been found, with three qualitatively different regimes. For large angles, there are strong commensurability effects: at large incommensurate angles the two graphene layers effectively decouple; large commensurate angles, corresponding to a small Wigner-Seitz unit cell, appear as sharp features in the conductance. For intermediate angles, we have found a correlation of the conductance features with the twist angle, which suggests that conductance measurements can be used to determine the twisting angle. For small angles we have seen that commensurate effects are washed out. However, the almost flat bands appearing in this regime give rise to distinctive conductance features. Our results agree with the recent experimental findings where transport gaps have been correlated with spectral gaps [219, 31, 135, 134, 199, 200, 209, 220, 198].

4.6 Chapter Appendices

A Building a finite-sized tBLG region

Here we explain how we construct a twisted bilayer region. The construction includes the following general steps:

1. Define the primitive vectors and positions of the basis atoms within the graphene unit cell.
2. Obtain the primitive vectors and basis atoms of the second (top) layer by applying the rotation matrix to the primitive vectors and basis atoms of the first layer.
3. Build the first layer in Kwant atom by atom, by assigning a zero onsite potential to a given lattice point.
4. While building the first layer, search for the neighbors of each atom on the second layer and create them too.

5. Assign the hopping energy to neighboring atoms according to $t_{\perp}\left(R^1 - R^2\right)$.
6. Establish the intralayer hoppings, t, in layers.
7. Cut the central region in desired shape.
8. Generate the leads and attach them to the central region

1. The primitive vectors of the first layer are,

$$\begin{aligned}
\mathbf{a_1} &= \sqrt{3}a_{cc}\left(\frac{\sqrt{3}}{2}, \frac{1}{2}\right) \\
\mathbf{a_2} &= \sqrt{3}a_{cc}\left(0, 1\right)
\end{aligned}$$

We build the first unit cell at $R = (0,0)$ by creating $A1$ and $B1$ sublattices at positions,

$$\begin{aligned}
\text{sublattice A1} &= (0,0) \\
\text{sublattice B1} &= a_{cc}\left(\frac{1}{2}, \frac{\sqrt{3}}{2}\right)
\end{aligned}$$

where a_{cc} is the C-C bond length. Leads are translational invariant along a_1. So the transverse direction is a_2.

A given unit cell labeled by (n, m) are located at

$$R^1_{mn} = \begin{cases} m\mathbf{a_1} + n\mathbf{a_2} & \text{if sublattice } A1 \\ m\mathbf{a_1} + n\mathbf{a_2} + \frac{1}{3}\left(\mathbf{a_1} + \mathbf{a_2}\right) & \text{if sublattice } B1 \end{cases}$$

in the plane (the reference atom is sublattice A). When there is no twist we have AB stacked bilayer graphene. So, at $\theta = 0$, the primitive vectors and the basis atoms of the second layer are defined as:

$$\begin{aligned}
\mathbf{a_1'} &= \mathbf{a_1} \\
\mathbf{a_2'} &= \mathbf{a_2} \\
\text{sublattice A2} &= -\text{sublattice B1} = a_{cc}\left(\frac{1}{2}, \frac{\sqrt{3}}{2}\right) \\
\text{sublattice B2} &= \text{sublattice A1} = \left(0, 0\right).
\end{aligned}$$

In tBLG the top layer is separated from the bottom layer with $d_{\perp}$. We take into account this separation when we define the interlayer hopping $t(r)$, but for the construction of the top layer we ignore it as if the two layers are in the same plane.

We set the C-C bond length to be $a_{cc} = \frac{1}{\sqrt{3}}$. While the first layer is fixed the second layer is rotated around the origin where $A1$ and B_2 sit. For the second layer we have

$$\begin{aligned} \mathbf{a_1'} &= \mathcal{R}(\theta) \cdot \mathbf{a_1} \\ \mathbf{a_2'} &= \mathcal{R}(\theta) \cdot \mathbf{a_2} \\ \text{sublattice A2} &= \mathcal{R}(\theta) \cdot \left(-\frac{a_{cc}}{2}, -\frac{a_{cc}\sqrt{3}}{2} \right) \\ \text{sublattice B2} &= (0,0) \end{aligned}$$

With these, we build the first layer by running m and n in R^1_{mn} from $-M$ to M and $-N$ to N respectively. For a given unit cell, labeled by R^1_{mn}, on the bottom layer we search for neighbors on the top layer at the on fly when we build the cell. This takes place with the following prescription: Assuming that we are looking for the neighbors of an atom within a circle with radius r, the atom X is the neighbor of atom Y if and only if their in-plane separation is less than r

$$|R_X - R_Y| < r \tag{4.9}$$

For a fixed R_X on the bottom layer, running R_Y on the second layer, the latter inequality determines the neighbors of atom X. Here we employ slightly different method for spatial search. We first solve the following equation, for a given R_X in first layer, in order to get p and q,

$$R_X = p\mathbf{a_1'} + q\mathbf{a_2'} \tag{4.10}$$

Obviously, p and q in general are not integers as R_X is not the lattice vector of the top layer. We round p and q to the closest integer. This in principle gives the m' and $n'$of the nearest cell in the top layer to the atom at R_X.

$$\begin{aligned} m' &= round\,(p) \\ n' &= round\,(q) \end{aligned}$$

$$R_Y^{nearest} = m'\mathbf{a_1'} + n'\mathbf{a_2'} \tag{4.11}$$

After finding the nearest neighbor cell in the second layer, we search all those cells which are neighbors of $R_Y^{nearest}$. This is done by running the following iteration,

$$R_Y^{i,j} = (m' + i)\,\mathbf{a_1'} + (n' + j)\,\mathbf{a_2'}, \quad i, j \in \{-1, 0, 1\}$$

This gives the first six neighbor unit cells of atom X. One could also look for next-next neighbors by using $i, j \in \{-2, -1, 0, 1, 2\}$ depending on the value of r. Since we set $r = 0.9a_{cc}$, the first six neighbors are enough to search within. An example of Python code to generate a circular tBLG region is given Appendix 4.6

B Python codes

In this Appendix, an example of Python (version 3.6) code to build a circular tBLG region is presented.

```
import kwant
import numpy as np
import tinyarray as ta

def Building(L=1, W=1, theta=0, lead=11, acc=1.42, dperp=3.35,
   t=2.79,tp=0.35, hp_range=0.9, E_in_units_of_t=True,
   acc_in_units_of_a=True, xshift=0, yshift=0):
# This function builds a tBLG with an arbitrary twist angle in
   circular shape and attaches the leads to it.
    size = np.array([L, W, theta])
    primitive_vector1 = np.sqrt(3)*acc*np.array([np.sqrt(3)/2,
       1/2]) # The first layer’s unit vector
    primitive_vector2 = np.sqrt(3)*acc*np.array([0, 1]) # The
       second layer’s unit vector
    Atom1 = ta.array([0, 0]) # Atom A in the first layer’s unit
        cell
    Atom2 = ta.array([acc/2, acc*np.sqrt(3)/2]) # Atom B in the
        first layer’s unit cell
    Atom4 = ta.array([0, 0]) +xshift*primitive_vector1+ yshift*
       primitive_vector2 # Atom A’ in the second layer’s unit
       cell
    Atom3 = ta.array([-acc/2, -acc*np.sqrt(3)/2]) +xshift*
       primitive_vector1+ yshift*primitive_vector2 # Atom B’ in
        the second layer’s unit cell

    layer1 = kwant.lattice.general([primitive_vector1,
       primitive_vector2], [Atom1, Atom2], name = ’firstlayer’,
```

```
      norbs = 1) # Set the first layer hoeycomb lattice
     parameters
    a1, b1 = layer1.sublattices
    TBL = kwant.Builder() # Kwant builder

    theta = theta/180*np.pi # Twist angle
    c = np.cos(theta)
    s = np.sin(theta)
    rotation_matrix = ta.array([[c, -s], [s, c]]) # Rotation
        matrix
    rotated_Atom3 = ta.dot(rotation_matrix, Atom3) # Rotate
        atom 3
    rotated_Atom4 = ta.dot(rotation_matrix, Atom4) # Rotate
        atom 4
    rotated_primitive_vector1 = ta.dot(rotation_matrix,
        primitive_vector1) # Rotate a1 in the top layer
    rotated_primitive_vector2 = ta.dot(rotation_matrix,
        primitive_vector2) # Rotate a2 in the top layer
    layer2 = kwant.lattice.general([rotated_primitive_vector1,
        rotated_primitive_vector2],  [rotated_Atom3,
        rotated_Atom4], name = 'secondlayer', norbs = 1) # Set
        the rotated second layer hoeycomb lattice parameters.

    a2, b2 = layer2.sublattices # Build the second layer
        lattice based
    Mat = ta.matrix([[rotated_primitive_vector1[0],
        rotated_primitive_vector2[0]], [
        rotated_primitive_vector1[1], rotated_primitive_vector2
        [1]]])
    invMat = np.linalg.inv(Mat)
    def distance(m, n, sub1, k, l, sub2): # Determines the
        distance between two atoms in different layers
         r1x = m*primitive_vector1[0] + n*primitive_vector2[0] +
              sub1*Atom2[0]
         r1y = m*primitive_vector1[1] + n*primitive_vector2[1] +
              sub1*Atom2[1]
         r2x = k*rotated_primitive_vector1[0] + (1-sub2)*
             rotated_Atom3[0] + \
         l*rotated_primitive_vector2[0]
         r2y = k*rotated_primitive_vector1[1] + (1-sub2)*
             rotated_Atom3[1] + \
         l*rotated_primitive_vector2[1]
         r12 = np.sqrt((r2x-r1x)**2 + (r2y-r1y)**2)

         return r12

    def tperp(r = 0, acc = acc, dperp = dperp, t = t, tp = tp):
         # Spatialy modulated interlayer hopping
```

```
        qsigma = 7.42
        qpi = 3.15
        rp = np.sqrt(r**2 + dperp**2)
        sin2omega =  r**2/(dperp**2 + r**2)
        cos2omega = dperp**2/(dperp**2 + r**2)
        VPPsigma = tp*np.exp(qsigma*(1-rp/dperp))
        VPPpi = -t*np.exp(qpi*(1-rp/acc))
        ttp = VPPsigma*cos2omega + VPPpi*sin2omega

        return ttp

    cutoff = tperp(r = hp_range*acc) # Determine the cutoff
       tperp below which all interlayer hoppings set to be zero
       .

    def mapp(m, n): # Finds possible hoppingd from the first to
        the second layer

        posx = m*primitive_vector1[0] + n*primitive_vector2[0]
        posy = m*primitive_vector1[1] + n*primitive_vector2[1]
        m2 = np.round(invMat[0, 0]*(posx+rotated_Atom3[0]) +
           invMat[0, 1]*(posy+rotated_Atom3[1]))
        n2 = np.round(invMat[1, 0]*(posx+rotated_Atom3[0]) +
           invMat[1, 1]*(posy+rotated_Atom3[1]))

        def hopp(m, n, m22, n22): # Interlayer hopping values
           between two cells in different layers

            hopa1a2 = np.round(tperp(r = distance(m, n, 0, m22,
                n22, 0)), decimals=5)
            hopa1b2 = np.round(tperp(r = distance(m, n, 0, m22,
                n22, 1)), decimals=5)
            hopb1a2 = np.round(tperp(r = distance(m, n, 1, m22,
                n22, 0)), decimals=5)
            hopb1b2 = np.round(tperp(r = distance(m, n, 1, m22,
                n22, 1)), decimals=5)

            return hopa1a2, hopa1b2, hopb1a2, hopb1b2

        sites = []

        if hp_range >= 1.5:
            watched_cells =  range(-5, 6) # Define the range of
                cells which need to be searched for neighbors.
        elif (hp_range > 0 and hp_range < 1.5):
            watched_cells =  range(-2, 3)
        else:
            ValueError('hp_range␣must␣be␣a␣non-negative␣number'
               )
```

```
    for i in watched_cells:
        for j in watched_cells:
            hopa1a2, hopa1b2, hopb1a2, hopb1b2 = hopp(m, n,
                m2 + i, n2 + j)
            sites.append([m, n, m2 + i, n2 + j, hopa1a2,
               hopa1b2, hopb1a2, hopb1b2])

    return sites, watched_cells

dim1 = [i for i in range(-L, L + 1)]
dim2 = [i for i in range(-W, W + 1)]
m, n = np.meshgrid(dim1, dim2, indexing = 'ij')
mass, watched_cells = mapp(m, n)

for i in range(-L, L+1):
    for j in range(-L, L+1):
        TBL[[a1(i, j), b1(i, j), a2(i, j), b2(i, j)]] = 0

for k in range(len(watched_cells)**2):
    mas = mass[k]
    for i in range(2*L + 1):
        for j in range(2*W + 1):

            x1, y1 = mas[0][i, j], mas[1][i, j]
            x2, y2 = int(mas[2][i, j]), int(mas[3][i, j])
            hopa1a2, hopa1b2 = mas[4][i, j], mas[5][i, j]
            hopb1a2, hopb1b2 = mas[6][i, j], mas[7][i, j]
            TBL[[a1(x1, y1), b1(x1, y1), a2(x2, y2), b2(x2,
                y2)]] = 0 # Generate sites

            if hopa1a2>cutoff:
                TBL[(a1(x1, y1), a2(x2, y2))] = -hopa1a2
            if hopa1b2>cutoff:
                TBL[(a1(x1, y1), b2(x2, y2))] = -hopa1b2
            if hopb1a2>cutoff:
                TBL[(b1(x1, y1), a2(x2, y2))] = -hopb1a2
            if hopb1b2>cutoff:
                TBL[(b1(x1, y1), b2(x2, y2))] = -hopb1b2

TBL[layer1.neighbors(1)] = -t # Assignement of interalyer
    nearest neighbor hoppings in the first layer.
TBL[layer2.neighbors(1)] = -t # Assignement of interalyer
    nearest neighbor hoppings in the second layer.


def in_hole(site): # Generates a disk region
    x, y = site.pos # position relative to centre
```

```
        center=xshift*primitive_vector1+ yshift*primitive_vector2
        aa = np.sqrt((x-center[0])**2 + (y-center[0])**2)>np.sqrt(3)/2*(L+2 )
        return  aa
#
    for site in filter(in_hole ,  list(TBL.sites())): # Delete atoms out of disk
        del TBL[site]
    TBL.eradicate_dangling()  # Delete all dangling atoms

    sym0 = kwant.TranslationalSymmetry(layer1.vec((-1, 0))) # Define the translational invariance along a a_{1} direction
    left_lead = kwant.Builder(sym0) # Generate the left lead along the translationally invariant direction.
    sym1 = kwant.TranslationalSymmetry(layer2.vec((1, 0)))
    right_lead = kwant.Builder(sym1)


    for x in range(0,3): # Specify atoms and hoppings in the leads
        for y in range(-L, L+1):
            left_lead[a1(x, y)]=0
            left_lead[b1(x, y)]=0
            right_lead[a2(x, y)]=0
            right_lead[b2(x, y)]=0

    left_lead[layer1.neighbors()]=-t  # Set the hoppings in left lead.
    right_lead[layer2.neighbors()]=-t # Set the hoppings in right lead.

    if lead==11:  # Attach both leads to the frist layer.
        TBL.attach_lead(left_lead )
        TBL.attach_lead(left_lead.reversed() )
        syst=TBL
        syst=TBL.finalized()
    elif lead==12:  # Attach both leads to the second layer.
        TBL.attach_lead(left_lead )
        TBL.attach_lead(right_lead)
        syst=TBL
        syst=TBL.finalized()
    elif lead==None:  # No leads are attached.
        syst=TBL

    else:
        raise NameError('Unknown␣type␣of␣lead␣connections.␣\
```

```
␣␣␣␣␣␣␣␣␣␣␣␣␣␣␣␣␣␣␣␣␣␣␣Please,␣choose␣1␣to␣1␣or␣1␣to␣2␣
    connextions')

    return syst, size, lead, [a1, b1, a2, b2],
        primitive_vector1, primitive_vector2

L=10 # set the width of the ribbon
W=10 # set the length of the ribbon
theta=30 # set the rotation angle
theta = theta/180*np.pi
hp_range= 1.0 # Set the interlayer hopping range (in units of
    lattice paramter.)

syst, size, lead, sitefam, pv1, pv2=Building(L=L, W=L, theta =
    theta, hp_range=hp_range, lead=None, xshift=0, yshift=0) #
    Build the system
a1, b1, a2, b2 = sitefam
kwant.plot(syst, site_size=0.2, site_color='black', hop_color='
    blue', hop_lw=0.1, file='theta'+str([theta, 11])+'.svg', dpi
    =200, fig_size=(3,3)) # Plot the system and save it in png
    format.
```

5 Concluding remarks

In this thesis, we theoretically investigated the transport properties of monolayer-bilayer-monolayer (MBM) hybrid structure in 1D, chain-ladder-chain, and in 2D, graphene-bilayer-graphene, using semi-analytical transfer matrix method and purely numerical method based on Kwant Python package. Electrons on 1D chain and honeycomb lattice are modeled using the single particle tight-binding Hamiltonian in order to get the electronic structure as well as charge transport properties in the the MBM systems. We first looked at the transport in the toy model of chain-ladder-chain where we established and employed transfer matrix formalism. We mainly concentrated on exploring the transmission through a bilayer graphene region for the case of Bernal stacked and twisted bilayer graphene.

In chapter 3, we introduced the MBM hybrid structure as a naturally arising sample in few layer graphene synthesis. The chain-ladder-chain structure as an instant example of an MBM structure in 1D is explored as a useful and simple toy model. The transfer matrix technique is used to yield the transmission and reflection coefficients. Using the celebrated Landauer-Buttiker formula we have studied the conductance across a graphene bilayer region for two different positions of the single layer leads: the case when the leads connect to the same layer, the $1 \rightarrow 1$ configuration; and the case when the leads connect to different layers, $1 \rightarrow 2$ configuration. We have worked in the limit of an infinitely wide scattering region, to avoid edge effects, and developed a transfer matrix, tight-binding based methodology which allows going away from linear response. We have also studied the effect of a gate bias with a multiple domain wall microstructure applied to the bilayer region. We have found that,

- when there is no gate bias applied to the bilayer region, the two setups, $1 \rightarrow 1$ and $1 \rightarrow 2$, have a similar behavior, with a slightly higher conductance in the $1 \rightarrow 1$ configuration.
- The presence of a bias gate voltage differentiates between the two configurations. Both of them develop a conductance gap which mimics the spectral gap of a biased bilayer, but only the $1 \rightarrow 1$ configuration shows a pronounced conductance step at one of the gap edges. This step is not present if the gate polarity is reversed.
- Introducing a domain wall in the gate bias applied to the bilayer region, the conductance step disappears and the two configurations, $1 \rightarrow 1$ and $1 \rightarrow 2$, behave again in a similar way.

- When the separation between domains is much larger than the localization length of the states confined at the domain walls, the multiple domain walls states behave independently and the result is similar to the case of a single domain wall.
- On decreasing the separation between domain walls, the localized states start to hybridize and a finite conductance starts to appear inside the gap. At even smaller distances, the gap is completely washed out, and only at higher energies a conductance asymmetry characteristic of a gate biased bilayer region is present.
- We have studied the viability of an integrated nano-transistor based on the $1 \to 1$ or $1 \to 2$ geometries. For experimentally reasonable chemical potential difference ($\sim 0.3\,\mathrm{eV}$) and gate voltage interval (from 0 up to $\sim 0.6\,\mathrm{eV}$) we have found that this setup can achieve $50 \lesssim I_{\mathrm{on}}/I_{\mathrm{off}} \lesssim 200$. Summing up all the finds, it is clear the transmission through a bilayer region can be manipulated by a gate bias in ways not previously anticipated.

In chapter 4, we explored the transmission through a twisted bilayer region. In order to keep the number of atoms almost constant at each rotation we shape the bilayer region in a disk form. We compute the conductance and density of states using a Kwant Python package. For small twist angles we also computed the band structure of the twisted bilayer graphene using wave expansion technique. We found that,

- There is a strong angle dependence with three qualitatively different regimes. Large, intermediate, and small angles.
- For large angles, in general, there are strong commensurability effects.
  - At large incommensurate angles, the two graphene layers effectively decouple.
  - At large commensurate angles, corresponding to a small unit cell, appear as sharp features in the conductance.
- For intermediate angles, there is a correlation of the conductance features with the twist angle, which suggests that conductance measurements can be used to determine the twisting angle.
- For small twisting angles the commensurate effects are washed out and the conductance becomes a smooth function of the angle. Conductance can be used to probe the almost flat bands appearing in this regime.
- Our results agree with the recent experimental findings where zero conductance regions have been correlated with gaps in the density of states.

Regarding the transport in graphene based hybrid structures, interesting phenomena can still be explored. It would be interesting to look at the transport in flat band regime in detail and for both commensurate and incommensurate angle structures. Though twisted bilayer graphene do not develop band gap, unlike its Bernal stacked form, it would still be interesting to study how transport respond to a gate voltage. From computational point of view, the computation complexities, both in time and memory, change with system size and highly paralleled computation seems to be necessary. It would be of great interest to implement transport calculations in graphic card bases parallel computing platforms, like CUDA, as they provide a powerful tool to achieve highly parallelized computer codes for faster calculations.

Coming back to the primary question of chapter 2, “What is so special about graphene?”, graphene has attracted significant attention of scientists both from fundamental science and applied research perspectives. Its unique electronic properties are mainly related to its peculiar band structure and linear dispersion near its Fermi surface. It has also been considered as a promising candidate for the post-silicon age. Graphene on its stacked form as Bernal and twist bilayers has shown striking properties, such as developing a controllable band gap and showing superconducting behavior. It has immense potential in the electronic device application, for instance, field-effect transistor, transparent electrode, etc.

At the end, uncovering the mysteries of 2D material not only can deepen our theoretical understanding of quantum world in similar confined systems but also can help us to control the properties of materials at nanoscale which eventually might end up in new physics and new nanodevices.

Bibliography

[1] N. D. Mermin, Physical Review **176**, 250 (1968).

[2] J. C. Slonczewski and P. R. Weiss, Physical Review **109**, 272 (1958).

[3] G. W. Semenoff, Physical Review Letters **53**, 2449 (1984).

[4] Y. Zhang, Y.-W. Tan, H. L. Stormer, and P. Kim, Nature **438**, 201 (2005).

[5] J. C. Meyer, A. K. Geim, M. I. Katsnelson, K. S. Novoselov, T. J. Booth, and S. Roth, Nature **446**, 60 (2007).

[6] M. S. Dresselhaus and G. Dresselhaus, Advances in Physics **51**, 1 (2002).

[7] O. A. Shenderova, V. V. Zhirnov, and D. W. Brenner, Critical Reviews in Solid State and Materials Sciences **27**, 227 (2002).

[8] K. S. Novoselov, Science **306**, 666 (2004), arXiv:0410550 [cond-mat] .

[9] A. A. Balandin, S. Ghosh, W. Bao, I. Calizo, D. Teweldebrhan, F. Miao, and C. N. Lau, Nano Letters **8**, 902 (2008).

[10] C. Lee, X. Wei, J. W. Kysar, and J. Hone, Science (New York, N.Y.) **321**, 385 (2008).

[11] S. Stankovich, D. A. Dikin, G. H. B. Dommett, K. M. Kohlhaas, E. J. Zimney, E. A. Stach, R. D. Piner, S. T. Nguyen, and R. S. Ruoff, Nature **442**, 282 (2006).

[12] D. A. Dikin, S. Stankovich, E. J. Zimney, R. D. Piner, G. H. B. Dommett, G. Evmenenko, S. T. Nguyen, and R. S. Ruoff, Nature **448**, 457 (2007).

[13] L. A. Ponomarenko, A. K. Geim, A. A. Zhukov, R. Jalil, S. V. Morozov, K. S. Novoselov, V. V. Cheianov, V. I. Fal'ko, K. Watanabe, T. Taniguchi, and R. V. Gorbachev, Nature Physics **7**, 958 (2011), arXiv:1107.0115 .

[14] L. Britnell, R. V. Gorbachev, R. Jalil, B. D. Belle, F. Schedin, A. Mishchenko, T. Georgiou, M. I. Katsnelson, L. Eaves, S. V. Morozov, N. M. R. Peres, J. Leist, A. K. Geim, K. S. Novoselov, and L. A. Ponomarenko, Science **335**, 947 (2012).

[15] S. J. Haigh, A. Gholinia, R. Jalil, S. Romani, L. Britnell, D. C. Elias, K. S. Novoselov, L. A. Ponomarenko, A. K. Geim, and R. Gorbachev, Nature Materials **11**, 764 (2012), arXiv:1206.6698 .

[16] C. Dean, A. Young, L. Wang, I. Meric, G.-H. Lee, K. Watanabe, T. Taniguchi, K. Shepard, P. Kim, and J. Hone, Solid State Communications **152**, 1275 (2012).

[17] R. V. Gorbachev, A. K. Geim, M. I. Katsnelson, K. S. Novoselov, T. Tudorovskiy, I. V. Grigorieva, A. H. MacDonald, S. V. Morozov, K. Watanabe, T. Taniguchi, and L. A. Ponomarenko, Nature Physics **8**, 896 (2012).

[18] T. Georgiou, R. Jalil, B. D. Belle, L. Britnell, R. V. Gorbachev, S. V. Morozov, Y.-J. Kim, A. Gholinia, S. J. Haigh, O. Makarovsky, L. Eaves, L. A. Ponomarenko, A. K. Geim, K. S. Novoselov, and A. Mishchenko, Nature Nanotechnology **8**, 100 (2013).

[19] A. K. Geim and I. V. Grigorieva, Nature **499**, 419 (2013).

[20] T. Ohta, A. Bostwick, T. Seyller, K. Horn, and E. Rotenberg, Science **313**, 951 (2006), arXiv:arXiv:1011.1669v3 .

[21] Y. Zhang, T. T. Tang, C. Girit, Z. Hao, M. C. Martin, A. Zettl, M. F. Crommie, Y. R. Shen, and F. Wang, Nature **459**, 820 (2009), arXiv:0802.2933 .

[22] M. F. Craciun, S. Russo, M. Yamamoto, J. B. Oostinga, A. F. Morpurgo, and S. Tarucha, Nature Nanotechnology **4**, 383 (2009).

[23] S. Y. Zhou, G.-H. Gweon, A. V. Fedorov, P. N. First, W. A. de Heer, D.-H. Lee, F. Guinea, A. H. Castro Neto, and A. Lanzara, Nature Materials **6**, 770 (2007), arXiv:0709.1706 .

[24] R. W. Havener, Y. Liang, L. Brown, L. Yang, and J. Park, Nano Letters **14**, 3353 (2014).

[25] S. K. Jain, V. Juricic, and G. T. Barkema, 2D Materials (2016), 10.1088/2053-1583/4/1/015018, arXiv:1611.01000 .

[26] S. Shallcross, S. Sharma, and O. A. Pankratov, Physical Review Letters **101**, 056803 (2008).

[27] R. de Gail, M. O. Goerbig, F. Guinea, G. Montambaux, and A. H. Castro Neto, Physical Review B **84**, 045436 (2011), arXiv:1103.3172 .

[28] R. Bistritzer and A. H. MacDonald, Physical Review B **84**, 035440 (2011).

[29] W. Yan, W.-Y. He, Z.-D. Chu, M. Liu, L. Meng, R.-F. Dou, Y. Zhang, Z. Liu, J.-C. Nie, and L. He, Nat. Commun. **4**, 2159 (2013), arXiv:1206.5881 .

[30] J. S. Alden, A. W. Tsen, P. Y. Huang, R. Hovden, L. Brown, J. Park, D. A. Muller, and P. L. McEuen, Proceedings of the National Academy of Sciences of the United States of America **110**, 11256 (2013).

[31] Y. Kim, P. Herlinger, P. Moon, M. Koshino, T. Taniguchi, K. Watanabe, and J. H. Smet, Nano Lett. **16**, 5053 (2016).

[32] J. Yin, H. Wang, H. Peng, Z. Tan, L. Liao, L. Lin, X. Sun, A. L. Koh, Y. Chen, H. Peng, and Z. Liu, Nature Communications (2016), 10.1038/ncomms10699.

[33] C.-C. Lu, Y.-C. Lin, Z. Liu, C.-H. Yeh, K. Suenaga, and P.-W. Chiu, ACS Nano **7**, 2587 (2013).

[34] J. M. B. Lopes dos Santos, N. M. R. Peres, and A. H. Castro Neto, Physical Review Letters **99**, 256802 (2007).

[35] A. O. Sboychakov, A. L. Rakhmanov, A. V. Rozhkov, and F. Nori, Physical Review B **92**, 075402 (2015).

[36] Q. Tang and Z. Zhou, Progress in Materials Science **58**, 1244 (2013).

[37] K. J. Koski and Y. Cui, ACS Nano **7**, 3739 (2013).

[38] K. S. Novoselov, D. Jiang, F. Schedin, T. J. Booth, V. V. Khotkevich, S. V. Morozov, and A. K. Geim, Proceedings of the National Academy of Sciences of the United States of America **102**, 10451 (2005).

[39] D. A. Areshkin and C. T. White, Nano Letters **7**, 3253 (2007).

[40] D. Gunlycke, D. A. Areshkin, J. Li, J. W. Mintmire, and C. T. White, Nano letters **7**, 3608 (2007).

[41] Q. Yan, B. Huang, J. Yu, F. Zheng, J. Zang, J. Wu, B.-L. Gu, F. Liu, and W. Duan, Nano Letters **7**, 1469 (2007).

[42] I. Snyman and C. W. Beenakker, Physical Review B - Condensed Matter and Materials Physics **75**, 1 (2007), arXiv:0609243 [cond-mat] .

[43] J. Nilsson, A. H. Castro Neto, F. Guinea, and N. M. R. Peres, Phys. Rev. B **76**, 165416 (2007).

[44] T. Nakanishi, M. Koshino, and T. Ando, Physical Review B - Condensed Matter and Materials Physics **82**, 125428 (2010), arXiv:1008.4450 .

[45] J. W. González, H. Santos, M. Pacheco, L. Chico, and L. Brey, Physical Review B **81**, 195406 (2010), arXiv:1002.3573 .

[46] F. Giannazzo, I. Deretzis, A. La Magna, F. Roccaforte, and R. Yakimova, Physical Review B **86**, 235422 (2012).

[47] C. J. Páez, D. A. Bahamon, and A. L. C. Pereira, Physical Review B **90**, 125426 (2014).

[48] C. J. Páez, A. L. C. Pereira, J. N. B. Rodrigues, and N. M. R. Peres, Physical Review B **92**, 045426 (2015).

[49] K.-L. Chu, Z.-B. Wang, J. Zhou, and H. Jiang, Chinese Physics B **26**, 067202 (2017).

[50] J. Zhu, Z. Zern, T. Taniguchi, K. Wang, K. Watanabe, K. J. McFaul, Y. Ren, J. Li, and Z. Qiao, Nature Nanotechnology **11**, 1060 (2016).

[51] P. R. Amestoy, I. S. Duff, J.-Y. L'Excellent, and X. S. Li, Parallel Computing **29**, 833 (2003).

[52] C. W. Groth, M. Wimmer, A. R. Akhmerov, and X. Waintal, New Journal of Physics **16**, 063065 (2014), arXiv:1309.2926 .

[53] A. K. Geim and K. S. Novoselov, Nature Materials **6**, 183 (2007), arXiv:0702595v1 [cond-mat] .

[54] A. H. Castro Neto, N. M. R. Peres, K. S. Novoselov, A. K. Geim, F. Guinea, N. M. R. Peres, K. S. Novoselov, A. K. Geim, F. Guinea, N. M. R. Peres, A. H. Castro Neto, N. M. R. Peres, K. S. Novoselov, A. K. Geim, and F. Guinea, Reviews of Modern Physics **81**, 109 (2009), arXiv:0709.1163v2 .

[55] Z. Liu, K. Suenaga, P. J. F. Harris, and S. Iijima, Physical Review Letters **102**, 015501 (2009).

[56] C. Park, J. Ryou, S. Hong, B. G. Sumpter, G. Kim, and M. Yoon, Physical Review Letters **115**, 015502 (2015), arXiv:1505.01959 .

[57] J. M. B. Lopes dos Santos, N. M. R. Peres, and A. H. Castro Neto, Physical Review B - Condensed Matter and Materials Physics **86**, 155449 (2012), arXiv:1202.1088 .

[58] R. Bistritzer and A. H. MacDonald, Proceedings of the National Academy of Sciences **108**, 12233 (2011).

[59] E. McCann and M. Koshino, Reports on Progress in Physics **76**, 056503 (2012), arXiv:1205.6953 .

[60] P. L. De Andres, R. Ramírez, and J. A. Vergés, Physical Review B - Condensed Matter and Materials Physics **77** (2008), 10.1103/PhysRevB.77.045403, arXiv:0707.4575 .

[61] Y. Shibuta and J. A. Elliott, Chemical Physics Letters **512**, 146 (2011).

[62] M. S. Alam, J. Lin, and M. Saito, Japanese Journal of Applied Physics **50**, 080213 (2011).

[63] Z. Xu, X. Li, B. I. Yakobson, and F. Ding, Nanoscale **5**, 6736 (2013).

[64] J. Berashevich and T. Chakraborty, The Journal of Physical Chemistry C **115**, 24666 (2011).

[65] E. V. Castro, K. S. Novoselov, S. V. Morozov, N. M. R. Peres, J. M. B. L. Dos Santos, J. Nilsson, F. Guinea, A. K. Geim, and A. H. C. Neto, Physical Review Letters **99**, 216802 (2007), arXiv:0611342 [cond-mat] .

[66] E. McCann, D. S. Abergel, and V. I. Fal'ko, Solid State Communications **143**, 110 (2007).

[67] S. Das Sarma, S. Adam, E. H. Hwang, and E. Rossi, Reviews of Modern Physics **83**, 407 (2011), arXiv:1003.4731 .

[68] H. Yan, Nanophotonics **4**, 115 (2015).

[69] T. Stauber, Journal of Physics: Condensed Matter **26**, 123201 (2013), arXiv:1310.4296 .

[70] M. M. Glazov and S. D. Ganichev, Physics Reports **535**, 101 (2013), arXiv:1306.2049 .

[71] E. J. Mele, Journal of Physics D: Applied Physics **45**, 154004 (2012), arXiv:1109.2008 .

[72] C. Gonçalo, B. Amorim, E. V. Castro, J. M. V. P. Lopes, and N. Peres, in *Handb. Graphene Vol. 3*, edited by M. Zhang (John Wiley & Sons, New Jersey, 2019) Chap. 6, pp. 177–230.

[73] E. McCann, Phys. Rev. B **74**, 161403(R) (2006).

[74] E. McCann and V. I. Fal'ko, Physical Review Letters **96**, 086805 (2006), arXiv:0510237 [cond-mat] .

[75] J. Nilsson, A. H. C. Neto, F. Guinea, and N. M. R. Peres, Physical Review Letters **97**, 266801 (2006), arXiv:0604106 [cond-mat] .

[76] E. V. Castro, K. S. Novoselov, S. V. Morozov, N. M. R. Peres, J. M. B. Lopes dos Santos, J. Nilsson, F. Guinea, A. K. Geim, and A. H. Castro Neto, Journal of Physics: Condensed Matter **22**, 175503 (2010), arXiv:0807.3348 .

[77] J. B. Oostinga, H. B. Heersche, X. Liu, A. F. Morpurgo, and L. M. K. Vandersypen, Nat. Mater. **7**, 151 (2008).

[78] E. A. Henriksen and J. P. Eisenstein, Physical Review B **82**, 041412 (2010), arXiv:1004.2543 .

[79] J. Nilsson, A. H. Castro Neto, F. Guinea, and N. M. R. Peres, Physical Review B - Condensed Matter and Materials Physics **76**, 165416 (2007), arXiv:0607343 [cond-mat] .

[80] M. Kuwabara, D. R. Clarke, and D. A. Smith, Applied Physics Letters **56**, 2396 (1990).

[81] Z. Y. Rong and P. Kuiper, Physical Review B **48**, 17427 (1993).

[82] J. Xhie, K. Sattler, M. Ge, and N. Venkateswaran, Physical Review B **47**, 15835 (1993).

[83] J. M. Englert, J. Röhrl, C. D. Schmidt, R. Graupner, M. Hundhausen, F. Hauke, and A. Hirsch, Advanced Materials **21**, 4265 (2009).

[84] Y. Hernandez, V. Nicolosi, M. Lotya, F. M. Blighe, Z. Sun, S. De, I. T. McGovern, B. Holland, M. Byrne, Y. K. Gun'Ko, J. J. Boland, P. Niraj, G. Duesberg, S. Krishnamurthy, R. Goodhue, J. Hutchison, V. Scardaci, A. C. Ferrari, and J. N. Coleman, Nature Nanotechnology **3**, 563 (2008), arXiv:0805.2850 .

[85] M. Choucair, P. Thordarson, and J. A. Stride, Nature Nanotechnology **4**, 30 (2009).

[86] C. R. Dean, L. Wang, P. Maher, C. Forsythe, F. Ghahari, Y. Gao, J. Katoch, M. Ishigami, P. Moon, M. Koshino, T. Taniguchi, K. Watanabe, K. L. Shepard, J. Hone, and P. Kim, Nature **497**, 598 (2013).

[87] B. Hunt, T. Taniguchi, P. Moon, M. Koshino, and R. C. Ashoori, Science **340**, 1427 (2013), arXiv:1303.6942 .

[88] L. A. Ponomarenko, R. V. Gorbachev, G. L. Yu, D. C. Elias, R. Jalil, A. A. Patel, A. Mishchenko, A. S. Mayorov, C. R. Woods, J. R. Wallbank, M. Mucha-Kruczynski, B. A. Piot, M. Potemski, I. V. Grigorieva, K. S. Novoselov, F. Guinea, V. I. Fal'ko, and A. K. Geim, Nature **497**, 594 (2013), arXiv:1212.5012 .

[89] M. Yankowitz, J. Xue, D. Cormode, J. D. Sanchez-Yamagishi, K. Watanabe, T. Taniguchi, P. Jarillo-Herrero, P. Jacquod, and B. J. LeRoy, Nature Physics **8**, 382 (2012), arXiv:1202.2870 .

[90] S. Shallcross, S. Sharma, E. Kandelaki, and O. A. Pankratov, Physical Review B - Condensed Matter and Materials Physics **81**, 165105 (2010), arXiv:0910.5811 .

[91] E. Suárez Morell, J. D. Correa, P. Vargas, M. Pacheco, and Z. Barticevic, Physical Review B - Condensed Matter and Materials Physics **82** (2010), 10.1103/PhysRevB.82.121407, arXiv:1012.4320 .

[92] A. Grüneis, C. Attaccalite, L. Wirtz, H. S. R. Saito, T. Pichler, and A. Rubio, Physical Review B **78**, 205425 (2008), arXiv:0808.1467 .

[93] J. M. Campanera, G. Savini, I. Suarez-Martinez, and M. I. Heggie, Physical Review B **75**, 235449 (2007).

[94] A. Luican, G. Li, A. Reina, J. Kong, R. R. Nair, K. S. Novoselov, A. K. Geim, and E. Y. Andrei, Physical Review Letters **106**, 126802 (2011), arXiv:1010.4032 .

[95] R. Bistritzer and A. H. MacDonald, Proc. Natl. Acad. Sci. **108**, 12233 (2011).

[96] G. Trambly de LaissardieÌre, D. Mayou, and L. Magaud, Nano Letters **10**, 804 (2010).

[97] A. Weisse, The European Physical Journal B **40**, 125 (2004).

[98] L. Wang and A. Zunger, The Journal of Chemical Physics **100**, 2394 (1994).

[99] L.-W. Wang, Physical Review B **49**, 10154 (1994).

[100] H. Röder, R. N. Silver, D. A. Drabold, and J. J. Dong, Physical Review B **55**, 15382 (1997).

[101] Von N. W. Ashcroft und N. D. Mermin, Physik in unserer Zeit **9**, 33 (1978).

[102] R. Kubo, Canadian Journal of Physics **34**, 1274 (1956).

[103] R. Kubo, Journal of the Physical Society of Japan **12**, 570 (1957).

[104] D. A. Greenwood, Proceedings of the Physical Society **71**, 585 (1958).

[105] R. Landauer, IBM Journal of Research and Development **1**, 223 (1957).

[106] R. Landauer, Philosophical Magazine **21**, 863 (1970).

[107] M. BÌttiker, Y. Imry, R. Landauer, S. Pinhas, M. Büttiker, Y. Imry, R. Landauer, S. Pinhas, M. BÌttiker, Y. Imry, R. Landauer, and S. Pinhas, Physical Review B **31**, 6207 (1985).

[108] M. Büttiker, Y. Imry, R. Landauer, and S. Pinhas, Physical Review B **31**, 6207 (1985).

[109] A. Altland and B. Simons, *Condensed Matter Field Theory* (Cambridge University Press, Cambridge, 2006).

[110] H. Matsuda, Progress of Theoretical Physics Supplement **23**, 22 (1962).

[111] J. N. B. Rodrigues, N. M. R. Peres, and J. M. B. Lopes dos Santos, Physical Review B **86**, 214206 (2012).

[112] J. N. B. Rodrigues, N. M. R. Peres, and J. M. B. Lopes dos Santos, Journal of Physics: Condensed Matter **25**, 075303 (2013), arXiv:1210.8294 .

[113] U. Treske, F. Ortmann, B. Oetzel, K. Hannewald, and F. Bechstedt, Physica Status Solidi (A) Applications and Materials Science **207**, 304 (2010), arXiv:arXiv:0907.5243v1 .

[114] M. Kurzyna and T. Kwapiński, Journal of Applied Physics **123**, 194301 (2018).

[115] H.-S. Sim, H.-W. Lee, and K. J. Chang, Physical Review Letters **87**, 096803 (2001).

[116] R. H. M. Smit, C. Untiedt, G. Rubio-Bollinger, R. C. Segers, and J. M. van Ruitenbeek, Physical Review Letters **91**, 076805 (2003).

[117] A. K. Geim, Science **324**, 1530 (2009), arXiv:0906.3799 .

[118] F. Xia, H. Yan, and P. Avouris, Proceedings of the IEEE **101**, 1717 (2013).

[119] P. Avouris, Nano Letters **10**, 4285 (2010).

[120] H. Chen, M. B. Müller, K. J. Gilmore, G. G. Wallace, and D. Li, Advanced Materials **20**, 3557 (2008).

[121] G. Eda and M. Chhowalla, Nano Letters **9**, 814 (2009).

[122] T. Georgiou, R. Jalil, B. D. Belle, L. Britnell, R. V. Gorbachev, S. V. Morozov, Y.-J. Kim, A. Gholinia, S. J. Haigh, O. Makarovsky, L. Eaves, L. A. Ponomarenko, A. K. Geim, K. S. Novoselov, and A. Mishchenko, Nature Nanotechnology **8**, 100 (2013), arXiv:1211.5090 .

[123] H. Jang, Y. J. Park, X. Chen, T. Das, M. S. Kim, and J. H. Ahn, Advanced Materials **28**, 4184 (2016).

[124] J. P. Llinas, A. Fairbrother, G. Borin Barin, W. Shi, K. Lee, S. Wu, B. Yong Choi, R. Braganza, J. Lear, N. Kau, W. Choi, C. Chen, Z. Pedramrazi, T. Dumslaff, A. Narita, X. Feng, K. Müllen, F. Fischer, A. Zettl, P. Ruffieux, E. Yablonovitch, M. Crommie, R. Fasel, and J. Bokor, Nature Communications **8**, 8 (2017), arXiv:1605.06730 .

[125] R. Murali, Graphene Nanoelectronics: From Materials to Circuits **9781461405**, 51 (2012), arXiv:NIHMS150003 .

[126] Y.-W. Son, M. L. Cohen, and S. G. Louie, Physical Review Letters **97**, 216803 (2006), arXiv:0611602 [cond-mat] .

[127] M. Y. Han, B. Özyilmaz, Y. Zhang, and P. Kim, Physical Review Letters **98**, 206805 (2007), arXiv:0702511 [cond-mat] .

[128] Z. Chen, Y. M. Lin, M. J. Rooks, and P. Avouris, Physica E: Low-Dimensional Systems and Nanostructures **40**, 228 (2007), arXiv:0701599 [cond-mat] .

[129] S. Y. Zhou, G.-H. Gweon, A. V. Fedorov, P. N. First, W. A. de Heer, D.-H. Lee, F. Guinea, A. H. Castro Neto, and A. Lanzara, Nature Materials **6**, 770 (2007).

[130] E. V. Castro, N. M. R. Peres, J. M. B. L. Dos Santos, F. Guinea, and A. H. C. Neto, Journal of Physics: Conference Series **129** (2008), 10.1088/1742-6596/129/1/012002, arXiv:1004.5079 .

[131] E. McCann and M. Koshino, Rep. Prog. Phys. **76**, 56503 (2013).

[132] G. Li, A. Luican, J. M. B. Lopes dos Santos, A. H. Castro Neto, A. Reina, J. Kong, and E. Y. Andrei, Nature Physics **6**, 109 (2010), arXiv:0912.2102 .

[133] B. Amorim, Physical Review B **97**, 165414 (2018), arXiv:1711.02499 .

[134] Y. Cao, V. Fatemi, S. Fang, K. Watanabe, T. Taniguchi, E. Kaxiras, and P. Jarillo-Herrero, Nature **556**, 43 (2018).

[135] Y. Cao, V. Fatemi, A. Demir, S. Fang, S. L. Tomarken, J. Y. Luo, J. D. Sanchez-Yamagishi, K. Watanabe, T. Taniguchi, E. Kaxiras, R. C. Ashoori, and P. Jarillo-Herrero, Nature **556**, 80 (2018), arXiv:1802.00553 .

[136] C. R. Woods, T. M. Fromhold, A. K. Geim, A. Mishchenko, K. Watanabe, J. S. Tu, Y.-J. Kim, J. R. Wallbank, R. V. Gorbachev, T. Taniguchi, F. Withers, V. I. Fal'ko, E. E. Vdovin, Y. Cao, K. S. Novoselov, M. T. Greenaway, V. E. Morozov, L. Eaves, S. L. Wong, S. V. Morozov, O. Makarovsky, and M. J. Zhu, Nature Nanotechnology **9**, 808 (2014).

[137] A. Mishchenko, M. I. Katsnelson, L. A. Ponomarenko, J. Leist, T. Georgiou, B. D. Belle, L. Britnell, A. K. Geim, S. V. Morozov, K. S. Novoselov, F. Schedin, L. Eaves, R. Jalil, N. M. R. Peres, and R. V. Gorbachev, Science **335**, 947 (2012).

[138] L. Britnell, R. V. Gorbachev, R. Jalil, B. D. Belle, F. Schedin, M. I. Katsnelson, L. Eaves, S. V. Morozov, A. S. Mayorov, N. M. R. Peres, A. H. Castro Neto, J. Leist, A. K. Geim, L. A. Ponomarenko, and K. S. Novoselov, Nano Letters **12**, 1707 (2012).

[139] B. Amorim, R. M. Ribeiro, and N. M. R. Peres, Physical Review B **93**, 235403 (2016), arXiv:1603.04446 .

[140] F. Chen, H. Ilatikhameneh, Y. Tan, G. Klimeck, and R. Rahman, IEEE Transactions on Electron Devices **65**, 3065 (2018), arXiv:1711.01832 .

[141] I. Martin, Y. M. Blanter, and A. F. Morpurgo, Physical Review Letters **100**, 36804 (2008), arXiv:0709.3522 .

[142] M. Koshino, Physical Review B - Condensed Matter and Materials Physics **88**, 115409 (2013), arXiv:1307.3421 .

[143] M. Barbier, P. Vasilopoulos, F. M. Peeters, and J. M. Pereira, Physical Review B - Condensed Matter and Materials Physics **79**, 155402 (2009), arXiv:1101.3930 .

[144] M. E. Wilkinson, S. M. Fica, W. P. Galej, X.-C. Bai, A. J. Newman, K. Nagai, and C. Oubridge, Nature **542**, 377 (2017).

[145] C. P. Puls, N. E. Staley, and Y. Liu, Physical Review B **79**, 235415 (2009).

[146] X. Xu, N. M. Gabor, J. S. Alden, A. M. van der Zande, and P. L. McEuen, Nano letters **10**, 562 (2010), arXiv:0907.3173 .

[147] S. Datta, *Quantum Transport: Atom to Transistor*, Vol. 9780521631 (Cambridge University Press, Cambridge, 2005) pp. 1–404, arXiv:arXiv:1011.1669v3 .

[148] J. Kang and O. Vafek, Physical Review X **8**, 031088 (2018).

[149] L. Zou, H. C. Po, A. Vishwanath, and T. Senthil, Physical Review B **98**, 085435 (2018).

[150] L. Rademaker and P. Mellado, Physical Review B **98**, 235158 (2018).

[151] C. C. Liu, L. D. Zhang, W. Q. Chen, and F. Yang, Physical Review Letters **121**, 217001 (2018).

[152] J. W. F. Venderbos and R. M. Fernandes, Physical Review B **98**, 245103 (2018), arXiv:1808.10416 .

[153] Y. Sherkunov and J. J. Betouras, Physical Review B **98**, 205151 (2018).

[154] F. Guinea and N. R. Walet, Proceedings of the National Academy of Sciences **115**, 13174 (2018).

[155] H. C. Po, L. Zou, T. Senthil, and A. Vishwanath, Phys. Rev. B **99**, 195455 (2018), arXiv:1808.02482 .

[156] N. F. Q. Yuan, M. Koshino, L. Fu, T. Koretsune, M. Ochi, K. Kuroki, N. F. Q. Yuan, T. Koretsune, M. Ochi, K. Kuroki, and L. Fu, Physical Review X **8**, 031087 (2018).

[157] T. J. Peltonen, R. Ojajärvi, and T. T. Heikkilä, Physical Review B **98**, 220504 (2018).

[158] N. F. Q. Yuan and L. Fu, Physical Review B **98**, 045103 (2018).

[159] H. C. Po, L. Zou, A. Vishwanath, and T. Senthil, Physical Review X **8**, 031089 (2018).

[160] J. F. Dodaro, S. A. Kivelson, Y. Schattner, X. Q. Sun, and C. Wang, Physical Review B **98** (2018), 10.1103/PhysRevB.98.075154.

[161] M. Ochi, M. Koshino, and K. Kuroki, Physical Review B **98**, 081102 (2018).

[162] S. Carr, S. Fang, P. Jarillo-Herrero, and E. Kaxiras, Physical Review B **98**, 085144 (2018).

[163] D. M. Kennes, J. Lischner, and C. Karrasch, Phys. Rev. B **98**, 241407 (2018).

[164] Y. W. Choi and H. J. Choi, Physical Review B **98**, 241412 (2018).

[165] F. Wu, A. MacDonald, and I. Martin, Physical Review Letters **121**, 257001 (2018).

[166] C. Xu and L. Balents, Physical Review Letters **121**, 087001 (2018).

[167] A. Thomson, S. Chatterjee, S. Sachdev, and M. S. Scheurer, Physical Review B **98**, 075109 (2018).

[168] H. Isobe, N. F. Q. Yuan, and L. Fu, Physical Review X **8**, 041041 (2018).

[169] J. Liu, J. Liu, and X. Dai, Physical Review B **99**, 155415 (2019), arXiv:1810.03103 .

[170] M. Fidrysiak, M. Zegrodnik, and J. Spałek, Physical Review B **98**, 085436 (2018).

[171] X. Lin, D. Liu, and D. Tománek, Physical Review B **98**, 195432 (2018).

[172] Z. Song, Z. Wang, W. Shi, G. Li, C. Fang, and B. A. Bernevig, Phys. Rev. Lett. **123**, 36401 (2019), arXiv:1807.10676 .

[173] C. Mora, N. Regnault, and B. A. Bernevig, Phys. Rev. Lett. **123**, 26402 (2019), arXiv:1901.05469 .

[174] B. L. Chittari, G. Chen, Y. Zhang, F. Wang, and J. Jung, Phys. Rev. Lett. **122**, 16401 (2019).

[175] F. Wu and S. Das Sarma, Phys. Rev. B **99**, 220507(R) (2019), arXiv:1904.07875 .

[176] J. González and T. Stauber, Physical Review Letters **122**, 026801 (2019).

[177] A. O. Sboychakov, A. V. Rozhkov, A. L. Rakhmanov, and F. Nori, Phys. Rev. B **100**, 45111 (2019), arXiv:1807.08190 .

[178] Y.-H. Zhang, D. Mao, Y. Cao, P. Jarillo-Herrero, and T. Senthil, Physical Review B **99**, 075127 (2019).

[179] G. Tarnopolsky, A. J. Kruchkov, and A. Vishwanath, Physical Review Letters **122**, 106405 (2019).

[180] F. Wu, Phys. Rev. B **99**, 195114 (2019).

[181] B. Lian, Z. Wang, and B. A. Bernevig, Physical Review Letters **122**, 257002 (2019).

[182] S. Ray, J. Jung, and T. Das, Physical Review B **99** (2019), 10.1103/PhysRevB.99.134515.

[183] K. Hejazi, C. Liu, H. Shapourian, X. Chen, and L. Balents, Physical Review B **99**, 035111 (2019).

[184] J. M. Pizarro, M. J. Calderón, and E. Bascones, J. Phys. Commun. **3**, 35024 (2019), arXiv:1805.07303 .

[185] N. Bultinck, S. Chatterjee, and M. P. Zaletel, (2019), arXiv:1901.08110 .

[186] S. Carr, S. Fang, H. C. Po, A. Vishwanath, and E. Kaxiras, (2019), arXiv:1907.06282 .

[187] S. Carr, S. Fang, Z. Zhu, and E. Kaxiras, (2019), arXiv:1901.03420 .

[188] T. Cea, N. R. Waler, and F. Guinea, (2019), arXiv:1906.10570 .

[189] F. Haddadi, Q. Wu, A. J. Kruchkov, and O. V. Yazyev, (2019), arXiv:1906.00623 .

[190] L. Rademaker, D. A. Abanin, and P. Mellado, (2019), arXiv:1907.00940 .

[191] Y.-H. Zhang, D. Mao, and T. Senthil, (2019), arXiv:1901.08209 .

[192] L. Klebl and C. Honerkamp, Phys. Rev. B **100**, 155145 (2019), arXiv:1907.10006 .

[193] M. Xie and A. H. MacDonald, (2018), arXiv:1812.04213 .

[194] S. Liu, E. Khalaf, J. Y. Lee, and A. Vishwanath, (2019), arXiv:1905.07409 .

[195] N. Bultinck, E. Khalaf, S. Liu, S. Chatterjee, A. Vishwanath, and M. P. Zaletel, (2019), arXiv:1911.02045 .

[196] S. Liu, E. Khalaf, J. Y. Lee, and A. Vishwanath, (2019), arXiv:1905.07409 .

[197] T. Cea and F. Guinea, (2020), arXiv:2004.01577 .

[198] T.-F. Chung, Y. Xu, and Y. P. Chen, Physical Review B **98**, 035425 (2018).

[199] M. Yankowitz, S. Chen, H. Polshyn, Y. Zhang, K. Watanabe, T. Taniguchi, D. Graf, A. F. Young, and C. R. Dean, Science (New York, N.Y.) **363**, 1059 (2019).

[200] A. L. Sharpe, E. J. Fox, A. W. Barnard, J. Finney, K. Watanabe, T. Taniguchi, M. A. Kastner, and D. Goldhaber-Gordon, (2019), arXiv:1901.03520 .

[201] A. Kerelsky, L. J. McGilly, D. M. Kennes, L. Xian, M. Yankowitz, S. Chen, K. Watanabe, T. Taniguchi, J. Hone, C. Dean, A. Rubio, and A. N. Pasupathy, Nature **572**, 95 (2019), arXiv:1812.08776 .

[202] Y. Choi, J. Kemmer, Y. Peng, A. Thomson, H. Arora, R. Polski, Y. Zhang, H. Ren, J. Alicea, G. Refael, F. von Oppen, K. Watanabe, T. Taniguchi, and S. Nadj-Perge, (2019), arXiv:1901.02997 .

[203] Y. Jiang, X. Lai, K. Watanabe, T. Taniguchi, K. Haule, J. Mao, and E. Y. Andrei, Nature (2019), 10.1038/s41586-019-1460-4, arXiv:1904.10153 .

[204] Y. Xie, B. Lian, B. Jäck, X. Liu, C.-L. Chiu, K. Watanabe, T. Taniguchi, B. A. Bernevig, and A. Yazdani, (2019), arXiv:1906.09274 .

[205] S. L. Tomarken, Y. Cao, A. Demir, K. Watanabe, T. Taniguchi, P. Jarillo-Herrero, and R. C. Ashoori, Phys. Rev. Lett. **123**, 46601 (2019), arXiv:1903.10492 .

[206] X. Lu, P. Stepanov, W. Yang, M. Xie, M. A. Aamir, I. Das, C. Urgell, K. Watanabe, T. Taniguchi, G. Zhang, A. Bachtold, A. H. MacDonald, and D. K. Efetov, Nature **574**, 653 (2019), arXiv:1903.06513 .

[207] E. Codecido, Q. Wang, R. Koester, S. Che, H. Tian, R. Lv, S. Tran, K. Watanabe, T. Taniguchi, F. Zhang, M. Bockrath, and C. N. Lau, Sci. Adv. **5** (2019), 10.1126/sciadv.aaw9770, arXiv:1902.05151 .

[208] H. Shi, Z. Zhan, Z. Qi, K. Huang, E. van Veen, J. A. Silva-Guillén, R. Zhang, P. Li, K. Xie, H. Ji, M. I. Katsnelson, S. Yuan, S. Qin, and Z. Zhang, (2019), arXiv:1905.04515 .

[209] M. Serlin, C. L. Tschirhart, H. Polshyn, Y. Zhang, J. Zhu, K. Watanabe, T. Taniguchi, L. Balents, and A. F. Young, (2019), arXiv:1907.00261 .

[210] C. Shen, N. Li, S. Wang, Y. Zhao, J. Tang, J. Liu, J. Tian, Y. Chu, K. Watanabe, T. Taniguchi, R. Yang, Z. Y. Meng, D. Shi, and G. Zhang, (2019), arXiv:1903.06952 .

[211] X. Liu, Z. Hao, E. Khalaf, J. Y. Lee, K. Watanabe, T. Taniguchi, A. Vishwanath, and P. Kim, (2019), arXiv:1903.08130 .

[212] Y. Cao, D. Rodan-Legrain, O. Rubies-Bigorda, J. M. Park, K. Watanabe, T. Taniguchi, and P. Jarillo-Herrero, (2019), arXiv:1903.08596 .

[213] G. Chen, A. L. Sharpe, P. Gallagher, I. T. Rosen, E. J. Fox, L. Jiang, B. Lyu, H. Li, K. Watanabe, T. Taniguchi, J. Jung, Z. Shi, D. Goldhaber-Gordon, Y. Zhang, and F. Wang, Nature **572**, 215 (2019).

[214] W.-J. Zuo, J.-B. Qiao, D.-L. Ma, L.-J. Yin, G. Sun, J.-Y. Zhang, L.-Y. Guan, and L. He, Phys. Rev. B **97**, 35440 (2018), arXiv:1711.08109 .

[215] F. Wu, T. Lovorn, E. Tutuc, I. Martin, and A. H. MacDonald, Physical Review Letters **122**, 086402 (2019).

[216] L. Wang, E.-M. Shih, A. Ghiotto, L. Xian, D. A. Rhodes, C. Tan, M. Claassen, D. M. Kennes, Y. Bai, B. Kim, K. Watanabe, T. Taniguchi, X. Zhu, J. Hone, A. Rubio, A. Pasupathy, and C. R. Dean, (2019), arXiv:1910.12147 .

[217] N. F. Q. Yuan, M. Koshino, L. Fu, T. Koretsune, M. Ochi, and K. Kuroki, Phys. Rev. X **8**, 031087 (2018).

[218] S. Shallcross, S. Sharma, and O. Pankratov, Phys. Rev. B - Condens. Matter Mater. Phys. **87**, 245403 (2013).

[219] Y. Cao, J. Y. Luo, V. Fatemi, S. Fang, J. D. Sanchez-Yamagishi, K. Watanabe, T. Taniguchi, E. Kaxiras, and P. Jarillo-Herrero, Phys. Rev. Lett. **117**, 116804 (2016).

[220] H. Polshyn, M. Yankowitz, S. Chen, Y. Zhang, K. Watanabe, T. Taniguchi, C. R. Dean, and A. F. Young, (2019), arXiv:1902.00763 .

[221] H. Yoo, R. Engelke, S. Carr, S. Fang, K. Zhang, P. Cazeaux, S. H. Sung, R. Hovden, A. W. Tsen, T. Taniguchi, K. Watanabe, G.-C. Yi, M. Kim, M. Luskin, E. B. Tadmor, E. Kaxiras, and P. Kim, Nat. Mater. **18**, 448 (2019), arXiv:1804.03806 .

[222] X. Liu, Z. Wang, K. Watanabe, T. Taniguchi, O. Vafek, and J. I. A. Li, (2020), arXiv:2003.11072 .

[223] M. Andelković, L. Covaci, and F. M. Peeters, Phys. Rev. Mater. **2**, 34004 (2018), arXiv:1705.05731 .

[224] E. H. Hwang and S. D. Sarma, (2019), arXiv:1907.02856 .

[225] F. Wu, E. Hwang, and S. Das Sarma, Phys. Rev. B **99**, 165112 (2019).

[226] M. Pelc, E. S. Morell, L. Brey, and L. Chico, Journal of Physical Chemistry C **119**, 10076 (2015), arXiv:arXiv:1407.6594v2 .

[227] D. A. Bahamon, G. Gómez-Santos, and T. Stauber, (2019), arXiv:1909.09341 .

[228] B. Padhi, A. Tiwari, T. Neupert, and S. Ryu, (2020), arXiv:2005.02406 .

[229] J. C. Slater and G. F. Koster, Physical Review **94**, 1498 (1954), arXiv:1506.08190 .

[230] G. Trambly De Laissardière, D. Mayou, and L. Magaud, Phys. Rev. B - Condens. Matter Mater. Phys. **86**, 125413 (2012).

[231] H. Z. Olyaei, P. Ribeiro, and E. V. Castro, Phys. Rev. B **99**, 205436 (2019), arXiv:1810.11743 .

[232] E. Suárez Morell, P. Vargas, L. Chico, and L. Brey, Physical Review B - Condensed Matter and Materials Physics **84** (2011), 10.1103/PhysRevB.84.195421, arXiv:1112.5467 .

[233] M. N. van der Linden, J. P. K. Doye, and A. A. Louis, J. Chem. Phys. **136**, 54904 (2012).

[234] P. Moon, M. Koshino, and Y. W. Son, Phys. Rev. B **99**, 165430 (2019).

[235] R. Bistritzer and A. H. MacDonald, Phys. Rev. B **81**, 245412 (2010), arXiv:1002.2983 .

[236] B. Amorim and E. V. Castro, (2018), arXiv:1807.11909 .